

DESIGN OF A CUSTOMIZED, SEMI-AUTONOMOUS,
SINGLE ARM ROBOTIC MANIPULATOR FOR A HAZARDOUS ENVIRONMENT

A Thesis
presented to
the Faculty of the Graduate School
at the University of Missouri-Columbia

In Partial Fulfillment
of the Requirements for the Degree
Master of Science

by
ANDREW GUNN
Dr. A. Sherif El-Gizawy, Thesis Supervisor

DECEMBER 2016

© Copyright by Andrew Gunn 2016

All Rights Reserved

The undersigned, appointed by the dean of the Graduate School, have examined the thesis entitled

DESIGN OF A CUSTOMIZED, SEMI-AUTONOMOUS,
SINGLE ARM ROBOTIC MANIPULATOR FOR A HAZARDOUS ENVIRONMENT

presented by Andrew Gunn,

a candidate for the degree of Master of Science,

and hereby certify that, in their opinion, it is worthy of acceptance:

Professor A. Sherif El-Gizawy

Professor Hani Salim

Professor Abdel Elsayy

ACKNOWLEDGEMENTS

I would like to thank my research advisor, Dr. Sherif El-Gizawy for providing me the opportunity and the funding to work on such a unique and challenging project that spans so many different facets of science, engineering and mathematics. I have gained so much invaluable knowledge about how to approach and solve real-world engineering problems and the engineering design process in general over the course of this research. I am thankful for his guidance and motivation throughout the entire process.

I would also like to thank my fellow graduate students, Bilal Hussain, Zhentao Xie, and Tony Adamson for their support and assistance whether it was through brainstorming ideas, helping me become familiar with different software, helping me to configure and use hardware, or helping me to understand abstract physical and mathematical principles. My research would have probably floundered in the beginning stages if not for their help and support.

I would like to give huge thanks to Ghassan Al Bahhash and Rex Gish in the ETS machine shop for their terrific jobs in interpreting my drawings and machining parts for my designs. If not for their skill and ability to recognize the logic in my sometimes disjointed ideas, the final product would have never achieved the quality that it did.

I would certainly like to thank my family, my mom and dad, Marla and Greg, and my brother Joe for their support, both emotionally and financially throughout this process. Getting this far would have been profoundly more difficult for me had they not been behind me as a safety net. Finally I would like to thank Megan Barrows, her continued patience and support inspired confidence in me during some of the most tedious hours of this project and I am very grateful for her companionship.

TABLE OF CONTENTS

ACKNOWLEDGEMENTS.....	ii
LIST OF FIGURES.....	v
LIST OF TABLES.....	ix
ABSTRACT.....	x
CHAPTER 1: INTRODUCTION.....	1
1-1: Introduction and Background.....	1
1-2: Objectives and Motivation.....	3
CHAPTER 2: LITERATURE REVIEW.....	6
2-1: Existing Research.....	6
2-2: Challenges Facing Robots in Hazardous Environments.....	9
2-3: Accuracy and Reliability in Hazardous Environment Robot Design.....	13
2-4: Building upon Existing Research.....	16
CHAPTER 3: PREVIOUS DESIGN ITERATIONS.....	17
3-1: Previous Design Iterations.....	17
3-2: Strengths and Weaknesses of Previous Designs.....	20
3-3: Building upon Previous Designs.....	22
CHAPTER 4: CONCEPTUAL DESIGN.....	24
4-1: Design Assumptions and Simplification.....	24
4-2: Constraints and Objectives.....	29
4-3: Satisfying Constraints and Objectives.....	34
4-3-1 Shoulder and Elbow Design.....	40
4-3-2 Bicep Design.....	43

4-3-3 Forearm and Wrist Design	45
4-3-4 End Effector Design	49
4-4: Final Mechanical Design	51
CHAPTER 5: MODELLING AND ANALYSIS OF CONCEPTUAL DESIGN	54
5-1: Manipulator Kinematics and Inverse Kinematics	54
5-2: Manipulator Dynamic Model	67
5-2-1: First Iteration Dynamic Model	68
5-2-2: Simulation and Structural Evaluation	74
5-3: Prototype Construction and Model Validation	83
5-4: Actuator Dynamic Model and Validation	95
CHAPTER 6: CONTROL AND ACCURACY/RELIABILITY STUDY	105
6-1: Control Design	105
6-2: Accuracy and Reliability Study	120
6-3: Control Implementation and Preliminary Testing	132
CHAPTER 7: CONCLUSIONS AND FUTURE WORK	138
BIBLIOGRAPHY	141
APPENDICES	144
A: Manipulator Kinematics	144
B: Manipulator Dynamics	146
C: Hall Array Calibration	153
D: Accelerometer Calibration	158
E: Model Validation Results	164
F: Accuracy and Control Performance Plots and Uncertainty Calculations	176

LIST OF FIGURES

Figure 1: Hot Cell Radiation Containment Vessel.....	2
Figure 2: Hot Cell Manipulators.....	2
Figure 3: Conceptual Hot Cell Environment with a Single Arm Robot.....	4
Figure 4: AARM Maintenance Robot.....	6
Figure 5: Tele-Operated Force-Feedback Manipulator.....	8
Figure 6a: Two Link Planar Robot.....	15
Figure 6b: Three Link Planar Robot.....	15
Figure 7: First Iteration Single-Arm Robotic Manipulator.....	18
Figure 8: Second Iteration, Dual-Arm Manipulator.....	19
Figure 9a: Third Iteration Single-Arm Manipulator.....	19
Figure 9b: Fourth Iteration Wall-Mounted Manipulator.....	19
Figure 10: Robotic System Behavior Diagram.....	24
Figure 11: Single-Arm-Robot Basic Task.....	26
Figure 12a: Two DOF Base with Prismatic and Revolute Joint.....	27
Figure 12b: Two DOF Base with Two Prismatic Joints.....	27
Figure 12c: Three DOF Base with Treads.....	27
Figure 13: Single-Arm Robot Task Description.....	28
Figure 14: Various 4 DOF Manipulator Design Concepts.....	30
Figure 15: Approximate Work Envelopes of 4 DOF Manipulators.....	31
Figure 16: Wrist Work Envelopes of Manipulators C and D.....	33
Figure 17: Single-Arm Robot Sub-Systems.....	35
Figure 18: Shoulder and Elbow Assembly Exploded View.....	40
Figure 19: Shoulder and Elbow Assembly Cross Section.....	41
Figure 20: Bicep Link Assembly Exploded View.....	43
Figure 21: Forearm and Wrist Roll Assembly Exploded View.....	46
Figure 22: Forearm and Wrist Roll Assembly Cross Section.....	46
Figure 23: Wrist Pitch Assembly Exploded View.....	48
Figure 24: End Effector Assembly Exploded View.....	50
Figure 25: End Effector Assembled.....	50
Figure 26: Fully Assembled, Single-Arm Robot Mechanical Design.....	52
Figure 27: Mechanical Design with Kinematic Design Superimposed.....	53
Figure 28: Definition of Kinematic Parameters.....	55
Figure 29: Exponential Coordinate Description.....	57
Figure 30: Description of Twist Coordinates.....	59
Figure 31: Four DOF Manipulator in Reference Configuration.....	62
Figure 32: 4 DOF Manipulator Work Envelope Side View.....	65
Figure 33: 4 DOF Manipulator Work Envelope Isometric View.....	65
Figure 34: Concept of Inverse Kinematics.....	66
Figure 35: Schematic Diagram of Four DOF Manipulator with Link C.O.M.....	68
Figure 36: Bicep (Link 1) Dynamic Parameters from SOLIDWORKS™.....	74
Figure 37: Initial Torque Evaluation State Transition.....	76
Figure 38: First Iteration Shoulder Torque Evaluation.....	76
Figure 39: Torque vs. Travel Time Test 1.....	77

Figure 40: Torque vs. Travel Time Test 2.....	77
Figure 41: Torque vs. Travel Time Test 3.....	78
Figure 42: Manipulator in Static Horizontal Configuration.....	79
Figure 43: Shoulder Torque from Horizontal to Reference Configuration.....	79
Figure 44: Shoulder Axle FEA Loading.....	81
Figure 45: Shoulder Axle FEA Supports and Fixtures.....	82
Figure 46: FEA Simulation Results.....	82
Figure 47: Robot Arm Prototype.....	83
Figure 48: Position Sensor Location and Calibration.....	84
Figure 49: Model Validation Test Configuration 1.....	86
Figure 50: End Effector Acceleration Measurement.....	87
Figure 51: Other Model Validation Test Configurations.....	89
Figure 52: First Model Validation Response Comparison.....	89
Figure 53: Model Validation Response with Added Viscous Friction.....	90
Figure 54: Model of Friction with Coulomb and Viscous Components.....	91
Figure 55: Critiqued Model of Coulomb and Viscous Friction.....	92
Figure 56: Expanded View of New Friction Model.....	93
Figure 57: Model Validation Response Comparison with New Friction Model.....	94
Figure 58: Electro-Mechanical Representation of the Robot Arm.....	96
Figure 59: DC Motor Schematic Representation.....	97
Figure 60: Characteristic Diagram of Shoulder Motor from Spec Sheet.....	100
Figure 61: Characteristic Diagram of Elbow Motor from Spec Sheet.....	100
Figure 62: Simulated Characteristic Diagram of Shoulder Motor.....	101
Figure 63: Simulated Characteristic Diagram of Elbow Motor.....	101
Figure 64: Simulated Diagram of Wrist Roll and Wrist Pitch Motors.....	102
Figure 65: Block Diagram Representation of Robotic Control System.....	105
Figure 66: Angular Pos. and Vel. Trajectories for Computed Torque Control.....	110
Figure 67: Angular Acc. and Torque Trajectories for Computed Torque Control.....	111
Figure 68: Computed Torque Controller with Feedback.....	112
Figure 69: Computed Torque Control Simulation Block Diagram.....	114
Figure 70: Computed Torque Control Joint Position Tracking Results: 10 Iterations.....	115
Figure 71: Computed Torque Control Input Results: 10 Iterations.....	116
Figure 72: Robot Arm and Motor Control Diagram with Computed Torque Controller and Current Regulator.....	118
Figure 73: Block Diagram of Motor Control Simulation with Current Regulator.....	119
Figure 74a: Joint Trajectory Tracking for $\vec{\theta}_0 = [0^\circ, 0^\circ, 0^\circ, 0^\circ]$, $\vec{\theta}_f = [-70^\circ, -50^\circ, 70^\circ, 30^\circ]$	120
Figure 74b: Joint Trajectory Tracking for $\vec{\theta}_0 = [-70^\circ, -50^\circ, 70^\circ, 30^\circ]$, $\vec{\theta}_f =$ $[0^\circ, 0^\circ, 0^\circ, 0^\circ]$	120
Figure 75: Monte Carlo Accuracy Analysis $\vec{\theta}_0 = [0^\circ, 0^\circ, 0^\circ, 0^\circ]$ to $\vec{\theta}_f = [-70^\circ, -50^\circ, 70^\circ, 30^\circ]$ Dynamic Uncertainty Only.....	125
Figure 76: Monte Carlo Accuracy Analysis $\vec{\theta}_0 = [0^\circ, 0^\circ, 0^\circ, 0^\circ]$ to $\vec{\theta}_f = [-70^\circ, -50^\circ, 70^\circ, 30^\circ]$ Dynamic and Kinematic Uncertainty.....	126
Figure 77: Monte Carlo Accuracy Analysis $\vec{\theta}_0 = [-70^\circ, -50^\circ, 70^\circ, 30^\circ]$ to $\vec{\theta}_f =$ $[0^\circ, 0^\circ, 0^\circ, 0^\circ]$ Dynamic and Kinematic Uncertainty.....	127

Figure 78: Manipulator in Home Configuration.....	128
Figure 79: Accuracy Analysis for $\vec{\theta}_0 = [-70^\circ, -50^\circ, 70^\circ, 30^\circ]$ to Home Config.....	128
Figure 80: Probabilistic End Effector Position Relative to a Target Location.....	129
Figure 81: Monte Carlo Analysis: Maximum Voltage.....	130
Figure 82: Monte Carlo Analysis: Maximum Torque.....	131
Figure 83: Monte Carlo Analysis: Maximum Current.....	131
Figure 84: Robot Arm Real-Time Control Schematic Diagram.....	133
Figure 85: Robot Arm Real-Time Control Configuration.....	134
Figure 86: Robot Arm Finite-State-Machine Representation.....	137
Figure 87: Shoulder Principal Axes of Inertia and C.O.M.....	150
Figure 88: Elbow Principal Axes of Inertia and C.O.M.....	150
Figure 89: Wrist Principal Axes of Inertia and C.O.M.....	150
Figure 90: End Effector Principal Axes of Inertia and C.O.M.....	151
Figure 91: First Iteration Elbow Torque Evaluation.....	151
Figure 92: First Iteration Wrist Roll Torque Evaluation.....	151
Figure 93: First Iteration Wrist Pitch Torque Evaluation.....	152
Figure 94: Hall Array Calibration Setup.....	153
Figure 95: Shoulder Hall Sensor Array Configuration.....	153
Figure 96: Elbow Hall Sensor Array Configuration.....	153
Figure 97: Data Acquisition and Motor Control for Calibration.....	154
Figure 98: Hall Array Measurements as Function of Angular Position.....	155
Figure 99: Sparse Set of Hall Array Measurement vs. Angular Position.....	156
Figure 100: Graphical Angular Position vs. Hall Voltage Lookup Table.....	156
Figure 101: Sample of Angular Position from both Encoder and Hall Array.....	157
Figure 102: Accelerometer Reference Zero Calibration.....	158
Figure 103: Accelerometer Measurement during Rotation about Arbitrary Axis.....	159
Figure 104a: Accelerometer Measuring 1g along Positive Y-Axis.....	160
Figure 104b: Accelerometer Measuring 1g along Positive X-Axis.....	160
Figure 105: Accelerometer Measuring 1g along Negative Z-Axis.....	160
Figure 106: X-axis Reading with Y and Z held at Zero and Gravity in $-X$ Direction.....	161
Figure 107: Y-axis Reading with X and Z held at Zero and Gravity in $-Y$ Direction.....	161
Figure 108: Z-axis Reading with X and Y held at Zero and Gravity in $-Z$ Direction.....	161
Figure 109: X-axis Reading with Y and Z held at Zero and Gravity in $+X$ Direction.....	162
Figure 110: Y-axis Reading with X and Z held at Zero and Gravity in $+Y$ Direction.....	162
Figure 111: Z-axis Reading with X and Y held at Zero and Gravity in $+Z$ Direction.....	162
Figure 112: Initial Condition Test 1 Shoulder Trials.....	164
Figure 113: Initial Condition Test 1 Elbow Trials.....	164
Figure 114: Initial Condition Test 1 Tool Acceleration Trials.....	165
Figure 115: Initial Condition Test 2 Shoulder Trials.....	165
Figure 116: Initial Condition Test 2 Elbow Trials.....	166
Figure 117: Initial Condition Test 2 Tool Acceleration Trials.....	166
Figure 118: Initial Condition Test 3 Shoulder Trials.....	167
Figure 119: Initial Condition Test 3 Elbow Trials.....	167
Figure 120: Initial Condition Test 3 Tool Acceleration Trials.....	168
Figure 121: Initial Condition Test 4 Shoulder Trials.....	168
Figure 122: Initial Condition Test 4 Elbow Trials.....	169

Figure 123: Initial Condition Test 4 Tool Acceleration Trials.....	169
Figure 124: Initial Condition Test 5 Shoulder Trials.....	170
Figure 125: Initial Condition Test 5 Elbow Trials.....	170
Figure 126: Initial Condition Test 5 Tool Acceleration Trials.....	171
Figure 127: Initial Condition Test 6 Shoulder Trials.....	171
Figure 128: Initial Condition Test 6 Elbow Trials.....	172
Figure 129: Initial Condition Test 6 Tool Acceleration Trials.....	172
Figure 130: Initial Condition Test 2 Response Comparisons.....	173
Figure 131: Initial Condition Test 3 Response Comparisons.....	173
Figure 132: Initial Condition Test 4 Response Comparisons.....	173
Figure 133: Initial Condition Test 5 Response Comparisons.....	174
Figure 134: Initial Condition Test 6 Response Comparisons.....	174
Figure 135: Gearbox Manufacturer Specifications.....	174
Figure 136: Elbow Motor Manufacturer Specifications.....	175
Figure 137: Shoulder Motor Manufacturer Specifications.....	175
Figure 138a: Motor Voltage for $\vec{\theta}_0 = [0^\circ, 0^\circ, 0^\circ, 0^\circ]$, $\vec{\theta}_f = [-70^\circ, -50^\circ, 70^\circ, 30^\circ]$	176
Figure 138b: Motor Voltage for $\vec{\theta}_0 = [-70^\circ, -50^\circ, 70^\circ, 30^\circ]$, $\vec{\theta}_f = [0^\circ, 0^\circ, 0^\circ, 0^\circ]$	176
Figure 139a: Motor Torque for $\vec{\theta}_0 = [0^\circ, 0^\circ, 0^\circ, 0^\circ]$, $\vec{\theta}_f = [-70^\circ, -50^\circ, 70^\circ, 30^\circ]$	176
Figure 139b: Motor Torque for $\vec{\theta}_0 = [-70^\circ, -50^\circ, 70^\circ, 30^\circ]$, $\vec{\theta}_f = [0^\circ, 0^\circ, 0^\circ, 0^\circ]$	176
Figure 140a: Motor Current for $\vec{\theta}_0 = [0^\circ, 0^\circ, 0^\circ, 0^\circ]$, $\vec{\theta}_f = [-70^\circ, -50^\circ, 70^\circ, 30^\circ]$	177
Figure 140b: Current Error for $\vec{\theta}_0 = [0^\circ, 0^\circ, 0^\circ, 0^\circ]$, $\vec{\theta}_f = [-70^\circ, -50^\circ, 70^\circ, 30^\circ]$	177
Figure 140c: Motor Current for $\vec{\theta}_0 = [-70^\circ, -50^\circ, 70^\circ, 30^\circ]$, $\vec{\theta}_f = [0^\circ, 0^\circ, 0^\circ, 0^\circ]$	177
Figure 140d: Current Error for $\vec{\theta}_0 = [-70^\circ, -50^\circ, 70^\circ, 30^\circ]$, $\vec{\theta}_f = [0^\circ, 0^\circ, 0^\circ, 0^\circ]$	177
Figure 141: Grasped Object Mass and Location Uncertainty.....	181
Figure 142a: Max Motor Voltage for $\vec{\theta}_0 = [0^\circ, 0^\circ, 0^\circ, 0^\circ]$, $\vec{\theta}_f = [-70^\circ, -50^\circ, 70^\circ, 30^\circ]$, 1000 Iterations, Dynamic Uncertainty Only.....	185
Figure 142b: Max Motor Current for $\vec{\theta}_0 = [0^\circ, 0^\circ, 0^\circ, 0^\circ]$, $\vec{\theta}_f = [-70^\circ, -50^\circ, 70^\circ, 30^\circ]$, 1000 Iterations, Dynamic Uncertainty Only.....	185
Figure 142c: Max Motor Torque for $\vec{\theta}_0 = [0^\circ, 0^\circ, 0^\circ, 0^\circ]$, $\vec{\theta}_f = [-70^\circ, -50^\circ, 70^\circ, 30^\circ]$, 1000 Iterations, Dynamic Uncertainty Only.....	185
Figure 143a: Max Motor Voltage for $\vec{\theta}_0 = [-70^\circ, -50^\circ, 70^\circ, 30^\circ]$, $\vec{\theta}_f = [0^\circ, 0^\circ, 0^\circ, 0^\circ]$, 1000 Iterations, Dynamic and Kinematic Uncertainty.....	186
Figure 143b: Max Motor Current for $\vec{\theta}_0 = [-70^\circ, -50^\circ, 70^\circ, 30^\circ]$, $\vec{\theta}_f = [0^\circ, 0^\circ, 0^\circ, 0^\circ]$, 1000 Iterations, Dynamic and Kinematic Uncertainty.....	186
Figure 143c: Max Motor Torque for $\vec{\theta}_0 = [-70^\circ, -50^\circ, 70^\circ, 30^\circ]$, $\vec{\theta}_f = [0^\circ, 0^\circ, 0^\circ, 0^\circ]$, 1000 Iterations, Dynamic and Kinematic Uncertainty.....	186
Figure 144a: Max Motor Voltage for $\vec{\theta}_0 = [-70^\circ, -50^\circ, 70^\circ, 30^\circ]$, $\vec{\theta}_f = [30^\circ, -135^\circ, 0^\circ, 15^\circ]$, 1000 Iterations, Dynamic and Kinematic Uncertainty.....	187
Figure 144b: Max Motor Voltage for $\vec{\theta}_0 = [-70^\circ, -50^\circ, 70^\circ, 30^\circ]$, $\vec{\theta}_f = [30^\circ, -135^\circ, 0^\circ, 15^\circ]$, 1000 Iterations, Dynamic and Kinematic Uncertainty.....	187
Figure 144c: Max Motor Voltage for $\vec{\theta}_0 = [-70^\circ, -50^\circ, 70^\circ, 30^\circ]$, $\vec{\theta}_f = [30^\circ, -135^\circ, 0^\circ, 15^\circ]$, 1000 Iterations, Dynamic and Kinematic Uncertainty.....	187

LIST OF TABLES

Table 1: Failure Mode and Effects Analysis.....	36
Table 2: Robotic Components, First Order Selection.....	38
Table 3: Shoulder and Elbow Assembly Parts List.....	42
Table 4: Bicep Assembly Parts List.....	44
Table 5: Forearm and Wrist Roll Assembly Parts List.....	47
Table 6: Wrist Pitch Assembly Parts List.....	49
Table 7: End Effector Assembly Parts List.....	51
Table 8: Exponential Coordinate Terms for the 4 DOF Manipulator.....	63
Table 9: Preliminary Torque Analysis Results.....	80
Table 10: Model Validation Root-Mean-Squared Errors.....	94
Table 11: Motor Model Validation Results.....	102
Table 12: Kinematic Uncertainty of $x_{0 \rightarrow 1}$	124
Table 13: Step Response Comparisons.....	135
Table 14: Kinematic Properties.....	145
Table 15: Dynamic Properties.....	149
Table 16: Uncertainty in Kinematic Parameter $y_{0 \rightarrow 1}$	182
Table 17: Uncertainty in Kinematic Parameter $z_{0 \rightarrow 1}$	183
Table 18: Uncertainty in Kinematic Parameter L_1	183
Table 19: Uncertainty in Kinematic Parameter L_2	184
Table 20: Uncertainty in Kinematic Parameter L_3	184

DESIGN OF A CUSTOMIZED, SEMI-AUTONOMOUS, SINGLE ARM ROBOTIC MANIPULATOR FOR A HAZARDOUS ENVIRONMENT

Andrew Gunn

Dr. A. Sherif El-Gizawy, Thesis Supervisor

ABSTRACT

The purpose of this project is to build upon past research to develop and implement a cost effective, reliable single-armed robotic manipulator that can be used to perform repetitive tasks in the radioactive environment of a hot-cell. Current practice often involves handling material through the use of mechanical manipulators that pass through the walls of the hot-cell. These can be very expensive and impractical for repetitive tasks. Low cost single-arm robots on the market either suffer adversely from the environment or are unreliable. High cost, more durable arms are too expensive to maintain or replace. This project explores designing a manipulator that is simple enough to maintain, inexpensive enough to replace, and reliable enough to perform its task adequately. These design criteria are used to develop a conceptual robotic manipulator design. A mathematical model of the manipulator is derived from the conceptual design. Numerical simulation is used to optimize the design, develop a control algorithm, and evaluate performance criteria. A prototype manipulator is constructed and tested, and physical measurements from the device are compared to predicted responses from the model. Design and construction of a customized semi-autonomous robotic manipulator is found to be cost effective and feasible.

Keywords: *Single-Arm Robot, Hazardous Environment, Semi-Autonomous*

CHAPTER 1: INTRODUCTION

1-1: Introduction and Background

The term “robot” is used to describe an electro-mechanical device that can autonomously, or semi-autonomously sense and interact with its environment. As computing technology advances, humans are developing an increasingly dependent relationship with robots, and applications for them can be found anywhere from the home, to the manufacturing industry, to research, to exploration [7,9]. Robots are very appealing for several reasons: first, they can offer a level of repeatable precision that cannot be manually achieved; second, they can work continuously for much longer durations than human workers; and third they have potential to work in environments that are unsuitable for human exposure or involve tasks that are beyond human capability. Over the past several decades, much effort has been channeled toward developing nuclear reactors as a source of clean and renewable energy, and a new niche for robots has presented itself here out of necessity to perform various tasks in environments contaminated by radiation. Robots have been in use in the nuclear power industry for some time, and there are numerous examples of their usage to perform maintenance, inspection, repair, and diagnostic evaluation inside nuclear reactors [11-14,19,21]. This project explores the development of such a robot with an emphasis on a design that is modular, customizable, semi-autonomous, reliable, and robust.

The target environment for this robot is a “hot-cell.” Shown in Fig. 1 below, this is a containment vessel commonly used in nuclear research facilities to hold radioactive material for study and analysis.



Figure 1: Hot Cell Radiation Containment Vessel.

Samples inside the hot-cell are handled by a technician looking through a leaded glass window that can be up to several feet thick to block high energy radiation. At the University of Missouri Research Reactor (MURR), hot cells are used to handle samples involved in radiopharmaceutical research, among other things [32]. Common practice for material handling inside hot cells at MURR is to use mechanical manipulators, like the ones shown in Fig. 1 and Fig. 2.

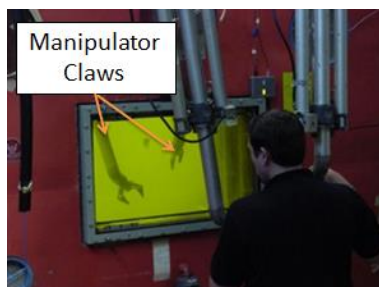


Figure 2: Hot Cell Manipulators.

These manipulators can be thought of as an extension of a user's hands through the walls of the vessel. They translate the three-dimensional motion and gripping action of the controls to a set of claws on the inside. These manipulators are well suited for accomplishing a wide variety of tasks and can be used with surprising dexterity by a highly skilled technician. However, due to the need for several feet of shielding material between the user and the manipulator claws, depth can be difficult to perceive, and this can result in clumsy movements and unwanted collisions with equipment. Furthermore, these feedthrough manipulators usually lack tactile feedback, making them somewhat risky for delicate operations, and ongoing or tedious tasks can become a strain on the operator. This project aims to address these issues with hot-cell material handling by introducing a semi-autonomous robot into the hot cell to supplement the manipulators and perform tasks that are difficult to accomplish with them.

1-2: Objectives and Motivation

The functionality of this robot does not aim to eclipse that of the manipulators, it is meant to share the hot-cell environment with them and perform the repetitive, precise, and delicate tasks for which it is better suited. The most appropriate configuration for a robot in a hot cell is an articulated, single-arm-robot. Single-arm-robots are well suited for confined spaces that may contain obstacles due to their ability to contort in a variety of ways depending on the number of joints that they have. This is useful for collision avoidance, end-effector positioning, and multi-task capability. Furthermore, many examples of successfully implemented articulated single-arm-robots used in hazardous

environments can be found in literature [12,14,19]. A two-dimensional schematic representation of the proposed new hot-cell layout can be seen in Fig. 3 below.

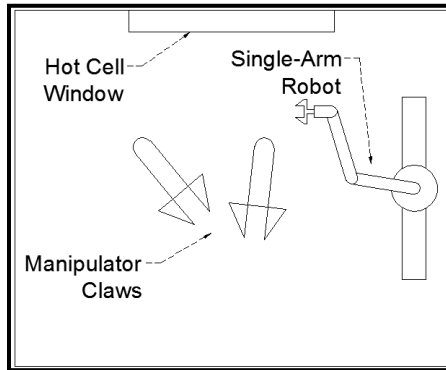


Figure 3: Conceptual Hot Cell Environment with a Single Arm Robot.

It is common knowledge that prolonged exposure to a radioactive environment will have an adverse effect on the health and functionality of the robot. Studies on the effects of ionizing radiation on robotic components and subsystems have revealed failure modes from malfunction of microprocessors and sensors [15,18], to loss of power, controllability and efficiency of motors [4,5]. The lifespan of the robot is a function of the total absorbed dose, which is a function of many parameters including radiation source, shielding, and configuration. Going forward in the design process, the harmful effects of radiation must be acknowledged and addressed. In order to be feasible, the robot will have to be semi-autonomous, simple in design, cost effective, reliable, and modular. This design project is approached with an understanding that eventual malfunction and failure inside the hot cell are likely, therefore the objective is to design a robot arm that is simple enough to be repaired in-house, cost effective enough to be fully

replaced, flexible enough to be reconfigured for different tasks, and reliable enough to perform its task adequately.

CHAPTER 2: LITERATURE REVIEW

2-1: Existing Research

There have been numerous research efforts to build and study the behavior and response of robots in nuclear reactor environments. In general, these robots are used for inspection and maintenance of areas inside reactors that are either too dangerous to inspect manually, or require lengthy and costly reactor shutdown to achieve. The IAEA (International Atomic Energy Agency) recommends the use of robots for these purposes as a means of minimizing human exposure and outage time [13]. At CANDU (Canada Deuterium-Uranium) reactors, an articulated-autonomous-robotic-manipulator (AARM), shown in Fig. 4, is used for inspection of the reaction cavity of the reactor [12].

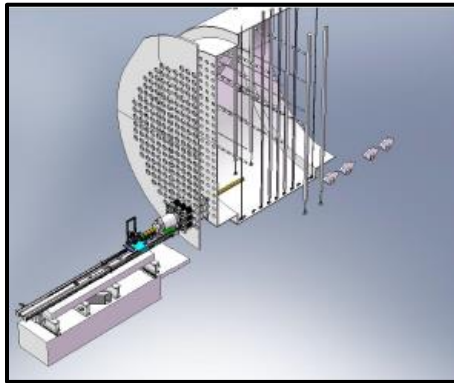


Figure 4: AARM Maintenance Robot [12].

During replacement of pressure and fuel lines, it becomes possible to insert the arm into this region to view otherwise inaccessible parts of the reactor. At the French CEA nuclear research facility at Cadarache, an articulated-inspection-robot (AIA) was designed and

built for insertion into the containment vessel of Tore Supra, an experimental fusion reactor [14]. This arm was subjected to an ultra-high vacuum and high temperature environment (1.4×10^{-5} Pa and 120 C respectively) during use, and could be outfitted with either an imaging system, or a “helium-sniffing” system at its end-effector to be used for inspection and leak detection of the reactor containment vessel walls.

Robots for highly specific applications have been used, such as the SADIE (Sizewell ‘A’ Duct Inspection Equipment) robot [21] which was designed to climb the interior walls of gas ducts inside the reactor containment area for inspection purposes. This tele-operated robot was designed to negotiate turns and corners in the ductwork and operate in any orientation. At Ontario’s Pickering Nuclear Generation Station, a single-task robot was designed and built to remove a high-activity radiation source found in a heat exchanger of the primary heat transfer system [11].

In addition to autonomous robots, “master-slave” robots have been used. At the AREVA La Hague nuclear fuel recycling facility in France, a user interface has been developed for using robot arms (including standard industrial arms) as slave manipulators [19]. Shown in Fig. 5, these are essentially an extension upon the standard mechanical manipulators described in the previous section. Their added benefits to the user include “force-feedback” to give the impression of touch, as well as visual information from imaging sensors mounted on the arm.

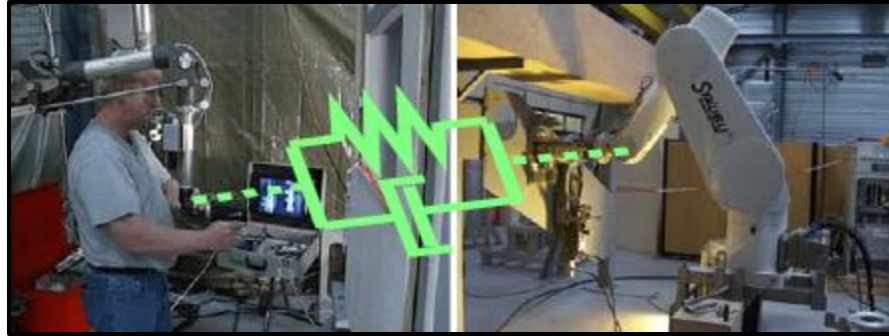


Figure 5: Tele-operated, Force-Feedback Manipulator [19].

In addition to nuclear reactor maintenance, robots have been used for clean-up and recovery operations in areas contaminated by nuclear disasters. A family of search and rescue robots named “Quince” were retrofitted and tested for exploratory missions within the contamination region of the Fukushima Daiichi Nuclear Plants after the earthquake and subsequent meltdown of 2011 [18,26]. The Quince robots, developed by NEDO (New Energy and Industrial Technology Development Organization), were tracked, multi-purpose, search and rescue robots with conventional electronics that had not previously been deployed in radioactive environments. These robots were desirable however, due to their high degree of mobility, and proven success rate in tele-operated situations. After laboratory testing of response to radiation, these robots were deployed into the disaster region and were able to carry out seven successful reconnaissance missions. Robots were also used to survey the damage resulting from the partial-meltdown accident at Three Mile Island. In response to this event, a surveillance and in-service inspection robot (SISO) and two rovers were deployed for imaging, dosage monitoring, and sample extraction.

There is a fairly extensive precedent for using robots in radioactive environments, suggesting that the concept is not only feasible, but attractive. The focus of this paper will be on defining yet another application for a robot in a nuclear facility and will highlight specific areas in which this research supplements that which has already been achieved.

2-2: Challenges Facing Robots in Radiation Environments

The primary challenge facing robots in radiation environments is the radiation itself. As previously stated, it introduces new failure modes to the main subsystems of the robot that must be considered in the design process. Interaction with energetic particles (alpha, beta, neutrons) or gamma rays can cause changes in the mechanical properties of materials that make up the robot structure or introduce faults into the electrical components and actuators that sense and drive the system. It is important to understand the sort of changes that might happen and account for them in the design of the robot.

The effects of ionizing radiation on electrical components (integrated circuits, microprocessors, etc.) have been well studied in recent years, motivated in large part by the ever-expanding space industry. NASA and other research organizations have focused much effort on developing electronics for communication satellites, space vehicles, and the International Space Station, that are resistant to cosmic radiation [16,17]. As robots have been used more and more in the nuclear industry, this research has expanded into studying the effects of terrestrial radiation on their sensitive on-board electronics [15,18,26,27]. Radiation damage to microelectronics, known as single-event-effects (SEE) or single-event-upset (SEU), occurs when a highly energetic particle strikes a

sensitive area of the device. SEU can have several different outcomes: it can have no observable effect, it can result in transient disruption in circuit operation, change of a logic state, or it can cause permanent structural damage to the device [15]. The mechanism for SEU is the ionizing nature of the incident particle or electromagnetic wave, which can cause unwanted charge accumulation on sensitive components of the integrated circuit (IC). This accumulation, and possible sudden discharge, can be the cause of any of the effects previously mentioned. The likelihood of failure of an electronic component is in general, a function of the radiation dose; however, studies have turned up a widely varying set of results that depend on specific radiation source, energy level, and orientation of the integrated circuit [27]. Studies done on standard (off-the-shelf) electronics have indicated radiation tolerance up to an absorbed dose of roughly 200 Gy to 10^4 Gy (where 1 Gy = 1 Gray = 100 Rad) [18,27]. Electronics that are designed to withstand prolonged exposure to radiation are called “radiation hardened” electronics. Various methods for radiation hardening have been researched and developed including the utilization of new radiation resistant semi-conductor materials, optimization of IC design for attenuating the effects of charge build-up and SEU, and even re-configuration of software algorithms for filtering out disturbances cause by radiation exposure [16,17].

On top of damage to robotic sensing and processing components, radiation causes physical damage to robotic actuators and structural components. DC motors are very common robotic actuators whose functionality and performance can be negatively affected by exposure to ionizing radiation. DC motors operate when current is applied to a coil of conductive wire within a magnetic field, thus generating a “Lorentz Force” on

the coil, which acts to rotate it. The speed and torque performances of a DC motor are largely dependent upon the strength of the magnetic field generated by its permanent magnets. Research indicates that radiation exposure over time can lead to magnetic field degradation in DC motors [4,5,6,20]. The degree to which the magnetic field is degraded is somewhat stochastic, and highly dependent upon situational factors such as intensity and type of radiation, presence of shielding material, orientation of the magnet, and angle of incident radiation [20]. Several studies have modeled radiation effects on DC motors for the specific purpose of analyzing how they might perform as components of a robotic manipulator in a hazardous environment [4,5]. These studies modeled radiation effects as random reductions in magnetic field strength, which affect the motor voltage and torque constants, and in turn, affect motor performance and efficiency. Several more studies have focused specifically on targeting samples of Nd-Fe-B (Neodymium-Iron-Boron) permanent magnets with X-ray, gamma ray, and fast-neutron radiation sources [6,20]. These studies suggest a widely varying degree of results, from 30-40% reduction in magnetic flux, to negligible loss of magnetic flux and suggest that effects are highly dependent on orientation of the sample magnet, incident angle of radiation beam, and ambient temperature.

From a design consideration standpoint, it is assumed that the radiation effects on the actuators of the robotic manipulator can be considered as stochastic and acting to reduce actuator power and efficiency. Over the course of duty of a robotic manipulator in a hot cell, the permanent magnets of the motors will be subject to varying radiation sources in many different orientations, as well as temperatures that vary with a high

degree of uncertainty, thus these effects must be treated as random variables in the design process.

Prolonged exposure to high energy radiation can cause changes in the mechanical properties of the materials that make up the structure of the manipulator. Radiation effects on metals, polymers, elastomers and composite materials have been well studied since the design and construction of nuclear reactors [30,31,33]. In metals, energy absorption from radiation can change the crystalline structure of the material and result in hardening, thus leading to embrittlement and reduction in fatigue strength. Temperature increase from energy absorption can also introduce heating effects such as creep [33]. In polymers, the fracture of molecules caused by incident high-energy particles, known as “chain scission,” can reduce material yield strength, and elasticity [33]. As in metals, one of the primary radiation effects on polymers is embrittlement and reduction of elongation percentage at fracture. Studies show that these properties can be preserved by introducing radiation tolerant material in the form of a compound. One such study found nearly 50% reductions in elongation percentage (at a total dose of 10 MGy) of a polymer commonly used in radiation-hazardous environments. With the introduction of as much as 25% alumina by volume, the composite, material could withstood nearly six times the original dose before the same reductions were seen [30]. As with metals, the coupled nature of radiation exposure and heating effects can cause material creep and reduction in tensile strength and flexibility [31].

Due to the high-risk nature of the operating environment of this robotic manipulator, and the diverse array of failure modes that are introduced by radiation, temperature, atmospheric composition etc. it is highly important that the design be

simple, modular, and mechanically robust. As the next section will point out, it is not realistically feasible to design a robot that will be immune to complications during the span of its useful life in a hot-cell. With this in mind, the design must consider how maintenance will be performed, and how likely failures will be dealt with, such that the lifespan of the manipulator can be extended even after damage has occurred.

2-3: Accuracy and Reliability in Hazardous Environment Robot Design

The accuracy of a robotic manipulator is the degree to which the robot is able to perform the task for which it was designed. If the robot's task is to locate an object, grasp the object, and move it to a new location, then the accuracy is related to how closely the robot is able to locate its end-effector (or tool) to the target area (initial and final object location). Reliability on the other hand, is the probability of failure of the manipulator over the course of its lifespan, and depends on many different variables that correspond to task, operating environment and physical manipulator structure.

The study of accuracy and reliability of a robotic manipulator in a hazardous environment is a key area of concern due to the numerous factors that could potentially cause failure, and the inaccessibility of the robot if failure does occur. Maintenance and repair to the manipulator is usually costly and dangerous, and may only be financially feasible to conduct several times over its lifespan. Studies have been done to identify methods and practices of improving the accuracy and reliability of robots in hazardous environments.

Robotic accuracy is a function of how precisely the physical parameters of the robot are known and how precisely the state of the robot can be measured. For an open-chain, rigid-link manipulator, accuracy is affected by uncertainties in angular position measurement and kinematic length. Small uncertainties and tolerances in the manufacturing and assembly process add up to produce an uncertainty margin in the major dimensions of the robot that result in tool position errors. Robotic accuracy analysis can be conducted analytically, or in the form of Monte Carlo simulation [23]. These studies produce a measure of the expected position error, and can be used in performance evaluation.

Robotic reliability is affected by many more parameters than robotic accuracy. This concept deals with the overall likelihood of failure and becomes increasingly complex as the number of components and subsystems in the robot increases. In open-chain manipulators, the failure of one subsystem can easily cascade to failure in other subsystems, thus it is important to identify faults before failure occurs, and compartmentalize damage if it does. The term “coverage” is introduced to describe the probability that a defect or failure in the robotic system is detected and dealt with such that the functionality of the robot is uninhibited [1]. In other words, a robot with a high degree of coverage can recover from failure either without human intervention, or with a moderate, non-invasive degree of which.

Several sources suggest that the best way to ensure coverage in a hazardous environment robot is to incorporate redundant physical systems into the design [1,22,24]. This can be achieved with kinematic redundancy and with redundant sensing. Kinematic redundancy is the situation in which the robotic manipulator has more degrees of freedom

than are necessary to perform its intended task [1]. For example, a two-link planar robot such as the one shown in Fig. 6a has roughly the same work envelope (area that the end-effector can reach) as the three-link planar robot shown in Fig. 6b. If a malfunction were to happen in one of the joints (joint $J1$ for instance) of the robot in Fig. 6a however, the work envelope of this robot would be significantly reduced. If the same malfunction were to happen to the robot in Fig. 6b, this manipulator would still be left with two degrees of freedom to work with in a two dimensional space, and therefore might still be able to perform its intended task.

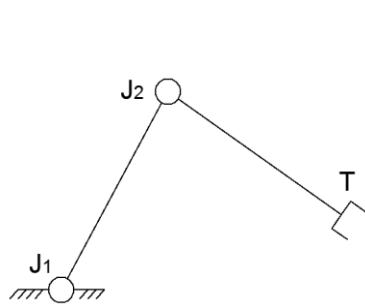


Figure 6a. Two Link Planar Robot.

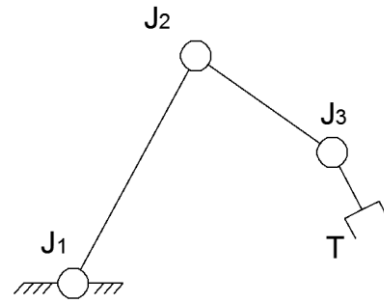


Figure 6b. Three Link Planar Robot.

Redundant sensing is a more intuitive concept; it is simply the practice of including more than the minimum number of sensors necessary to describe the state of the system. For the planar robots in Fig. 6a and 6b, this would mean configuring the design with multiple angular position sensors at each joint, thus reducing the probability of total position feedback loss from any particular joint. In addition to including redundant sensors and links into the design, a technique called analytic redundancy (AR) has been studied to improve reliability and fault resistance in manipulators [25,29]. AR is somewhat of a machine-learning principle in which state measurements are analyzed in real-time, and compared to model predictive and historical state measurements.

Discrepancies between the actual and predicted values are flagged by software and used to warn of potential fault.

Whether it is by physical or computational means, addressing accuracy and reliability in the design of the manipulator is of key importance in prolonging its useful life in the hot cell.

2-4 Building upon Existing Research

The concept of using robots as manipulators in areas contaminated by radiation is not a new one. Studies show a very wide range of applications in which robots have been successfully used, and the challenges facing these robots have been well documented and explored. In many cases, the required task and the specific environment in which the robot is needed dictate the design requirements and constraints. Therefore, each design and analysis is unique. The subject matter of this paper outlines the complete design cycle of a multi-purpose robotic manipulator for use in a hot-cell radiation environment.

The design process presented here includes some of the techniques and concepts presented in the research covered in this section, as well as several new ones available to our facilities. Specifically, this paper will highlight design conceptualization with an emphasis on a robust, simplistic, modular structure, development of a mathematical model of the unique design, and utilization of the model for control and accuracy analysis. The accuracy and reliability analysis presented here will consider radiation effects as well as manufacturing and assembly effects. A full report of the performance and feasibility of the robotic manipulator design will be presented

CHAPTER 3: PREVIOUS DESIGN ITERATIONS

3-1: Previous Design Iterations

At the University of Missouri – Columbia, the hot-cell robotic manipulator project has seen several iterations of design and testing. In the early stages of this project, a radiopharmaceutical production process at The University of Missouri Research Reactor (MURR) involving loading and unloading cylindrical vessels containing irradiated uranium foil into and out of a “disassembly” extraction device was identified as a task that could ideally be accomplished by a semi-autonomous robotic manipulator [34]. Due to its radioactive nature, this process had to be carried out in a hot-cell, and all operations had to be done using manipulators. Although mechanical manipulators were sufficient to accomplish the necessary maneuvers, continuous operation could quickly lead to operator fatigue and error. If the process were to be scaled up for a production environment where as many samples as possible would need to be processed in a timely manner, automation would be needed.

The first design iteration of the single-arm robotic manipulator, shown in Fig. 7, was developed to perform the ongoing repetitive act of grasping a target vessel from a rack, moving the vessel to the extraction device, waiting until the extraction process was complete, then moving the vessel to a secondary container for further processing.



Figure 7: First Iteration Single-Arm Robotic Manipulator.

This robot was designed to be semi-autonomous in that, it could perform its specific task without human intervention, but could not deviated from this task, or adapt to changes in the workspace environment. Equipped with six degrees of freedom, this manipulator could place its end-effector in any position and orientation in the vicinity of its guide-rail base.

Considering the limited mobility and functionality of this robot as an area for improvement, the second design iteration transitioned from a robot grounded on a stationary base, to a robot mounted on treads. The greatly enhanced degree of mobility of this robot and its ability to travel virtually anywhere in the workspace meant greater complexity in autonomous control algorithm design. As a result, this robot was designed to be directly controlled by a human operator via radio signal. This design featured two independently operated arms equipped with gripping mechanisms designed for handling the cylindrical tubes involved in the radiopharmaceutical process. This robot introduced a higher degree of versatility to the design because it could be used for other pick-and-place hot-cell tasks as well as the primary task. This second-iteration robot can be seen in Fig. 8 on the next page.



Figure 8: Second Iteration Dual-Arm Manipulator.

Though highly mobile and very versatile, the size and complexity of this robot design made its use in a hot-cell rather impractical.

In an attempt to simplify the design and improve upon the utilization of limited space, several more design iterations were attempted. Shown in Fig. 9a and 9b, key attributes of these designs included hot-cell wall mounting capability, very inexpensive, hobbyist grade actuators, fewer parts, and simpler assembly.

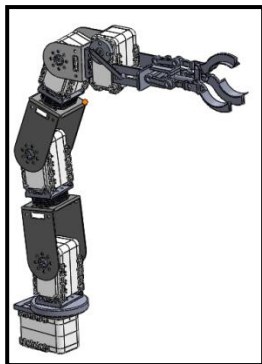


Figure 9a: Third Iteration Single-Arm Manipulator

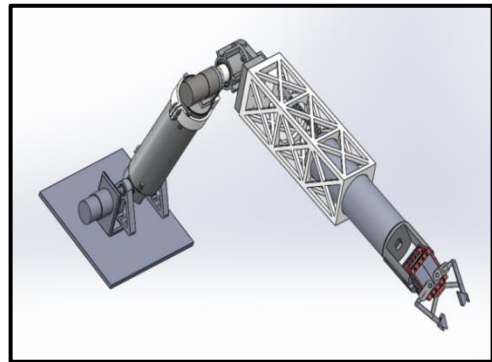


Figure 9b: Fourth Iteration Wall-Mounted Manipulator

3-2: Strengths and Weaknesses of Previous Designs

Strengths and weaknesses of the previous robot design iterations highlight areas that the design presented in this paper will build upon and address. The original objective presented in this paper is to design a robot arm that is simple enough to be repaired in-house, cost effective enough to be fully replaced, flexible enough to be reconfigured for different tasks, and reliable enough to perform its task adequately. The previous designs effectively satisfy cost and flexibility criteria with inexpensive actuators and structures composed primarily of polymer components made with rapid manufacturing technology. What makes these designs desirable is how simply they can be totally rebuilt and replaced. The structures of these robots are fabricated using an FDM (fusion deposition modelling) rapid manufacturing process, thus complex shapes and geometries can be used without added cost of fabrication. The sort of design intricacies that this process is capable of producing can be seen in each of the first four robot arm iterations from the streamline curves of the first iteration, to the economical, scaffold-type structure of the fourth. In addition, this process allows the freedom of unique end-effector design, a concept that is very valuable for a versatile robot. The material used in this process is a thermoplastic polymer, usually Polycarbonate or Acrylonitrile Butadiene Styrene (ABS). Low molecular weight and relatively high strength and structural rigidity make these materials attractive for robot design because they impose much smaller constraints on actuator selection than heavier materials. As a result, functionality is accomplished in these former designs using low cost servo-motors, which in most cases include built-in position controllers and are seamlessly compatible with numerous off-the-shelf

microcontrollers. In most dynamic system design situations, a detailed understanding of the forces and motions involved is critical to selecting actuators that satisfy design requirements. For a robot arm, the designer usually needs to know torque magnitudes at critical joints to ensure a motor with sufficient capability is selected. However, for the very lightweight structures of the previous iterations, the servo-motors with pre-programmed controllers are robust enough to execute the desired motion without detailed knowledge of the necessary torque. This allows for the design and construction of the system without developing a unique system model and control algorithm, which saves a lot of time in bringing the design to fruition.

While these designs are highly replaceable and can be re-configured for a high degree of versatility, they are not without several key limitations. Primarily, it is not well understood how the delicate structure of these designs will hold up to prolonged exposure to a radioactive environment. As examined in the previous chapter, studies indicate that many polymers suffer adversely to radiation and can become weak and brittle over time. Fabricated mostly out of plastic components, such damage would be detrimental to the health of these robots. Furthermore, the manufacturing process of these robots is highly susceptible to introducing inaccuracies into their assembly and functionality. The precision of the FDM rapid manufacturing facility available is limited, and resultant errors can cause miss-alignment of mating parts and error propagation in bulk dimensions. Such errors can inhibit assembly and motion of the robot, and will result in end-effector positioning error while the robot is trying to perform its task.

In addition to structural problems present in the former designs, there are issues with the dynamics that come as a result of using off-the-shelf microcontrollers and servo-

motors. Because these robots are designed without unique mathematical models, the dynamics in general, are not well understood. In robust design, it is important to conduct pre-fabrication testing and analysis with simulation. In this fashion, model responses and tendencies can be identified before the device is built and changes or repairs become much more costly and difficult. A major problem with these robots is that the motors do not “know” the required torque to transition from one point to another, and thus force the controller to base outputs solely on the error margin between current position and desired position. This causes motion that is not smooth, and sudden torque spikes from the motors that can damage the manipulator or its surroundings. Furthermore, accuracy and reliability analysis, as well as dynamic radiation effects of these manipulators can be greatly improved with aid of an accurate model because systematic changes to model parameters and iterative simulation can offer much insight into how certain parameters affect accuracy and performance.

The robotic design presented in this paper will incorporate the strengths of these previous designs and build upon their weaknesses for a more robust, accurate, and versatile design.

3-3: Building upon Previous Designs

The previous designs address the importance of a robot that is simple to re-fabricate and replace. In the conceptualization phase of this design, much attention will be paid toward maintaining a system design that is modular and can compartmentalize damage. In addition, the design will focus on maintaining versatility by means of end-

effector replacement capability. To keep maintenance and repair costs down, care will be taken to ensure that replacement parts for the new manipulator can be constructed using basic manufacturing capability and readily available materials.

The new design will feature large improvements in the areas of structural robustness and durability as well as dynamic understanding and controllability. The new design will seek to minimize the number of necessary components and the number of possible failure modes that can occur within the containment of the hot-cell. The remainder of this paper will describe in detail the design process of this iteration of the hot-cell robotic manipulator project from conceptualization, to structural modelling, to dynamic modelling, to simulation and analysis, and finally, to prototype construction and testing.

CHAPTER 4: CONCEPTUAL DESIGN

4-1: Design Assumptions and Simplification

The mechanical design of a robot is constrained and dictated by the task that it will perform and the environment that it will occupy. Robotic systems operate in a recursive loop of sensing, planning, and acting, as illustrated in Fig. 10 below.

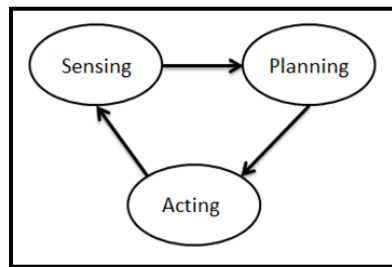


Figure 10: Robotic System Behavior Diagram.

Information is gathered from the environment via the robot's sensors and processed according to an algorithm that determines function. Then commands are sent to the system's actuators such that a desired function is carried out. Before design work can begin, the specific task and environment must be identified.

It is established that the robot will operate in the radioactive environment of a hot-cell, and perform tasks that are tedious, repetitive, and otherwise difficult to accomplish with feedthrough hot-cell manipulators. A key objective in the design is that the robot be versatile in a sense that it can be programmed to accomplish a wide array of miscellaneous tasks. With this in mind, the mechanical design of the robot cannot be so

specific that the functionality is limited. In addition, because the task presented to this robot may change, its native hot-cell environment may also change. It could potentially have to work around a varying collection of other equipment and obstacles. Taking all of this into consideration, the most efficient design for the robot is an articulated arm. This is a design that can be seen in many of the industrial radiation environment robots discussed earlier, as well as in the previous design iterations of this project, and even in the design of the feedthrough manipulators that are currently in use. It should be rather intuitive that this design makes the most sense for an unspecific task and environment; the articulated joints allow the robot to assume many different positions and orientations while avoiding potential obstacles. For a biological example, look no further than our own arms, which are essentially general purpose manipulation tools that do not have one *specific* task, but are very well suited for many different ones.

With the conceptual shape established, it is necessary to further refine the task for design analysis that will take place later on. Because the nature of the task is vague, it is assumed that the robot will simply locate an object within its workspace, move to a position where it can grasp the object, do so, and then move the object to a new location, as shown in Fig. 11 on the next page.

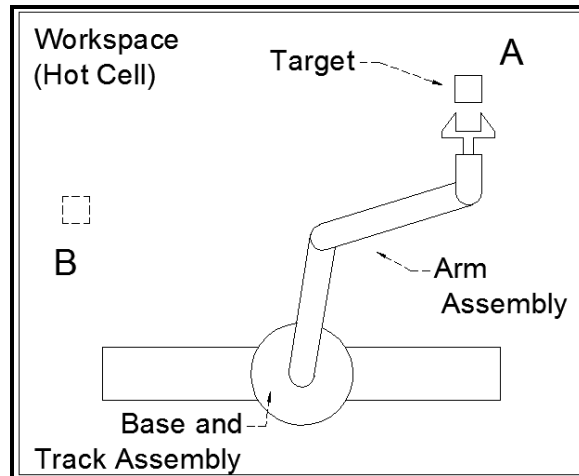


Figure 11: Single-Arm-Robot Basic Task.

Furthermore, it is assumed that the robot's workspace is clean and there is no risk of collision with an obstacle at any point during this task. In addition, the task is assumed to be path-independent, with the only constraint being that the object is located and moved to the right location.

In order to give the robotic manipulator the ability to grasp an object in any orientation, it is necessary for the design to contain at least six degrees of freedom (DOF). This owes to the number of coordinates that are required to describe the position and orientation of a rigid body in space (three coordinates that describe position, x , y , z perhaps, and three coordinates that describe orientation, *roll*, *pitch*, and *yaw* angles perhaps). There are many different ways in which a 6 DOF single-arm robot can be configured, but many of these involve two fundamental components, a 2 DOF base, and a 4 DOF articulated arm. The 2 DOF of the base generally correspond to freedom of motion on the surface upon which the robot operates, in this case, the floor of the hot cell. At any point in time, at least two coordinates are necessary to describe the position and orientation of the base in this region. Several different 2 DOF base configurations are

shown in Fig. 12 below. In terms of kinematic description, a joint can be either *prismatic* or *revolute* depending on the nature of its degree of freedom. A prismatic joint has a linear degree of freedom and is described by a measure of distance, whereas a revolute joint has a rotary degree of freedom and is described by a measure of angular rotation. The base configurations shown in Fig. 12 contain different combinations of these joints for slightly different functionality.

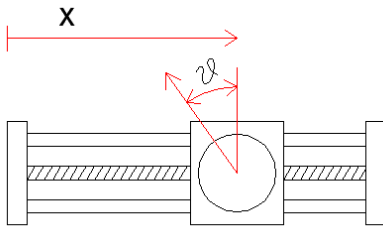


Figure 12a: Two DOF Base with Prismatic and Revolute Joint.

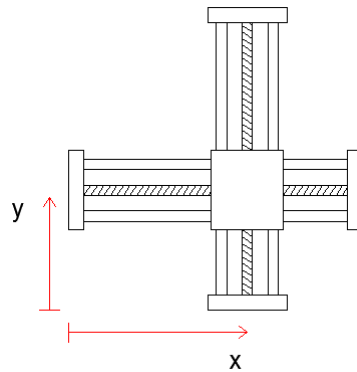


Figure 12b: Two DOF Base with Two Prismatic Joints.

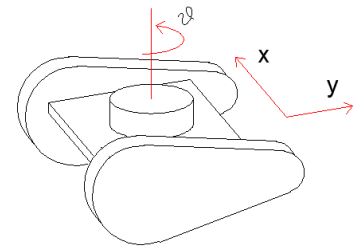


Figure 12c: Three DOF Base with Treads.

Several of these base designs have been successfully used in past iterations of this project. In modular robotic design, it should be possible to physically re-configure the robot for a variety of tasks. For example, it should be possible to take an articulated robot arm from a base like the one in Fig. 12a (and past iteration 1) and secure it to a base like the one in Fig. 12c (past iteration 2). In this way, the task of the robot can change without major mechanical alteration. Furthermore, if the task is assumed to be path-independent, it is possible to assume that the upper section of the arm can be held stationary while the

base of the arm is moving. If this assumption is obeyed, then the dynamic forces involved in moving the articulated, upper section of the arm will not affect the motion of the base. To obey this assumption, the robot will begin its pick-and-place task from an initial configuration, and once an object is detected in the workspace, the base of the arm will move the system into a position in which the upper arm can reach it (the upper arm will not move during this process). Once the base is in position, the upper arm will activate and grasp the object, then return to a retracted position, allowing the base to move to the final location, at which point, the upper arm will deposit the object. This process is described in Fig. 13.

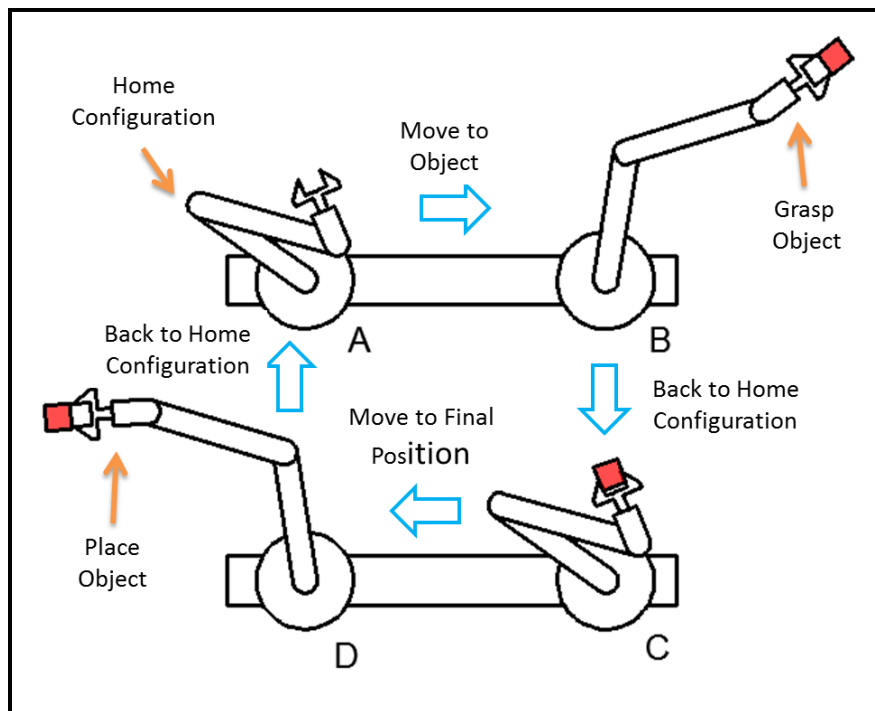


Figure 13: Single-Arm Robot Task Description.

Defining the task for the single-arm robot in this way means that the base design is arbitrary, and allows the design to focus only on the 4 DOF, articulated arm subsystem. The problem cannot be simplified any further than this because the dynamics of each joint in the 4 DOF arm are highly dependent on the dynamics of the other joints during motion. From this point forward, the design will focus solely on the design of the 4 DOF robotic arm subsystem, and all references to the single arm robot will be referring to this system.

4-2: Constraints and Objectives

Now that the single-arm-robot design has been simplified to a 4 DOF articulated arm, it is necessary to hone in on a specific design configuration. As mentioned before there are two basic types of joint in a rigid-link robotic manipulator, prismatic and revolute. The configurations of these joints in the “kinematic chain” (a term used to describe the robotic structure as a serial connection of joints and links) affect the shape of the manipulator workspace. The workspace, or work envelope of the robot is the set of all points in space that the end effector can reach. Several variations of 4 DOF manipulators with different configurations of prismatic and revolute joints can be seen in Fig. 14 on the next page. Prismatic joints are represented with a cube and a slide axis, whereas revolute joints are represented with a cylinder that rotates on its own axis.

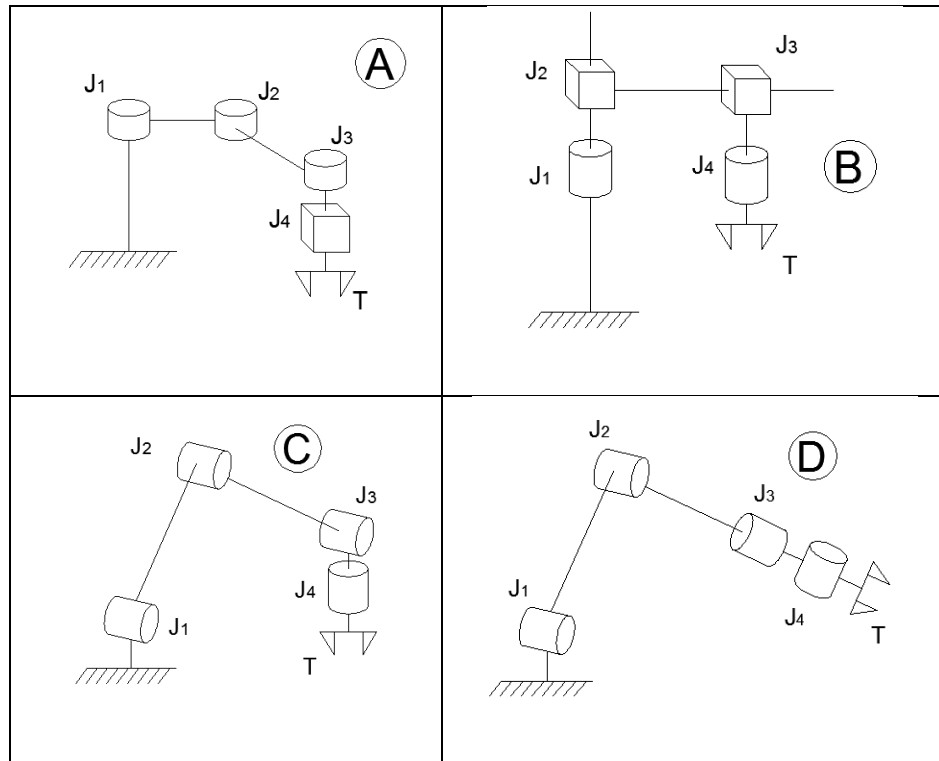


Figure 14: Various 4 DOF Manipulator Design Concepts.

Assuming that each of these manipulators are mounted onto a 2 DOF base, they will all be able to access roughly the same two-dimensional floor envelope, however they have different capabilities when it comes to grasping and handling objects in the vertical dimension (above the floor). The prismatic joints in manipulators A and B have the advantage of allowing these robots to change the length of some of their structural links. This allows them to execute motion that is much more complicated to achieve with designs C and D. Furthermore, the kinematic equations, which will be discussed in the next section, are much simpler for these designs because prismatic joints are described by a linear distance as opposed to an angle, and are therefore simpler mathematically.

Manipulators A and B are limited however, in that their vertical reach capabilities are absolutely constrained by the vertical positions of their J_1 and J_2 joints respectively. The maximum vertical tool position in manipulator A is met when J_4 is fully retracted towards J_3 , and by inspection, this can leave the tool no higher above the base than the height of joint J_1 . Also by inspection, it is clear that the maximum vertical tool position in manipulator B is met when J_2 is fully extended upwards. This aspect gives these manipulators a cylindrical shaped work envelope. In manipulators C and D, the vertical height of the tool is a function of the position of every joint. These manipulators have work envelopes in the shape of a half-sphere (assuming they are mounted on a flat plane below which they cannot reach). The approximate work envelopes of each manipulator configuration can be seen in Fig. 15. It should be noted that work envelopes shown for arms C and D in this figure assume the addition of a rotating base (which falls into the 2 DOF base assumption).

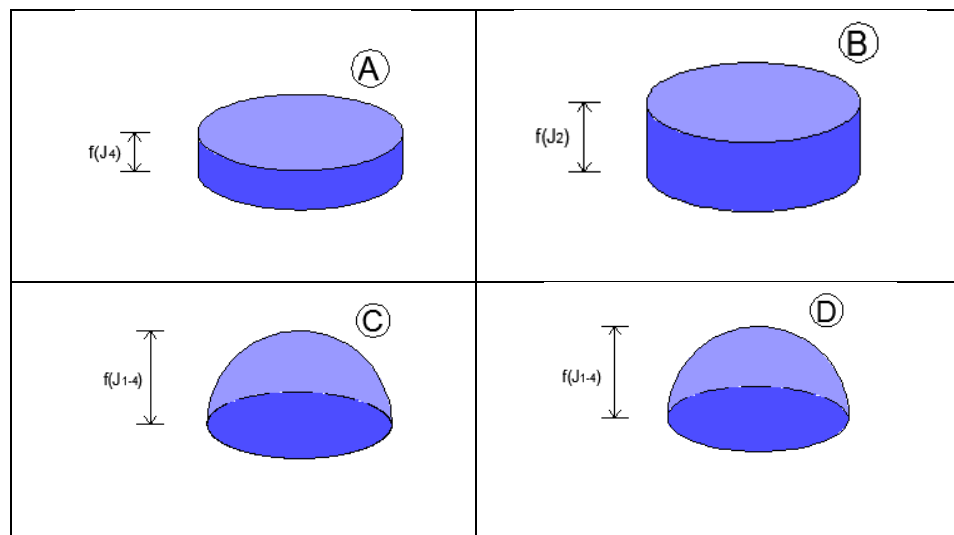


Figure 15: Approximate Work Envelopes of 4 DOF Manipulators.

The work envelopes for configurations A and B are similar, and those for C and D are identical (assuming that corresponding links are of equal length). If each of these manipulators is constructed with similar dimensions for corresponding links, it is clear that the workspace of C and D will enclose a larger volume than the “truncated” workspaces of A and B.

In addition to limitations on vertical tool position, arms A and B are limited in *how* they can grasp an object. If the design is to be versatile, the manipulator must be able to handle an object in many different orientations, and by inspection, it is evident that these manipulators can only grasp an object from above. This could be undesirable if obstacles are ever introduced into the workspace. Furthermore, prismatic joints are generally more mechanically complex than revolute joints (which are usually motor-actuated), and from a design simplicity standpoint are less attractive.

In terms of the design goals and objectives, manipulators C and D have more attractive work envelopes and joint configurations than A and B. The kinematic designs of these two manipulators are the same from the base to a point just before the 3rd joint, and differ only in the configuration of their wrist joints. The deciding factor in choosing a final conceptual design is the slight difference in manipulation capabilities of the wrists. Let the revolute joint whose axis of rotation coincides with the axis on which it is mounted be called the “roll” joint, and the revolute joint whose axis of rotation is perpendicular to its mounting axis be called the “pitch” joint. On manipulator C, the pitch joint is located before the roll joint in the kinematic chain (closer to the base). On manipulator D the order is flipped, and this produces a different “wrist work envelope.” The two work envelopes can be seen in Fig. 16 on the next page.

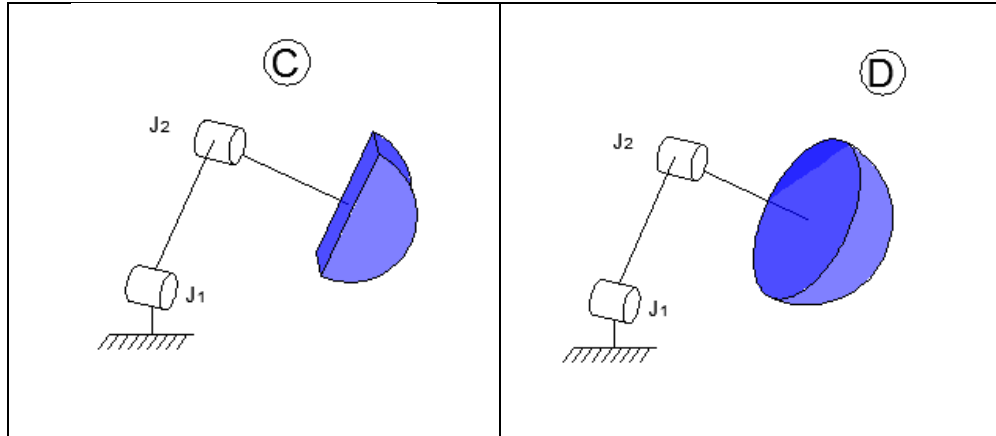


Figure 16: Wrist Work Envelopes of Manipulators C and D.

The wrist configuration of C constrains the end-effector to move in the half-cylinder shape shown in the figure, whereas the configuration D allows movement in the half-sphere. This slight reach advantage prompts the design to take on the configuration of manipulator D over manipulator C, and further design and analysis will be focused on this configuration.

With the basic configuration of the manipulator established, it is important to recall the objectives for the structural design and identify constraints. Primarily, the design must be modular, replaceable, cost effective, and robust. The end-effector must also be interchangeable for added versatility. It is important that components of the design be simple enough for in-house fabrication. The facility for which this robot is designed has access to basic machining capabilities including, milling, CNC, lathe, but advanced manufacturing techniques such as casting or cold working are not easily available and would result in a great deal of added cost. With this in mind, components must be designed for simple manufacturing. The device will likely require maintenance

in the hot-cell, and possibly replacement of key components. This requires a detailed design-for-simple-assembly approach. The next section presents the mechanical design of each component of the manipulator and will discuss the concepts and considerations that shaped them.

4-3: Satisfying Constraints and Objectives

The synthesis of the robotic manipulator is an iterative process that starts with selection of the fundamental components of a robotic system, sensors, processors, and actuators. It is necessary to make a rough selection of these components before modelling of the structural design can begin because they must be incorporated into that design. Furthermore, the size and shape of the actuators themselves will have a large effect on the dynamic forces generated during motion, and the actuators must be able to handle these forces while executing the desired task. As in any design process, this involves iterative design, simulation, performance evaluation and adjustment to achieve.

A reliability engineering technique for design formulation called *Failure Mode and Effect Analysis* (FMEA) is used as a brainstorming method for identifying the most important aspects in the design by their likelihood of failure coupled with the severity of such failure to the health of the system. The FMEA table for the single-arm hot-cell robot, shown in Table 1 on the next page, identifies all of the ways in which the device could conceivably fail during operation in the hot cell, and indicates the cause of failure, the system-level effect of failure, and the relative likelihood and severity of each failure on a scale from *very low* to *very high*. Failure events that are evaluated as moderate to

high likelihood *and* severity indicate areas in the design in which special attention must be paid toward reliability and robustness. In addition, a risk mitigation technique is presented for each failure to suggest how it will be accounted for in further design. The analysis presented in this table assumes that each joint is motor actuated, and has a position sensing element. It also assumes that one micro-processor is used as the controller for the device. The mechanical design is broken into sub-systems that include joints (shoulder, elbow, wrist roll, and wrist pitch) and links (bicep, forearm, wrist, end effector), as shown on Fig. 17 below.

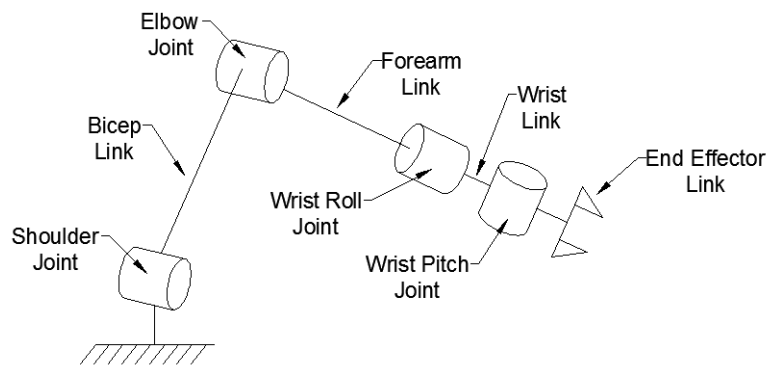


Figure 17: Single-Arm Robot Sub-Systems.

Furthermore, likelihood evaluation presented in the FMEA table assumes that all components are subject to the radioactive environment of the hot cell.

Failure Mode	Failure Sub-category	Specific Failure	Failure Cause	System Level Effect	Likelihood in Hot-Cell Over Useful Life	Severity	Risk Mitigation Technique	
Electrical Failure	Motor Failure	Shoulder Motor Stall	Max load Exceeded by Object or Own Structural Weight.	Motor Driver Over Current. Potential Burn Out. Loss of Control.	Moderate	Very High	Analysis of Dynamic Forces and Lifting Capability	
			Collision	Potential Structural Damage.	Low	High	Clean Workspace, Design for Disturbance Rejection	
			Power Loss Due to Radiation Effects	Motor Driver Over Current. Potential Burn Out.	Low	High	Modular Design, Easily Replaceable Motor	
		Elbow Motor Stall	Max load Exceeded by Object or Own Structural Weight.	Motor Driver Over Current. Potential Burn Out. Loss of Control.	Moderate	Very High	Analysis of Dynamic Forces and Lifting Capability	
			Collision	Potential Structural Damage.	Moderate to Low	High	Clean Workspace, Design for Disturbance Rejection	
			Power Loss Due to Radiation Effects.	Motor Driver Over Current. Potential Burn Out.	Moderate to Low	High	Modular Design, Easily Replaceable Motor	
		Wrist Roll Motor Stall	Max load Exceeded by Object or Own Structural Weight.	Motor Driver Over Current. Potential Burn Out. Loss of Control.	Moderate	Moderate	Analysis of Dynamic Forces and Lifting Capability	
			Collision	Potential Structural Damage.	Low	Moderate to High	Clean Workspace, Design for Disturbance Rejection	
			Power Loss Due to Radiation Effects.	Motor Driver Over Current. Potential Burn Out.	Low	Moderate to High	Modular Design, Easily Replaceable Motor	
		Wrist Pitch Motor Stall	Max load Exceeded by Object or Own Structural Weight.	Motor Driver Over Current. Potential Burn Out. Loss of Control.	Moderate	Moderate	Analysis of Dynamic Forces and Lifting Capability	
			Collision	Potential Structural Damage	Low	Moderate to High	Clean Workspace, Design for Disturbance Rejection	
			Power Loss Due to Radiation Effects.	Motor Driver Over Current. Potential Burn Out.	Low	Moderate to High	Modular Design, Easily Replaceable Motor	
	Sensor Failure	Error or Loss of Shoulder Position	Radiation Damage to Sensing Element	Controller Over-Compensation. Unwanted Motor Actuation	High	Very High	Modular Design, Easily Replaceable Sensor. Redundant Sensing.	
		Error or Loss of Elbow Position	Radiation Damage to Sensing Element	Controller Over-Compensation. Unwanted Motor Actuation	High	Very High	Modular Design, Easily Replaceable Sensor. Redundant Sensing.	
		Error or Loss of Wrist Roll Position	Radiation Damage to Sensing Element	Controller Over-Compensation. Unwanted Motor Actuation	High	High	Modular Design, Easily Replaceable Sensor. Redundant Sensing.	
		Error or Loss of Wrist Pitch Position	Radiation Damage to Sensing Element	Controller Over-Compensation. Unwanted Motor Actuation	High	High	Modular Design, Easily Replaceable Sensor. Redundant Sensing.	
	Micro-processor Failure	Control Logic Error	Single Event Upset due to Radiation (SEU)	Loss of Control, Potential Unwanted Motor Actuation	High	Very High	Locate Processor Outside the Hot Cell	
		Loss of Power	SEU due to Radiation	Loss of Control, Potential Unwanted Motor Actuation	High	Very High	Locate Processor Outside the Hot Cell	
	Wiring	Disconnection	Entanglement on Obstacle	Loss of Sensing or Motor Power	Low	Very High	Desing Robust Wiring Harness	
			Entanglement due to System Motion	Loss of Sensing or Motor Power	Moderate	Very High	Desing Robust Wiring Harness	
	Mechanical Failure	Component Stress Fracture	Bicep Component	Overloading or Fatigue Weakening	Potential Collapse of the Arm	Low	Very High	Extensive Analysis and Testing, Inspection
			Forearm Component	Overloading or Fatigue Weakening	Potential Collapse of Forearm and Wrist	Very Low	High	Extensive Analysis and Testing, Inspection
			Wrist Component	Overloading or Fatigue Weakening	Potential Loss of Wrist Function	Low	Moderate	Extensive Analysis and Testing, Inspection
			End Effector Component	Overloading or Fatigue Weakening	Potential Loss of End Effector Function	Moderate	Moderate	Extensive Analysis and Testing, Inspection
Component Wear Damage		Shoulder Joint	Wear Between Shoulder Axel and Joint Housing	Increase in Friction and Motor Load. Potential Fracture	Moderate	Moderate to High	Observation and Inspection	
		Elbow Joint	Wear Between Shoulder Axel and Joint Housing	Increase in Friction and Motor Load. Potential Fracture	Moderate	Moderate to High	Observation and Inspection	
		Wrist Roll Joint	Wear Between Shoulder Axel and Joint Housing	Increase in Friction and Motor Load.	Moderate	Moderate	Observation and Inspection	
		Wrist Pitch Joint	Wear Between Shoulder Axel and Joint Housing	Increase in Friction and Motor Load.	Moderate	Moderate	Accessibility and Replaceability	
Component Radiation Damage		Plastic Component	Weakening or Embrittlemet from Radiation Exposure	Range from Structural Collapse to Localized Loss of Function	Moderate to High	Low to High	Limit Use of Plastics in Structurally Critical Areas	
		Metal Component	Weakening or Embrittlemet from Radiation Exposure	Range from Structural Collapse to Localized Loss of Function	Low	Low to Very High	Robust Design. Periodic Inspection	

Table 1: Failure Mode and Effects Analysis.

Inspection of this table reveals that the components that are most susceptible to failure from radiation damage *and* have a moderate to severe effect on the health of the system are the position sensing elements, the micro-processor, and all plastic structural components. The components that are most likely to suffer mechanical failure as a result of structural loading *and* have a moderated to severe impact on system functionality are the major load-bearing axles in the shoulder and elbow, and the motors in each joint.

In order to address each of these potential failures, the design absolutely needs redundant sensing elements at each joint, powerful and robust motors and joints, protection for the main processor, and limited use of plastics in structurally critical areas. In addition to these design elements, contingency must be achieved with simplicity for ease of repair and replacement of damaged components. The following table presents the first order selections for the robotic components of this design. These are in essence, initial guesses for what is needed to satisfy the engineering requirements derived from FMEA analysis, as well as design constraints and objectives.

Subsystem	Type	Specifications	Location	Reason for Selection
Actuating	24V Brushed DC Motor	3600 RPM, 0.1 Nm Rated. 0.67 Nm Stall Torque @ 24V. 850g Weight	Shoulder	Mechanically and electrically robust. high torque to weight ratio.
	91.12:1 Reduction Gearbox	24 Nm Rated Torque. 73% Efficiency	Shoulder	Enhance torque capability of shoulder joint.
	24V Brushed DC Motor	3600 RPM, 0.038 Nm Rated. 0.2 Nm Stall Torque @ 24V. 390g Weight	Elbow	Mechanically and electrically robust. high torque to weight ratio. Lighter than shoulder motor.
	91.12:1 Reduction Gearbox	24 Nm Rated Torque. 73% Efficiency	Elbow	Enhance torque capability of elbow joint.
	12V Brushed DC Gearmotors	1.55 Nm Stall Torque, 100RPM Free Run Speed @ 12V with 100:1 gear reduction.	Wrist Roll and Wrist Pivot	Mechanically and electrically robust. Inexpensive to replace.
Sensing	Hall Effect Sensors with NdFeB Magnets	0-4.65V Analog Output	Shoulder and Elbow	Mechanically independent. Simple to replace. Several used at each Joint for redundancy.
	Hall Effect Encoders built into 12V Gearmotors	16cpr of motor shaft (2096 cpr or output shaft)	Wrist Roll and Wrist Pivot	Small spaces around wrist make other methods difficult. Wrist motors can be economically replaced if needed. Sensor failure at wrist joints will have local effect.
Processing	LabVIEW USB-6251 DAQ Device	15 AI Channels, 2 AO Channels, 2 Counters, 24 DIO Channels.	External	Aquire sensor data and feed into LabVIEW program for the controller. Output control signal to actuators.
	LabVIEW 2016		Software	Virtual instrument for observing state of manipulator as well as block diagram programming platform for controller integration.

Table 2: Robotic Components, First Order Selection.

As shown in the table above, the design will feature powerful brushed DC motors as the actuators of each joint. This selection is made with two intentions, to achieve robustness with simplicity, and to ensure enough available torque for reliable motion execution, versatile task capability and low probability of stall. The sensing elements for the shoulder and elbow joints will be hall-effect proximity sensors mounted to the housing block of each joint that are triggered by a magnet embedded in each rotating link.

This selection is intended to achieve redundancy, as multiple sensors will be needed to capture the full range of motion of each joint, and ease of replacement. Wrist position sensing will be achieved with encoders that are embedded into the wrist motor design. Redundant sensors are not included in the design on the wrist at this point due to the lack of space in this region for mechanically independent sensing, however the inexpensive nature of the wrist actuators and ease with which they can be replaced make it feasible to couple actuating and sensing in this area. The processing facet of the design will be accomplished using an Analog/Digital Data Acquisition Device (DAQ) and LabVIEW™ software. The DAQ will acquire signal inputs from the sensors, the software will apply the control algorithm to the input, calculate appropriate output, and the DAQ will generate the output signal for the actuators.

Designing the structure of the robot arm to incorporate all of the selected components is an iterative process that is accomplished using SOLIDWORKS™ 3-D modelling software. First, the geometry of the sensors and actuators are modelled, then the structural and motion concepts presented in Section 4-2 are considered, and a virtual model of the device is pieced together around the sensors and actuators, using a combination of custom-designed components and off-the-shelf available ones. The remainder of this section will describe the complete, virtual mechanical design of each robot arm sub-assembly and describe how they meet design requirements.

4-3-1: Shoulder and Elbow Design

The shoulder and elbow joints are the most important areas of the single-arm robot design from a mechanical standpoint. These are areas where some of the largest structural loading occurs and the necessity of motion results in large force and torque generation. These joints need to support the weight of the arm and permit smooth, rotary motion. In order to satisfy design simplicity requirements, as few components as possible are desired. The joints, sensors, and motors must be accessible for repair and maintenance. An exploded assembly view and cross section of the shoulder and elbow design can be seen in Fig. 18 and Fig. 19 respectively.

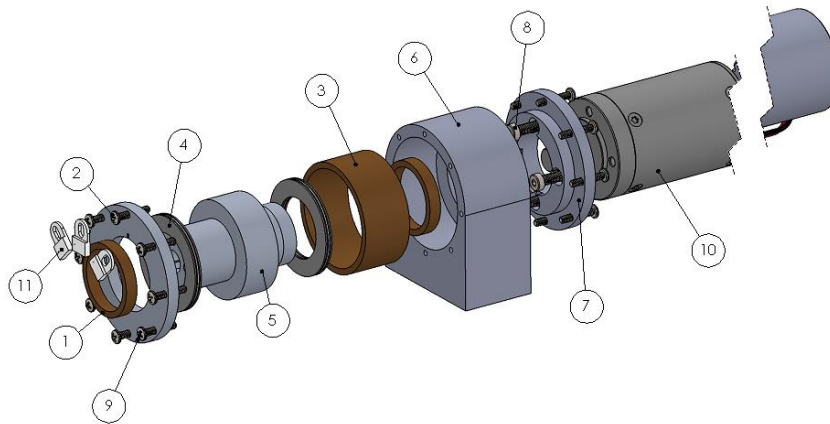


Figure 18: Shoulder and Elbow Assembly Exploded View.

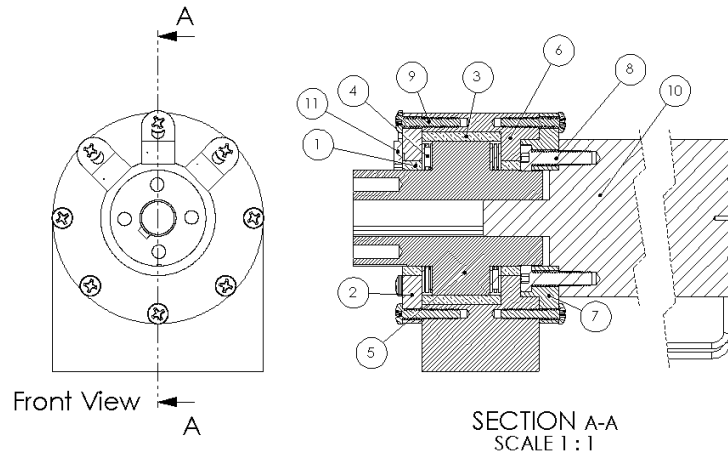


Figure 19: Shoulder and Elbow Assembly Cross Section.

One key feature of this design is that it is exactly the same for both joints. The only difference between the two designs are the sizes of the motors; however, both motors use the same in-line gearbox (*item 10*), and are thus identical from a mounting standpoint. Redundant physical design like this is efficient from a manufacturing perspective because the majority of time spent in custom manufacturing is often a result of setting up equipment for a specific type of machining process. Once the machine is set and calibrated however, manufacture of multiple components can usually be done relatively quickly.

Design accessibility is achieved with screw-fastened access plates, denoted *items 2 and 7*, which can be removed to expose the joint axle and motor respectively. Wear resistance and robust design is addressed with bronze bushings (*items 1 and 3*) between the joint axle and the housing block. These are used in place of ball bearings (which usually contain plastic races and rubber seals for holding the balls) for enhanced radiation

resistance. In the event of wear to either the bushing or the axle, the joint can be accessed, and these parts can be replaced.

Redundant sensing is achieved here with Hall Effect proximity sensors (*item 11*), and a magnet (shown with the bicep design in the next sub-section). Three sensors are shown in Fig. 18 for angular position detection spanning roughly 180°. Although each of these sensors is needed for position measurement over the full range of motion, only one is needed for some degree of feedback. Therefore, in the event of one or two sensor failures, the robot can enter a “safeguarding” state where it will remain until the failed sensors are replaced.

A full list of parts for the shoulder and elbow assemblies can be found in Table 3 below.

Shoulder and Elbow Assembly		
Part #	Part Name	QTY (per assembly)
1	1.25" ID x 1.5" OD Bronze Bushing	2
2	Joint Cap Plate	1
3	2" ID x 2 1/4" OD Bronze Bushing	1
4	1 1/4" ID x 1 15/16" OD Needle Thrust Bearing	2
5	Axel	1
6	Joint Housing	1
7	Motor Access Plate	1
8	M5 x 20mm Low Profile Socket Head Cap Screw	4
9	#6-32 x 3/4" Machine Screw	16
10	Dunkermotoren Typ GR 53x30 w/ PLG 52 Gearbox (shoulder) Dunkermotoren Typ GR 42x25 w/ PLG 52 Gearbox (elbow)	1
11	Hall Effect Proximity Sensor	3

Table 3: Shoulder and Elbow Assembly Parts List.

4-3-2: Bicep Design

The bicep of the single-arm robot is the link connecting the shoulder to the elbow. Because this is a rigid-link manipulator, there is no relative motion between components that make up the link, thus it only needs to be structurally stiff and able to withstand the dynamic forces developed during motion. Considering the final kinematic design presented in Section 4-2, the only type of loading that the bicep link will undergo, is bending along its normal (lengthwise) axis in a plane perpendicular to shoulder and elbow axes. With this in mind the link must be shaped such that the bending moment of inertia in this direction is much greater than that in the transverse direction.

In addition to being structurally rigid, the bicep must be designed such that the elbow and shoulder joints can be easily removed for maintenance, and the length of the link can be adjustable for versatility. An exploded view of the bicep assembly can be seen in Fig. 20 below.

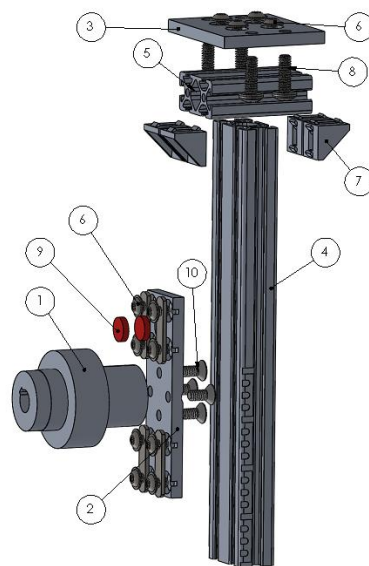


Figure 20: Bicep Link Assembly Exploded View.

The link is attached to the shoulder axle (*item 1*) via an adapter plate (*item 2*) as shown in the figure. The magnets (*item 9*), used to trigger the proximity sensors, are embedded into the adapter plate. The bicep link itself is made from prefabricated double T-slot extruded aluminum that is commonly used in structural framing applications. The component is oriented such that structural bending occurs about the double-wide cross section for rigidity. Connections can be made to the T-slot with either sliding, end-feed fasteners (*item 6*), or corner braces (*item 7*). End feed fasteners are used to connect the adapter plate to the bicep link so that its effective length (which is defined as the normal distance between the shoulder and elbow axes) can be changed by sliding the adapter plate along the link before tightening the fasteners. The etched pattern shown at the base of the link is used for visual identification of the adjusted length. The reference point for the kinematic length is the lower edge of the shoulder/bicep adapter plate. The elbow joint assembly is attached to the bicep via another adapter plate (*item 3*) and corner braces. A list of components used in the bicep assembly can be seen in Table 4 below.

Bicep Assembly		
Part #	Part Name	QTY
1	Shoulder Axel	-
2	Shoulder/Bicep Adapter Plate	1
3	Bicep/Elbow Adapter Plate	1
4	Bicep Link (Double 20mm T-Slot Framing Extrusion)	1
5	Bicep/Elbow Adapter Link (Double 20mm T-Slot Framing Extrusion)	1
6	Dual End-Feed Fastener for 20mm T-Slot	6
7	Corner Brace for 20mm T-Slot	4
8	1/4-20 x 3/4" Machine Screw	4
9	1/2" Diameter x 1/8" Thick NdFeB Magnet	2
10	#12-24 x 1/2" Flat Head Machine Screw	4

Table 4: Bicep Assembly Parts List.

4-3-3: Forearm and Wrist Design

The forearm design principles are very similar to those of the bicep. The link must be structurally rigid, adjustable, and easily assembled and disassembled. The forearm link itself will need to span a greater distance than the bicep link in order to make up for length limitations imposed on the bicep link due to torque constraints. For this reason, single T-slot extruded aluminum is used because it is lighter and will experience much less loading than the bicep. The different link geometry forces the elbow/forearm adapter plate (*item 3 of Fig. 21*) and its embedded magnet (*item 6 of Fig. 21*) to take on a slightly different shape. However, like the bicep, the length of the forearm can be adjusted by sliding the adapter plate along the T-slot. A length scale is also etched into the forearm for visual aid. An exploded assembly of the forearm can be seen in Fig. 21 on the next page.

The design of the wrist is a bit more intricate. Because the wrist assembly is attached to the elbow motor shaft by a long moment arm, the components here must be lightweight to prevent developing large torques in the elbow. Also, as indicated in the kinematic design concept, there are two joints included in the full wrist assembly, the wrist roll joint and the wrist pitch joint. These two joints must be allowed full range of motion without interfering with one another despite being located in close proximity.

For the wrist roll joint, the same basic design geometry used in the shoulder and elbow joints is scaled to a point in which it is compatible with the pre-selected wrist motors, and implemented. An assembly exploded view and cross section of the forearm

and wrist roll joint can be seen in Fig. 21 below and Fig. 22 on the following page respectively.

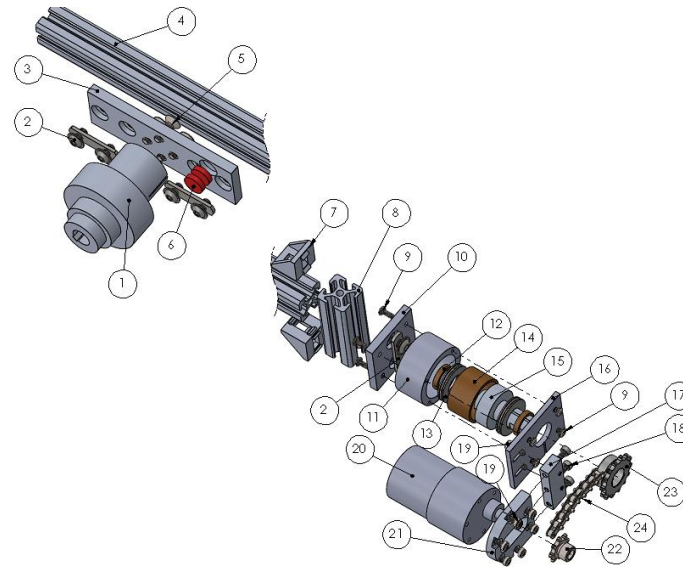


Figure 21: Forearm and Wrist Roll Assembly Exploded View.

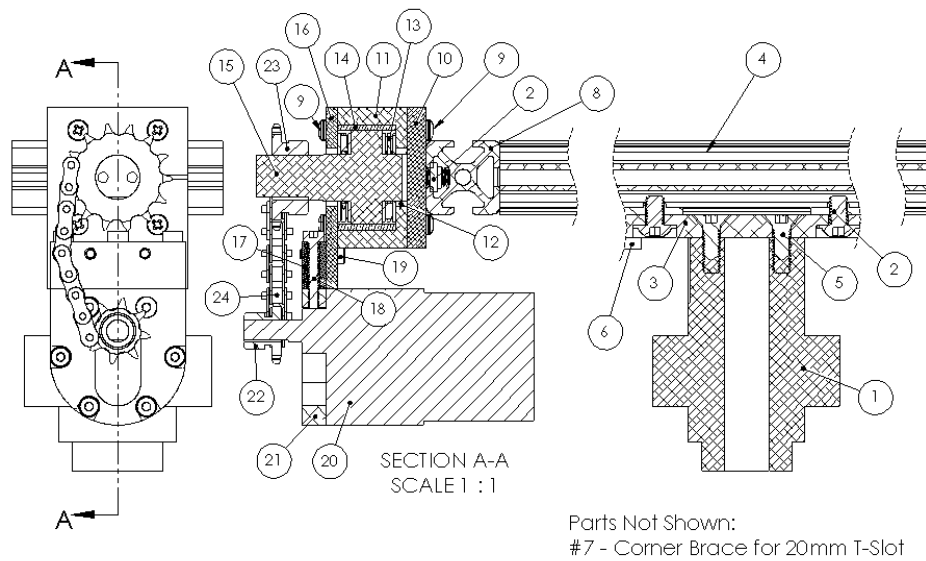


Figure 22: Forearm and Wrist Roll Assembly Cross Section.

The kinematic description of the manipulator is simplified if the axis of the wrist roll joint is collinear with the normal axis of the forearm link. In order to accomplish this while maintaining a degree of mechanical separation between the motor and the joint components, the motor is offset from the joint axis, and a chain and sprocket system (items 22-24 of Fig. 21 and 22) is used to connect to the motor shaft to the wrist roll axle. With this design, the motor can be replaced without the need to access the joint at all.

Wear resistance, radiation damage mitigation, and accessibility are achieved in the wrist roll joint in the same fashion as the shoulder and elbow joints, with bushings instead of plastic components, and screw-fastened joint access plates. A full list of components used in the forearm and wrist roll assembly can be seen in Table 5.

Forearm and Wrist Roll Assembly		
Part #	Part Name	QTY
1	Elbow Axle	-
2	Dual End-Feed Fastener for 20mm T-Slot	3
3	Elbow/Forearm Adapter Plate	1
4	Forearm Link (Single 20mm T-Slot Framing Extrusion)	1
5	#10-32 x 5/8" Flat Head Machine Screw	4
6	1/2" Diameter x 1/8" Thick NdFeB Magnet	2
7	Corner Brace for 20mm T-Slot	2
8	Forearm/Wrist Roll Adapter Link (Single 20mm T-Slot)	1
9	#4-40 x 3/4" Machine Screw	8
10	Forearm/Wrist Roll Adapter Plate	1
11	Wrist Roll Joint Housing	1
12	1/2" ID x 1/8" OD Bronze Bushing	2
13	1/2" ID x 15/16" OD Needle Thrust Bearing	2
14	1" ID x 1 1/8" OD Bronze Bushing	1
15	Wrist Roll Axle	1
16	Wrist Roll Joint Access Plate	1
17	Wrist Roll Pillow Block	1
18	M3 x 18mm Socket Head Cap Screw	3
19	M3 x 10mm Socket Head Cap Screw	8
20	Pololu 37D Gearmotor with 100:1 Gear Reduction	1
21	Pololu 37D Motor Mount Block	1
22	6mm Bore Sprocket	1
23	12mm Bore Sprocket	1
24	ISO #04B Metric Roller Chain	6"

Table 5: Forearm and Wrist Roll Assembly Parts List.

The wrist pitch joint is constructed in basic fashion, with a joint axle (*item 9 of Fig. 23*) that is directly connected to the motor shaft, and a housing block to hold the axle and motor in place. The entire wrist pitch joint must rotate with the wrist roll axle, thus the base of the wrist pitch housing block (*item 4 of Fig. 23*) is mounted directly onto the wrist roll axle (*item 1*). An exploded view of the wrist pitch assembly can be seen Fig. 23

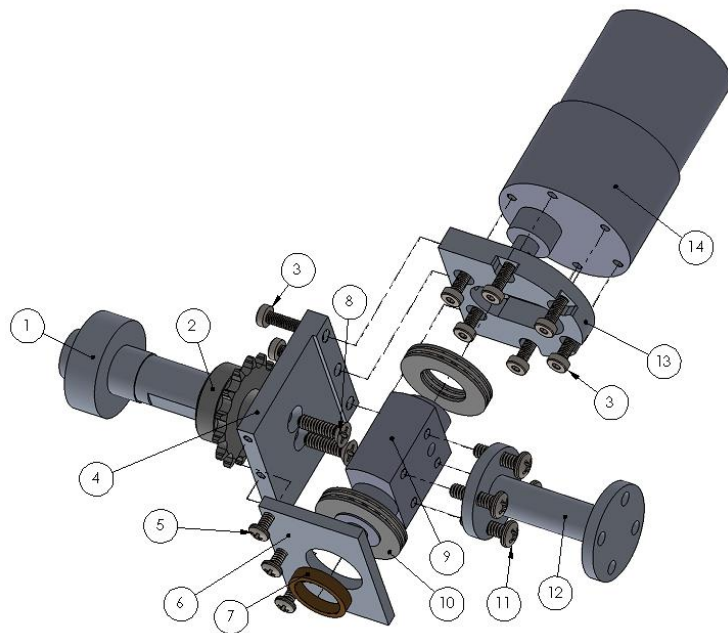


Figure 23: Wrist Pitch Assembly Exploded View.

The end effector is mounted directly to the end-effector mounting rod (*item 12*), allowing freedom of arbitrary end effector design and functionality. A full list of parts used in the wrist pitch assembly is shown in Table 6 below.

Wrist Pitch Assembly		
Part #	Part Name	QTY
1	Wrist Roll Axle	-
2	12mm ID Sprocket	-
3	M3 x 10mm Socket Head Cap Screw	9
4	Wrist Pitch Block Base	1
5	#4-40 x 3/4" Round Head Machine Screw	3
6	Wrist Pitch Block Wall	1
7	3/8" ID x 1/2" OD Bronze Bushing	1
8	#6-32 x 1/2" Flat Head Machine Screw	2
9	Wrist Pitch Axle	1
10	1/2" ID x 15/16" OD Needle Thrust Bearing	2
11	#6-32 x 1/2" Rounded Head Machine Screw	4
12	End Effector Mounting Rod	1
13	Pololu 37D Motor Mount	1
14	Pololu 37D Gearmotor 100:1 Reduction	1

Table 6: Wrist Pitch Assembly Parts List.

4-3-4: End Effector Design

The design of the end effector (or tool) of a robot is specific to the task that the robot will perform. Tools can have many different shapes and functions, but for the case of a general purpose, pick-and-place robot, a practical tool design is a simple pincher. One such pincher design with a solenoid actuator can be seen in exploded form in Fig. 24, and in standard form mounted onto the end effector mounting rod in Fig. 25 on the following page.

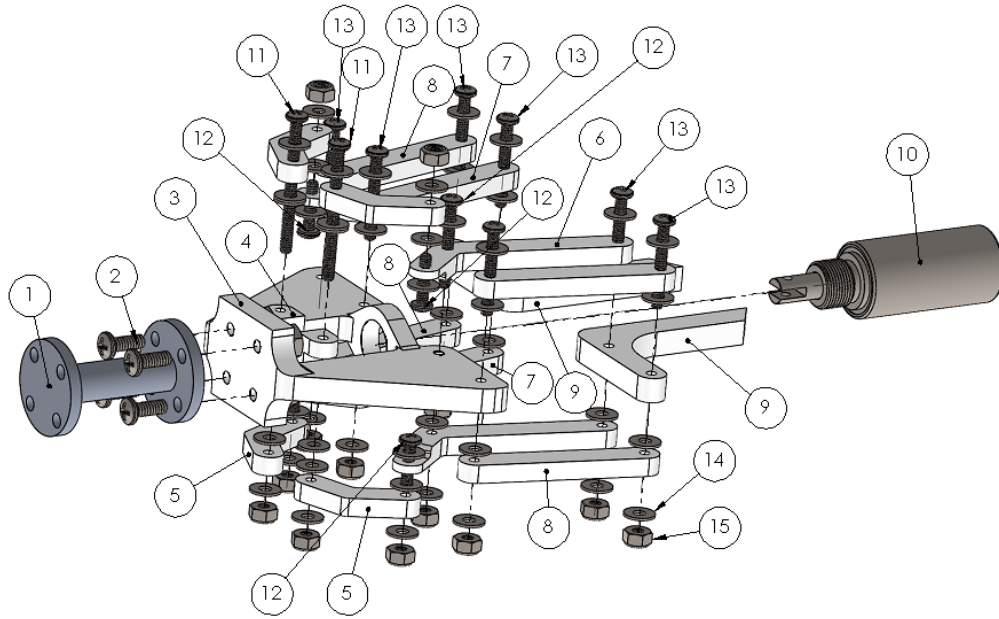


Figure 24: End Effector Assembly Exploded View.

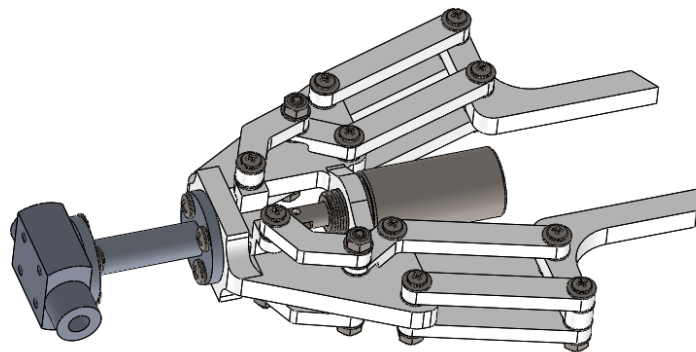


Figure 25: End Effector Assembled.

To accentuate the versatile nature of the end effector, the components are designed for rapid manufacturing using 3D printed polymers. Radiation damage to this material is neglected due to the simplicity with which the assembly can be replaced, and

the understanding that the tool design might need to change many times over the lifetime of the manipulator anyway due to change in task requirements. A list of parts used in the current pincher design can be seen in Table 7 below.

End Effector Assembly		
Part #	Part Name	QTY
1	End Effector Mounting Shaft	-
2	#6-32 x 3/8 Rounded Head Machine Screw	4
3	Ground Link	1
4	Coupler Link	1
5	Link 1	4
6	Link 2	2
7	Mirrored Link 2	2
8	Link 3	4
9	Pincher	2
10	Solenoid Actuator	1
11	#4-40 x 1 3/8" Rounded Head Machine Screw	2
12	#4-40 x 1/2" Rounded Head Machine Screw	4
13	#4-40 x 7/8" Rounded Head Machine Screw	8
14	#4 Washer	56
15	#4 Hex Lock Nut	16

Table 7: End Effector Assembly Parts List.

4-4: Final Mechanical Design

The fully assembled, mechanical design of the single-arm robotic manipulator can be seen in Fig. 26.

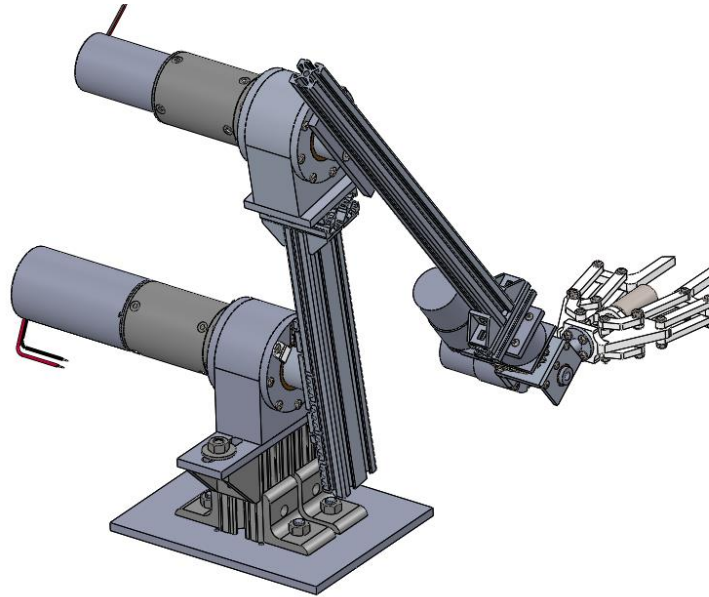


Figure 26: Fully Assembled, Single-Arm Robot Mechanical Design.

The shoulder joint is mounted to a stationary plate that represents the base. The four degrees of freedom and their kinematic configuration are preserved in this design and can be seen superimposed onto the mechanical design in Fig. 27 on the next page. The mechanical design, not including the motors, sensors or the end effector, consists of 20 custom machined components, 15 modified prefabricated components, and 112 prefabricated components (the vast majority of which are fasteners). This means that only 35 components must be machined for the four DOF system, thus achieving a high degree of simplicity.

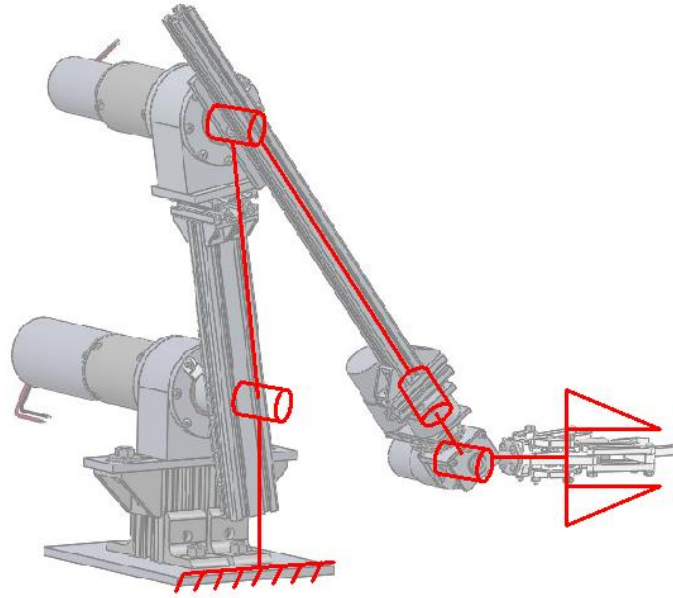


Figure 27: Mechanical Design with Kinematic Design Superimposed.

Now that a 4 DOF manipulator design is identified, the next phase of the process is to construct a model of the system that can be used in design analysis and evaluation. The next chapter will cover the development of this model.

CHAPTER 5: MODELLING AND ANALYSIS OF CONCEPTUAL DESIGN

5-1: Manipulator Kinematics and Inverse Kinematics

The previous chapter defined the shape and mechanical design of the single arm robot. The term “kinematic configuration” was used to describe the arrangement of joints and links as they relate to the function of the robot. In this section, the term “kinematics” will be used to describe the mathematical relationship between the manipulator joint angular positions and the position and orientation of the end effector. Eventually, a control algorithm will be developed to position the manipulator tool in a certain location so that it can perform a task, and it will be necessary to give positioning commands to the motors that will accomplish this.

Specifically, the robot arm kinematics will describe the position, velocity, and orientation of a reference coordinate frame attached to each link with respect to a stationary reference coordinate frame as a function of joint angular positions and velocities. For the remainder of this paper, the shoulder, elbow, wrist roll, and wrist pitch positions will be denoted $\theta_1, \theta_2, \theta_3$ and θ_4 respectively, and their angular velocities will be denoted $\dot{\theta}_1, \dot{\theta}_2, \dot{\theta}_3$ and $\dot{\theta}_4$. Before kinematic derivation can take place, it is necessary to define coordinate frames that are attached to ground, each link, and the end effector. The definition of the ground frame, which will be called the “base frame,” is arbitrary, and the position and orientation of all objects in the workspace of the robot will be defined with respect to this frame. The position and orientation of coordinate frames attached to the links and end effector will also be described with respect to the base frame. Let the *Z axis*

of the base frame point in the upward direction, let the X axis be parallel to the axes of the shoulder and elbow joints, and point in a the direction *outward* from the face of the motors, and let the Y axis complete a right-handed coordinate system (where the cross product of the X and Y unit vectors is the Z unit vector). This coordinate system, along with an arbitrary arm configuration, can be seen in Fig. 28 below.

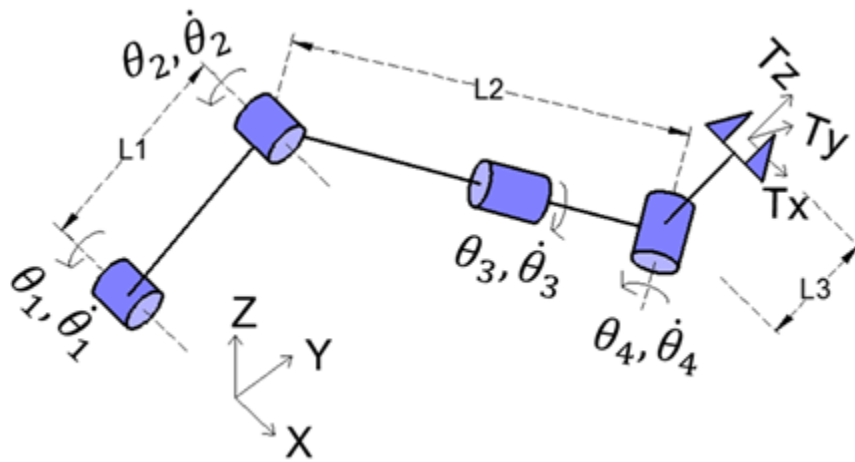


Figure 28: Definition of Kinematic Parameters.

The end effector body frame (represented $[T_x, T_y, T_z]$ in the figure), is defined such that the Z axis (T_z) points outward along Link 3, the X axis (T_x) points to the right when viewed from above, and the Y axis (T_y) completes a right-hand frame. The ultimate purpose of kinematic analysis is to develop a function that describes the position, velocity and orientation of $[T_x, T_y, T_z]$ with respect to the base frame $[X, Y, Z]$ as a function of joint angles and velocities. This is done by sequentially rotating and translating coordinate frames, starting from the base frame and passing through the frame of each link until ending up coincident with the end effector frame. The rotations of each frame

are functions of the joint angles $[\theta_1, \theta_2, \theta_3, \theta_4]$, and the translations are functions of the link lengths $[L_1, L_2, L_3]$.

The rotation of a coordinate frame in 3-dimensional space is accomplished with a *rotation matrix*. This is a 3x3 matrix whose columns are unit vectors that represent the axes of a new reference frame, expressed in an old one. For example if there are two right-handed frames, A and B , the rotation matrix of B with respect to (w.r.t) A (expressed R_{ab}) is a 3x3 matrix whose columns are the components of each axis of B expressed in the A frame. Furthermore, a vector expressed in terms of its coordinates in frame B , can be expressed in frame A by the following expression:

$$\vec{V}_a = R_{ab}\vec{V}_b \quad (5.1.1)$$

If an operation consists of a rotation as well as a translation, the mapping from one frame to another is described by a *homogeneous transformation matrix*. This is essentially a concatenated, 4x4 matrix containing a rotation matrix to describe the change in frame orientation, and a vector to describe the translation through 3-dimensional space, as shown in Eq. 5.1.2 below.

$$g_{ab} = \begin{bmatrix} R_{ab} & p_{ab} \\ 0 & 1 \end{bmatrix} \quad (5.1.2)$$

Further explanation of these concepts can be found in Reference [2], pages 23-25 and 35-36.

With the concept of a coordinate transformation matrix established, the derivation of the kinematic function can begin. There are several ways to define coordinate transformations along the kinematic chain of a manipulator. One popular, generalized method is to use Denavit-Hartenberg parameters [3]. This convention describes the position and orientation of reference frames that are attached to the intersections of joint axes and the common normal axes that connect them. Each link frame is expressed in global (3-dimensional) coordinates using four parameters: a displacement along the joint axis, a displacement along the common normal axis, a rotation about the joint axis, and a rotation about the common normal axis. Each of these parameters can either be a constant related to the geometry of the robot, or a variable related to its degree of mobility.

Another method for defining coordinate transformations, and the one that will be used in developing the kinematic equation of this robot, is the method of exponential coordinates and twists [2]. Exponential coordinates express transformations in terms of the definition of angular position and velocity of a point about an axis. Consider Fig. 29 below, where a point (q) is rotated with constant, unit angular velocity (ω) about a fixed axis.

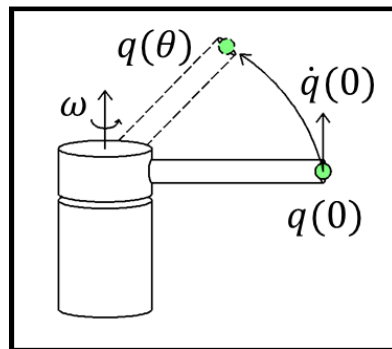


Figure 29: Exponential Coordinate Description.

The velocity of the point is expressed by the equation:

$$\dot{\vec{q}}(\theta) = \vec{\omega} \times \vec{q}(\theta) = \widehat{\omega} \vec{q}(\theta) \quad (5.1.3)$$

The unit angular velocity and subsequent point velocity calculation are used to describe the change in orientation of the point reference frame. The term $\widehat{\omega}$ is a cross product operator that is defined in [2], page 26. Equation 5.1.3 is a linear differential equation (where the dynamic variable is θ) that is easily solved to obtain the position and orientation of the point for any θ in the following fashion:

$$q(\theta) = e^{\widehat{\omega}\theta} q(0) \quad (5.1.4)$$

This equation has the same form as Eq. 5.1.1, where the term $e^{\widehat{\omega}\theta}$ is analogous to R_{ab} , and is a rotation matrix that is used to map the orientation of the point reference frame from its initial state to its final state. The Taylor Series Expansion of the exponential term is used to develop a closed form solution for the rotation matrix. For a robotic manipulator, the rotation matrix for each joint has the form:

$$e^{\widehat{\omega}_i \theta_i} = I + \widehat{\omega}_i \theta_i + \frac{\widehat{\omega}_i^2 \theta_i^2}{2!} + \frac{\widehat{\omega}_i^3 \theta_i^3}{3!} + \dots \quad (5.1.5)$$

The subscript i is used to express each joint in the kinematic chain of the manipulator. Because $\widehat{\omega}_i$ expresses a unit vector, odd and even powers of this term are a repeating

sequence, thus this equation can be rearranged and simplified to express a closed form solution for the rotation matrix (the details of which are described in [2], pages 27-28).

$$e^{\widehat{\omega}_i \theta_i} = I + \widehat{\omega}_i \sin(\theta_i) + \widehat{\omega}_i^2 (1 - \cos(\theta_i)) \quad (5.1.6)$$

This equation is called *Rodriguez's Formula* and will be used in developing the kinematic function for the robot. The final component necessary to describe the homogeneous transformation is the translational component. This is where *twist coordinates* come into play. A twist coordinate is defined as a 6-dimensional vector that contains the unit angular velocity *and* linear velocity components of a point in space. This coordinate is necessary in developing an equation that is analogous to equation to Eq. 5.1.3 for a case where a point is rotating about an axis that is *not* coincident with one of the axes of the reference frame in which it is defined. This concept is shown in Fig. 30 below.

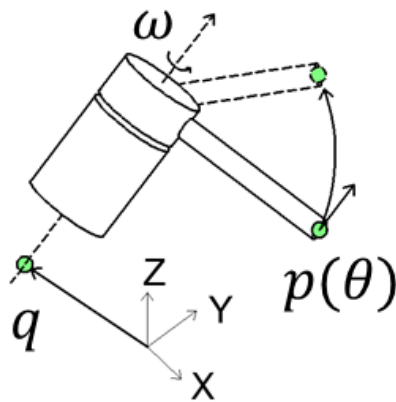


Figure 30: Description of Twist Coordinates.

The position of point p with respect to the reference frame shown $[X,Y,Z]$, can be computed by integration of the velocity equation:

$$\dot{\vec{p}}(\theta) = \vec{\omega} \times (\vec{p}(\theta) - \vec{q}) \quad (5.1.7)$$

The term q represents the coordinates of some point on the axis of rotation, expressed in $[X,Y,Z]$. The twist coordinate ξ is defined as:

$$\xi = \begin{bmatrix} \vec{v} \\ \vec{\omega} \end{bmatrix} \quad \text{where: } \vec{v} = -\vec{\omega} \times \vec{q} \quad (5.1.8)$$

and has the homogeneous representation:

$$\hat{\xi} = \begin{bmatrix} \hat{\omega} & \vec{v} \\ 0 & 0 \end{bmatrix} \quad (5.1.9)$$

The twist coordinate is used in order to write Eq. 5.1.7 in the form of Eq. 5.1.3 as follows:

$$\begin{bmatrix} \dot{\vec{p}} \\ 0 \end{bmatrix} = \begin{bmatrix} \hat{\omega} & -\vec{\omega} \times \vec{q} \\ 0 & 0 \end{bmatrix} \begin{bmatrix} \vec{p} \\ 1 \end{bmatrix} = \hat{\xi} \begin{bmatrix} \vec{p} \\ 1 \end{bmatrix} \rightarrow \dot{\vec{p}} = \hat{\xi} \vec{p} \quad (5.1.10)$$

After a somewhat extensive derivation (found in [2], pages 39-42), the homogeneous transformation matrix can be derived, and has the following form:

$$e^{\widehat{\xi}_i \theta_i} = \begin{bmatrix} e^{\widehat{\omega}_i \theta_i} & (1 - e^{\widehat{\omega}_i \theta_i})(\vec{\omega}_i \times \vec{v}_i) + \vec{\omega}_i \vec{\omega}_i^T \vec{v}_i \theta_i \\ 0 & 1 \end{bmatrix} \quad (5.1.11)$$

Where the subscripts i represent the homogeneous transformations associated with each joint in a kinematic chain as before. This homogeneous transformation does not give the position and orientation of a rotated and translated coordinate frame in absolute (base frame) coordinates. Rather, it gives the position and orientation of the transformed frame *with respect to* its initial position and orientation. For this reason, the initial transformation from the base frame to the tool frame ($g_{st}(0)$), of the manipulator must be known and expressed in base frame coordinates.

For an open-chain manipulator with n joints, the forward kinematics map from base frame to tool frame, $g_{st}(\vec{\theta})$, can be computed as the product of the homogeneous transformations specific to each joint (from 1 to n) and the initial homogeneous transformation from the base frame to the tool frame, $g_{st}(0)$, as describe below:

$$g_{st}(\vec{\theta}) = e^{\widehat{\xi}_1 \theta_1} e^{\widehat{\xi}_2 \theta_2} \dots e^{\widehat{\xi}_n \theta_n} g_{st}(0) \quad (5.1.12)$$

The reason exponential coordinates are so appealing is that they require just two pieces of information from each joint to describe the transformation of the manipulator from an initial state, to a new state. Observing Eq. 5.1.11, the only variables present are the joint variables, θ_i , the joint angular velocity directions, $\vec{\omega}_i$, and the velocity directions of the points on the axes of rotation, \vec{v}_i . The velocity terms are functions of the angular velocities and the locations of the axis points, \vec{q}_i , thus the forward kinematics map can be

fully obtained by defining the initial (reference) configuration directions of positive joint rotation, a point on the axis of rotation of each joint, and the initial homogeneous transformation from base frame to tool frame.

For the kinematic manipulator described in this paper, the Reference (Zero) Configuration is defined as a position in which all of the links are in-line and the axis of the wrist pitch motor is in the same direction as the axes of the shoulder and elbow motors as shown in Fig. 31.

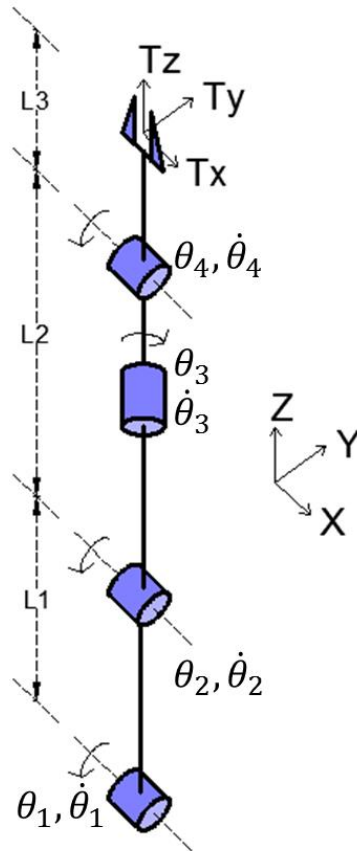


Figure 31: Four DOF Manipulator in Reference Configuration.

The directions of coordinate axes of the base frame for this manipulator are labeled $[X, Y, Z]$ in the figure, this frame remains fixed at all times and is defined to have an origin

located at the *front-middle* of the base plate on which the arm is mounted (see Fig. 26 for reference). The joint angular velocity unit vectors and axis point coordinates for this configuration, defined with respect to the base frame, can be seen in Table 8.

Joint	Angular Velocity Unit Vectors	Axis Point Coordinates
Shoulder	$\omega_1 = [1 \ 0 \ 0]^T$	$q_1 = [x_{0 \rightarrow 1} \ y_{0 \rightarrow 1} \ z_{0 \rightarrow 1}]^T$
Elbow	$\omega_2 = [1 \ 0 \ 0]^T$	$q_2 = [x_{0 \rightarrow 1} \ y_{0 \rightarrow 1} \ z_{0 \rightarrow 1} + L_1]^T$
Wrist Roll	$\omega_3 = [0 \ 0 \ 1]^T$	$q_3 = q_2$
Wrist Pitch	$\omega_4 = [1 \ 0 \ 0]^T$	$q_4 = [x_{0 \rightarrow 1} \ y_{0 \rightarrow 1} \ z_{0 \rightarrow 1} + L_1 + L_2]^T$

Table 8: Exponential Coordinate Terms for the 4 DOF Manipulator.

The direction of positive angular velocity is defined as counter-clockwise, and the direction of the angular velocity unit vector is defined by the right-hand-rule. From Fig. 31, it is clear that the angular velocity unit vectors for the shoulder, elbow, and wrist pitch joints are initially in the X direction, and the angular velocity unit vector for the wrist roll joint is initially in the Z direction. So far, the kinematic diagrams of the single-arm robot have suggested that all of the links reside in a plane when the wrist roll joint is held a 0° . This description is not 100% accurate with respect to the actual model, as joint and link geometries require offsets in the X direction. However, this schematic representation can be mapped onto the actual device if the points chosen to lie on the shoulder and elbow axes are directly below the origin of the tool reference frame in the reference configuration. The location of the shoulder reference point is fixed for any

rotation, $\vec{\theta}$, and it is defined as $[x_{0 \rightarrow 1} \ y_{0 \rightarrow 1} \ z_{0 \rightarrow 1}]$ in Table 8. Thus the initial homogeneous transformation from base frame to tool frame for the Reference Configuration is:

$$g_{st}(0) = \begin{bmatrix} 1 & 0 & 0 & x_{0 \rightarrow 1} \\ 0 & 1 & 0 & y_{0 \rightarrow 1} \\ 0 & 0 & 1 & z_{0 \rightarrow 1} + L_1 + L_2 + L_3 \\ 0 & 0 & 0 & 1 \end{bmatrix} \quad (5.1.13)$$

The 3x3 identity in the upper left-hand corner of this matrix indicates that the axes of the tool frame are initially aligned with the axes of the base frame. Furthermore, the initial X and Y locations of the tool frame are equal to the X and Y locations of the point defined on the shoulder axis. Thus in the initial configuration, the tool frame is merely translated in the Z direction. Using Eq. 5.1.8 and 5.1.11-5.1.12, the forward kinematic homogeneous transformation matrix for the robot is obtained. Computations related to the specific forward kinematics for this robot can be found in Appendix A.

With the forward kinematics, it is possible to iteratively build a picture of the work envelope of the manipulator by stepping through a range of joint angles and plotting the position of the end effector. This is valuable for the 4 DOF manipulator because it gives insight into what the work envelope of the manipulator will be if a base is added. Several views of the work envelope for this robot can be seen in Fig. 32 and 33 on the next page.

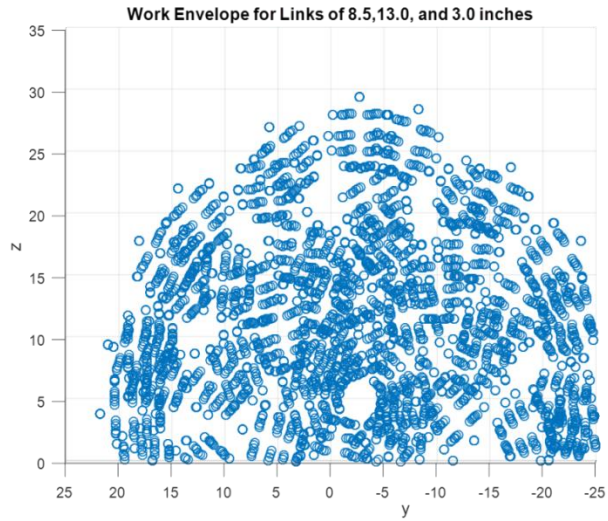


Figure 32: 4 DOF Manipulator Work Envelope Side View.

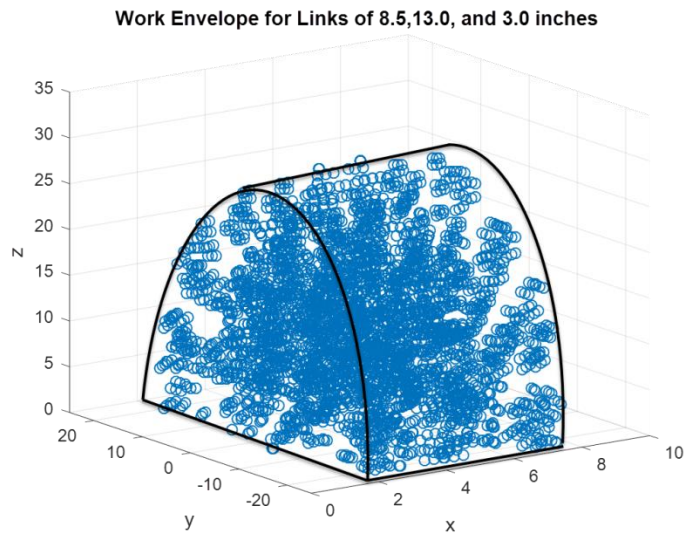


Figure 33: 4 DOF Manipulator Work Envelope Isometric View.

Essentially these plots show a “target region” where a separately controlled base must position itself with respect to an object in order for the robot arm to grasp it. This information could prove useful down the road if the task of the robot arm is adapted to

maneuver around obstacles, or if an optimal trajectory is required to map out an efficient route.

Where the forward kinematics of the manipulator describes tool position with respect to joint positions, *inverse kinematics* describes joint positions with respect to end effector position. The inverse kinematics problem involves computing the necessary joint angles and velocities required to achieve a desired tool position, velocity and orientation as shown.

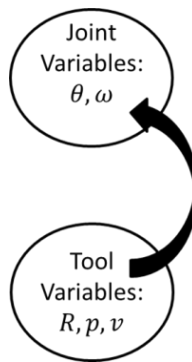


Figure 34: Concept of Inverse Kinematics.

This problem is obviously critical to robotic functionality because the way in which an object is found, grasped and handled is at the heart of accomplishing any task. The real complexity with solving inverse kinematics problems is that there can either be many different solutions (multiple configurations that locate the end effector in one position and orientation), one unique solution, or no solution at all. The problem definition starts with the homogeneous transformation from base to tool frame, $g_{st}(\vec{\theta})$, which is usually known as per the description of the robot's task (which can either be a predefined series of tool motions, or in the case of this design, locating an object and grasping it

autonomously). The kinematics provides a symbolic expression of this transformation in the form:

$$g_{st}(\vec{\theta}) = \begin{bmatrix} 3 \times 3 f(\vec{\theta}) & 3 \times 1 f(\vec{\theta}) \\ 1 \times 3 \text{ zeros} & 1 \end{bmatrix} \quad (5.1.14)$$

Therefore the problem consists of solving 12 non-linear equations in which there are 4 unknowns ($\theta_1, \theta_2, \theta_3, \theta_4$). This problem can be solved analytically, but a convenient method is to solve it numerically using least squares regression. This method is used for this design and it is implemented using built-in MATLAB™ and LabVIEW™ functions.

With the kinematics of the manipulator obtained, modelling can segue into the dynamics where rigid body masses and inertias are considered, and an investigation of the forces and torques acting on the structure is conducted.

5-2: Manipulator Dynamic Model

The dynamic model of the manipulator describes the *state* of the system (joint angles and velocities) as a function of external forces acting on it as well as link masses and inertia. A detailed description of the dynamics of the system is needed so that analysis of the conceptual design can be conducted via simulation, and adjustments can be made before fabrication and assembly. The model presented in this section is strictly concerned with the *mechanical arm dynamics*. At this point it is necessary to evaluate the strength of the arm structure and the capabilities of the motors to handle dynamic forces,

thus modelling of the motors will take place *after* the conceptual design is evaluated and it is determined that they can handle these forces.

5-2-1: First Iteration Dynamic Model

Derivation of the dynamic equations begins by adding the mass and center of mass (C.O.M) location of each link to the kinematic diagram as shown on the next page.

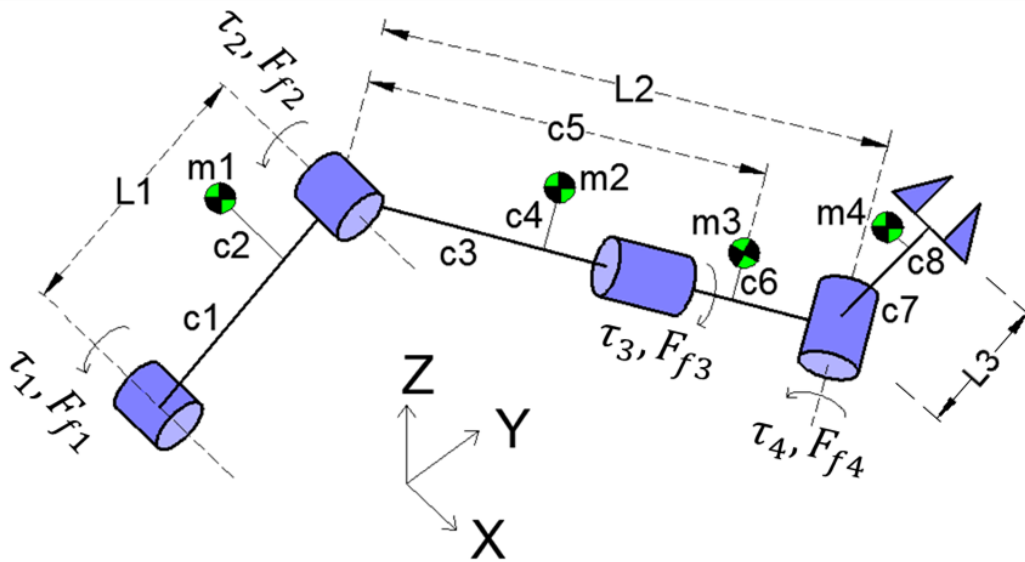


Figure 35: Schematic Diagram of Four DOF Manipulator with Link C.O.M.

External forces, including applied torques and friction forces are shown acting at the axis of each joint. Energy methods will be used later to formulate the equations of motion for the manipulator, thus expressions need to be developed for kinetic energy, potential energy, and non-conservative forces (friction) as functions of joint angles and velocities.

The kinetic energy of the entire robotic system, expressed $T(\vec{\theta}, \dot{\vec{\theta}})$, is composed of two components: the angular velocity of the joints, $\dot{\vec{\theta}}$, and the *Manipulator Inertia Matrix*, denoted $M(\vec{\theta})$, as shown:

$$T(\vec{\theta}, \dot{\vec{\theta}}) = \frac{1}{2} \dot{\vec{\theta}}^T M(\vec{\theta}) \dot{\vec{\theta}} \quad (5.2.1)$$

The Manipulator Inertia Matrix is analogous to the moment of inertia (usually expressed as I) for the rotational kinetic energy of a point mass about an axis. This matrix is a complete parameterization of the inertia of the system and is the sum of the inertias of each of the four links, as described by the following expression:

$$M(\vec{\theta}) = \sum_{i=1}^n J_i^T(\vec{\theta}) \mathfrak{m}_i J_i(\vec{\theta}) = J_1^T(\vec{\theta}) \mathfrak{m}_1 J_1(\vec{\theta}) + \dots + J_4^T(\vec{\theta}) \mathfrak{m}_4 J_4(\vec{\theta}) \quad (5.2.2)$$

The term, \mathfrak{m}_i , represents the “*Generalized Inertia Matrix*” of link i . Each 6x6 matrix \mathfrak{m}_i is composed of a 3x3 diagonal matrix in the upper left in which each element is the mass of the link, and a 3x3 *Inertia Tensor* matrix in the lower right, in which the rotational inertia of the link about each of its own major axes is described. If the major axes that describe the orientation of the link body are aligned with the principal axes of inertia of the link (axes in which the angular momentum vector of the rotating body is along the axis of rotation, such that “product of inertia” terms are all zero), then the Inertia Tensor

is a diagonal matrix containing the *principal moments of inertia*, and the Generalized Inertia Matrix has the following form:

$$\mathfrak{m}_i = \begin{bmatrix} m_i & 0 & 0 & 0 & 0 & 0 \\ 0 & m_i & 0 & 0 & 0 & 0 \\ 0 & 0 & m_i & 0 & 0 & 0 \\ & & & I_{xi} & 0 & 0 \\ & 0 & & 0 & I_{yi} & 0 \\ & & & 0 & 0 & I_{zi} \end{bmatrix} \quad (5.2.3)$$

The second term found in Eq. 5.2.2, $J_i(\vec{\theta})$, is called the “*Body Jacobian*” for link i . The Jacobian term describes the velocity and orientation of the link as a function of the velocities and orientations of the links “behind” it in the kinematic chain. This is a function of the homogeneous transformation from the base frame to a frame originating at the center of mass of each link and aligned with the principal axes of inertial of the link. The expression of the link Jacobian has the following form:

$$J_{sl_i}^b(\vec{\theta}) = [\xi_1^+ \dots \xi_i^+ 0 \dots 0] = J_i \quad (5.2.4)$$

where:

$$\xi_j^+ = Ad_{(e^{\xi_j \theta_j} \dots e^{\xi_i \theta_i} g_{sl_i(0)})}^{-1} \xi_j \quad j \leq i \quad (5.2.5)$$

The body Jacobians for each link are $6 \times n$ matrices (where n is the total number of links) that are constructed one at a time, starting with the first link, and whose columns are twist

coordinates (ξ_j^+) that describe the effect of the j^{th} link C.O.M velocity on the velocity of the i^{th} link. Equation 5.2.5 defines the twist coordinate as a function of the homogeneous transformation from the motion contributing link, j , to the current link, i . This transformation is a function of the initial position and orientation (expressed in the base frame) of a frame originating at the center of mass of the i^{th} link that has axes along the principal axes of inertia of the link, hence the term $g_{sl_i}(0)$ seen in Eq. 5.2.5. Starting with the first link it can be seen in Eq. 5.2.4 that the only contributor to the motion of this link, is its own joint rotation (i.e. rotation of joint 1), thus the last $n-1$ columns of the body Jacobian are zeros. The second link has a motion contribution from its own joint as well as from the first joint. The third has contribution from its own joint, as well as joints 1 and 2. This process is continued until a Jacobian is constructed for the last link in the chain (the Jacobian for this link will have no columns of zeros because its motion is function of the motion of every link in the chain). The Jacobians for this robotic manipulator are computed in this manner and can be found in Appendix B.

The potential energy of the manipulator, $V(\theta)$, is simply the total gravitational potential energy and is expressed as the sum of the potential energy of each link, as shown in Eq. 5.2.6 below.

$$V(\vec{\theta}) = \sum_{i=1}^n m_i g h_i(\vec{\theta}) \quad (5.2.6)$$

The term $h_i(\vec{\theta})$ represents the height of the C.O.M. of the link *above* a stationary reference point, which is taken as the origin of the base frame. Thus the height of the link

i C.O.M. can be obtained for any configuration of $\vec{\theta}$ using the Z -axis translation component of the homogeneous transformation matrix, $g_{sLi}(\vec{\theta})$, from the base frame to link i as described below.

$$g_{sLi}(\vec{\theta}) = e^{\widehat{\xi}_1 \theta_1} e^{\widehat{\xi}_2 \theta_2} \dots e^{\widehat{\xi}_i \theta_i} g_{sLi}(0) \quad (5.2.7)$$

With the total kinetic and potential energy of the manipulator described as functions of the state of the system, $(\vec{\theta}, \dot{\vec{\theta}})$, the *Lagrange Conservation of Energy Equations* are used to write the equations of motion as a function of externally applied and non-conservative forces. The *Lagrangian* is defined as the difference between the total kinetic and potential energy of the system as follows:

$$L(\vec{\theta}, \dot{\vec{\theta}}) = T - V = \frac{1}{2} \dot{\vec{\theta}}^T M(\vec{\theta}) \dot{\vec{\theta}} - V(\vec{\theta}) \quad (5.2.8)$$

Lagrange's Equation for describing the dynamics of a system in generalized coordinates has the form:

$$\frac{d}{dt} \frac{\partial L}{\partial \dot{\theta}_i} - \frac{\partial L}{\partial \theta_i} = \vec{Y}_i \quad (5.2.9)$$

The term \vec{Y}_i is used to describe applied and generalized forces (torques) acting on the i^{th} joint. After an extensive derivation, found in [2], pages 169-171, the equations of motion of the system are given in the following form:

$$M(\vec{\theta})\ddot{\vec{\theta}} + C(\vec{\theta}, \dot{\vec{\theta}})\dot{\vec{\theta}} + N(\vec{\theta}, \dot{\vec{\theta}}) = \vec{\tau} \quad (5.2.10)$$

In this matrix expression, $M(\vec{\theta})$ describes link inertias as covered earlier, $C(\vec{\theta}, \dot{\vec{\theta}})$ describes Coriolis Forces that are functions of relative link motions and moving axes of rotation, and $N(\vec{\theta}, \dot{\vec{\theta}})$ contains gravitational potential forces, and friction. The right-hand-side term, $\vec{\tau}$, represents the vector of externally applied torques acting on each joint that are either provided by the motors as control torques, or by loads placed upon the arm as a result of the task, collisions, etc.

Each term in Eq. 5.2.10 can be fully defined from mass and inertial properties obtained from the SOLIDWORKS™ model of the manipulator, with the exception of the friction component of $N(\vec{\theta}, \dot{\vec{\theta}})$. Friction in the joints of the arm is very difficult to describe and is highly dependent upon the assembly of the joint. For preliminary simulation and force evaluation, friction is modelled as simple, viscous friction in each joint by a friction coefficient attached to the angular velocity term of each joint in $\dot{\vec{\theta}}$. Estimates for inertial properties, mass, C.O.M. location, and principal axes orientation for each link are obtained from the SOLIDWORKS™ model of the manipulator for preliminary simulation. An example of this information related to the bicep link is shown in Fig. 36. A detailed presentation for each of the links can be found in Appendix B.

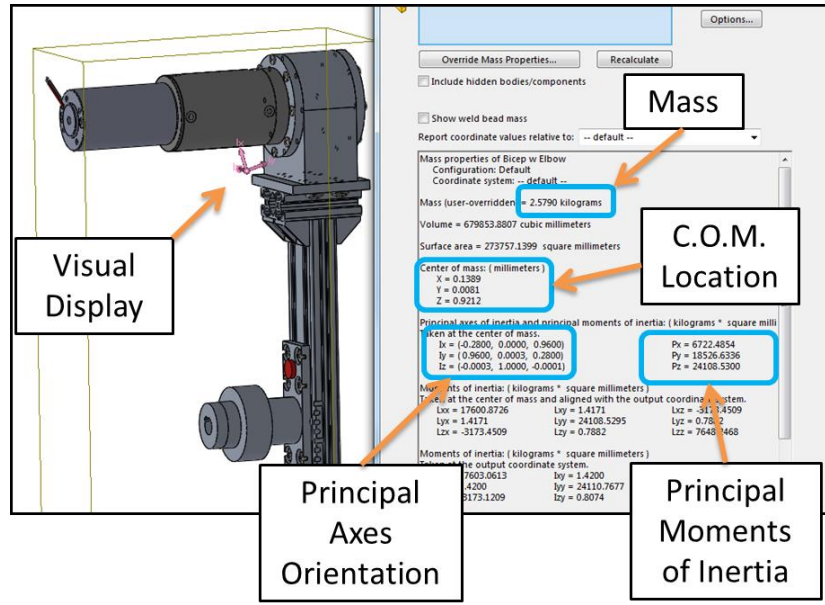


Figure 36: Bicep (Link 1) Dynamic Parameters from SOLIDWORKS™.

The dynamic model presented in Eq. 5.2.10 assumes that arbitrary torques can be commanded from the motors at each joint. The electro-mechanical dynamics of the motors are *not* included at this point in the design process because it is first necessary to determine whether or not the selected motors will be able to handle the loading that they will experience. Now that a completed description of the *arm dynamics* has been obtained, simulation can be used to estimate the forces present during operation, and an evaluation of the preliminary design can be conducted from the simulation results.

5-2-2: Simulation and Structural Evaluation.

The torque required for the manipulator to execute a motion from one configuration to another can be calculated directly from Eq. 5.2.10 if a *trajectory* $\vec{\theta}_{traj}(t)$ is defined for each joint from the initial angle to the final angle. The trajectory must be

twice differentiable such that joint angular velocity and acceleration can be computed with respect to time and substituted into Eq. 5.2.10 for $\dot{\vec{\theta}}$ and $\ddot{\vec{\theta}}$ respectively. Recall that the task for this robot arm is defined as path-independent, pick-and-place in a clean workspace. With this in mind, the trajectory defined for torque evaluation is somewhat arbitrary. The path should be defined such that it is realistic and passes through a set of configurations that simulate a maximum dynamic loading situation. There are two components necessary to define the trajectory: the initial and final angles for each joint, and the time it will take for the manipulator to travel from the initial configuration to the final one. The total travel affects the set of configurations that the system passes through and the travel time affects angular velocities and accelerations. Each in turn has a particular effect on the torque required to drive the system. In order to obtain a good estimate of the maximum joint torques required, the case in which the manipulator starts “hanging” in a downward position and transitions to a state described by $\vec{\theta}_f = [0^\circ, 90^\circ, 90^\circ, 90^\circ]$ is simulated and analyzed. Referring back to Fig. 31, this initial state is described by the set of joint angles: $\vec{\theta}_0 = [-180^\circ, 0^\circ, 0^\circ, 0^\circ]$ and is shown in blue in Fig. 37 on the next page. This transition is interesting because all links must move against gravity and inertia, thus it is a good example of a high-torque transition.

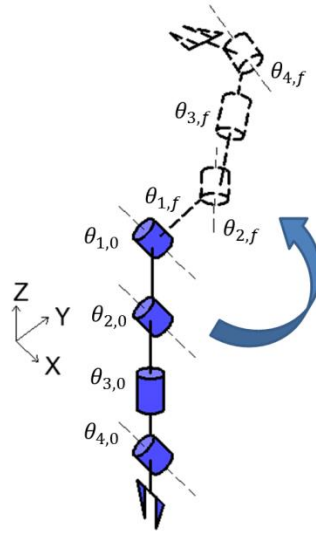


Figure 37: Initial Torque Evaluation State Transition.

Simulation of this movement using an arbitrary trajectory and Eq. 5.2.10 yields the necessary torque required to achieve the motion described by the trajectory for each joint. For concept illustration, an arbitrary travel time of 2 seconds is used in the first simulation to obtain results. Both the torque and trajectory expressions for the shoulder joint are plotted in Fig. 38 below.

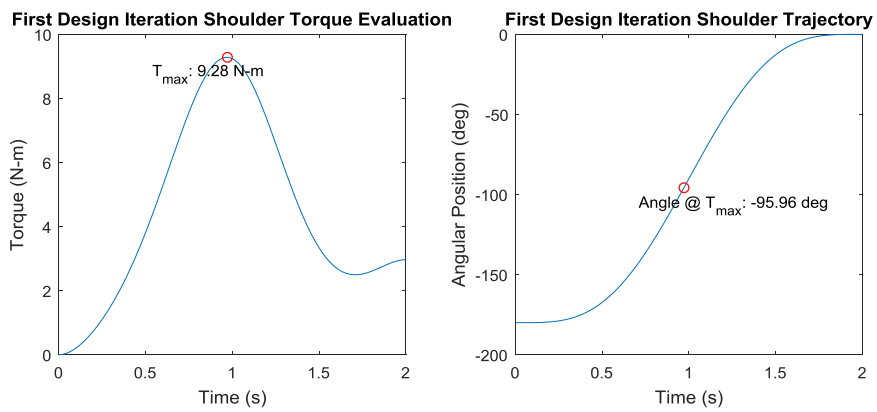


Figure 38: First Iteration Shoulder Torque Evaluation.

The maximum necessary torque can be identified for any set of trajectory and travel time specifications, and by varying these two components over several trials, their respective contributions to the maximum torque can be understood. Figures 39-41 show maximum torque as a function of travel time for three different trajectory cases.

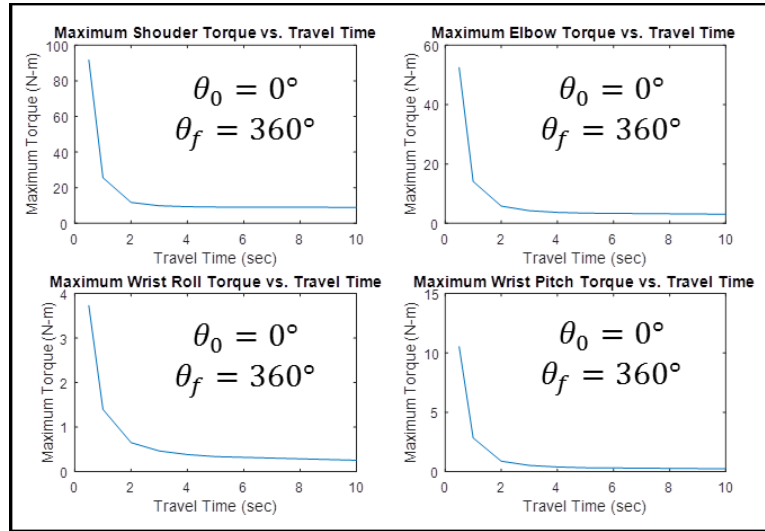


Figure 39: Torque vs. Travel Time Test 1.

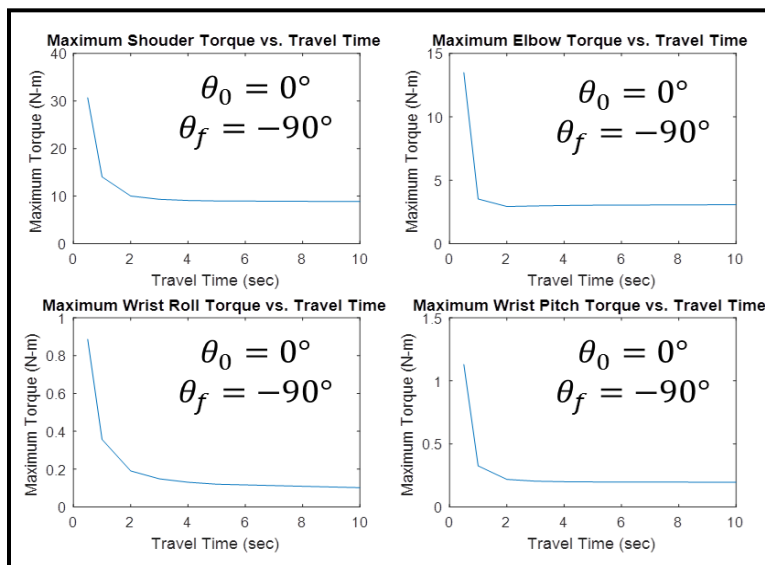


Figure 40: Torque vs. Travel Time Test 2.

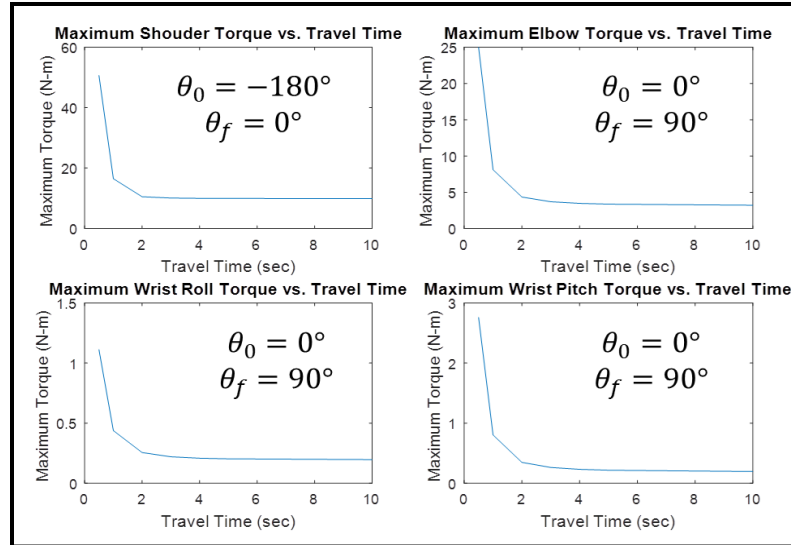


Figure 41: Torque vs. Travel Time Test 3.

It can be seen from these figures that for fast travel times (less than 1 second) the inertia of the system has a very large effect on the torque requirements. As travel time is increased, the inertial effects are rapidly diminished and the torque begins to converge to that required to overcome inertia, gravity and friction forces alone. For the purpose of picking and placing an object, it is assumed that travel times around 3 seconds are acceptable thus the majority of the torque requirement will arise from gravitational forces, and will be a function of the trajectory definition. With this in mind, a situation in which gravitational loading is at its peak must be analyzed to obtain an idea of worst-case structural integrity. Statically speaking, the highest loading occurs when the arm is in a fully horizontal configuration as shown in Fig. 42.

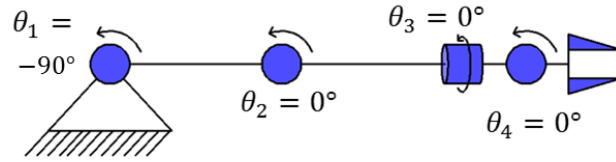


Figure 42: Manipulator in Static Horizontal Configuration.

If the manipulator starts in this configuration and heads toward a configuration in which all joints rotate against gravity (such as the Zero Configuration), and the travel time is greater than 3 seconds, then the loading will consist of a large component related to holding the manipulator in the static position and a smaller component necessary to start the motion. A good estimation of minimum actuator torque needed can be obtained from this simulation, and the results can be seen for the shoulder joint in the figure below.

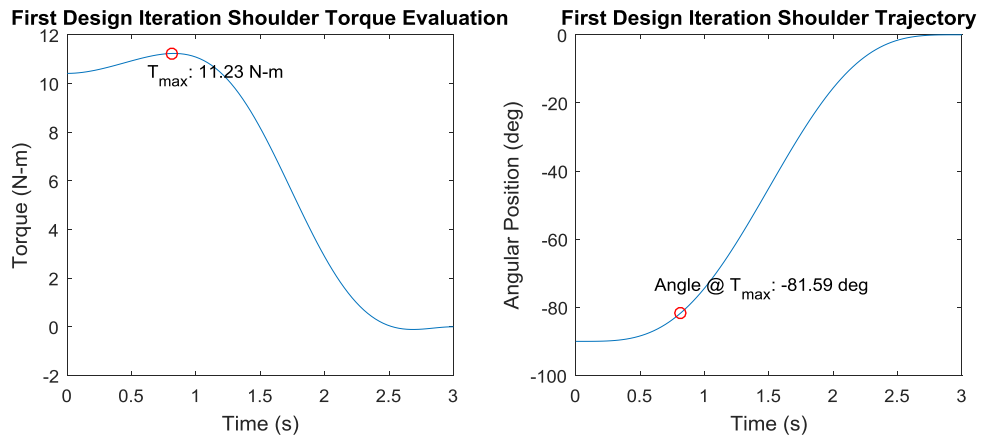


Figure 43: Shoulder Torque from Horizontal to Reference Configuration.

The maximum torque for each of the other joints can be found in Table 9 on the next page along with the respective maximum torque capability of the motor and gearbox

combination. Torque profile and trajectory plots for the other three joints can be found in Appendix B.

Joint:	Shoulder	Elbow	Wrist
Max Torque Encountered:	11.23 N-m	3.37 N-m	0.21 N-m
Motor Max Efficiency Torque	6.65 N-m	2.66 N-m	--
Motor Stall Torque	44.5 N-m	13.3 N-m	1.55 N-m
Continuous Rated Gearbox Torque	24 N-m	24 N-m	--
Percent of Limiting Torque:	47%	25.3%	13.5%

Table 9: Preliminary Torque Analysis Results.

This analysis suggests that each motor is capable of handling the loading that its respective joint will experience with a sufficient factor of safety against unknown disturbance torques.

With an estimation of the torques obtained, stress analysis of individual components can be conducted. The largest loads are found in the shoulder and elbow joints, and because the mechanical designs of these two joints are identical, the highest stresses will be found in the shoulder joint. More specifically, the highest stress can be found in the keyway of the shoulder axle, where torque is transmitted from the motor shaft to the axle via a small key insert. In this region, sharp corners and small spaces result in large stress concentrations, and an evaluation by finite-element-analysis (FEA) is

necessary. In order to evaluate the stress response of the shoulder axle with a degree of confidence, the component is loaded with the continuous rated torque of the shoulder gearbox, over twice the maximum expected loading of the joint. To simulate the loading, a distributed force of 3500 N is applied in the keyway at the contact interface between the axle and the motor key. This loading, applied at an average distance of 7 millimeters from the axis of the cylinder, produces a torque of 24.5 N-m about the joint axis, similar to what would be expected from the motor exerting the rated torque of the gearbox. The mesh of the FEA simulation is defined as very fine in this region to ensure a mesh-independent solution. A visual representation of the loading can be seen in Fig. 44 below.

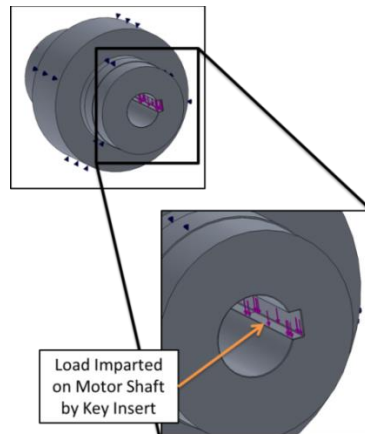


Figure 44: Shoulder Axle FEA Loading.

The axle is constrained with simulated bearing supports (which permit rotational deflection) and fixed at the inner surfaces of the mounting holes where the adapter plate is fastened, as shown in Fig. 45.

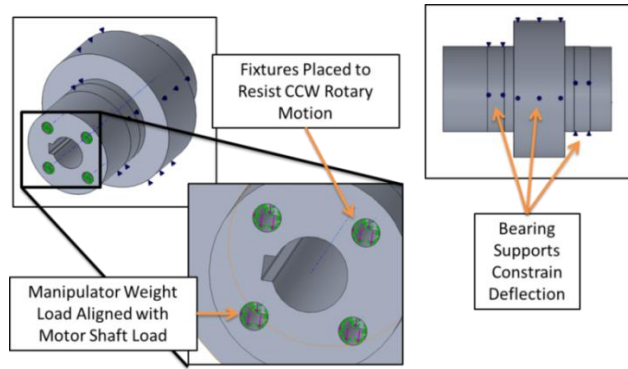


Figure 45: Shoulder Axle FEA Supports and Fixtures.

The fixtures are defined such that they resist the rotational motion tendency caused by the loading. In addition to the contact force of the motor on the axle, a distributed load of 40 N is placed on the inner surface of the fastening holes to simulate the shear force produced by the weight of the manipulator. This type of loading is reflective of a situation in which the manipulator is held in the reference configuration (perhaps by an obstacle), and the shoulder motor is attempting rotation with a torque similar to the rated torque of its gearbox. The results of this FEA simulation are shown in Fig. 46.

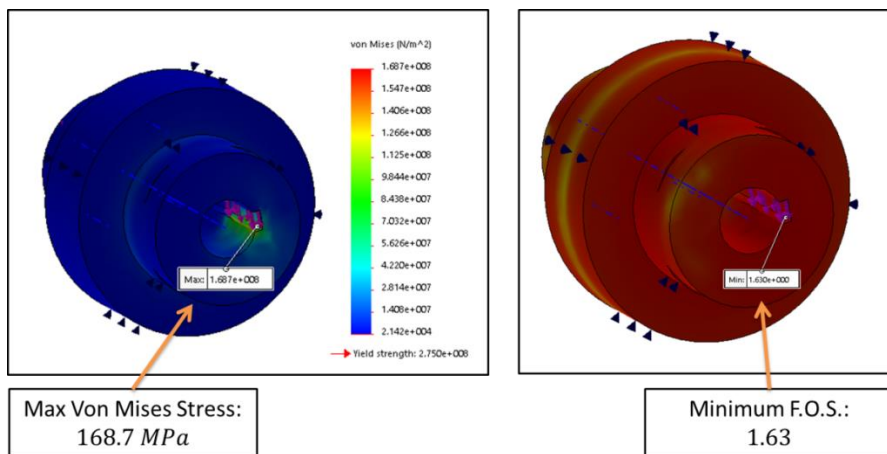


Figure 46: FEA Simulation Results.

The results presented here indicate that the shoulder axle can tolerate loading on the order of twice that which is expected with a factor of safety. From this point, it is concluded that the selected motors and structural design are sufficient for achieving design goals and requirements, and a prototype is constructed.

5-3: Prototype Construction and Model Validation

The 4 DOF manipulator prototype, post manufacturing and assembly can be seen in Fig. 47 below. The system is divided into two components, a hot-cell subsystem, and an external subsystem. Radiation sensitive integrated circuits, data acquisition units and power supplies are located outside the hot-cell. Only the manipulator structure, motors and joint position sensors are located within the hazardous environment. Communication between the two subsystems is maintained with a single wire “feedthrough.”

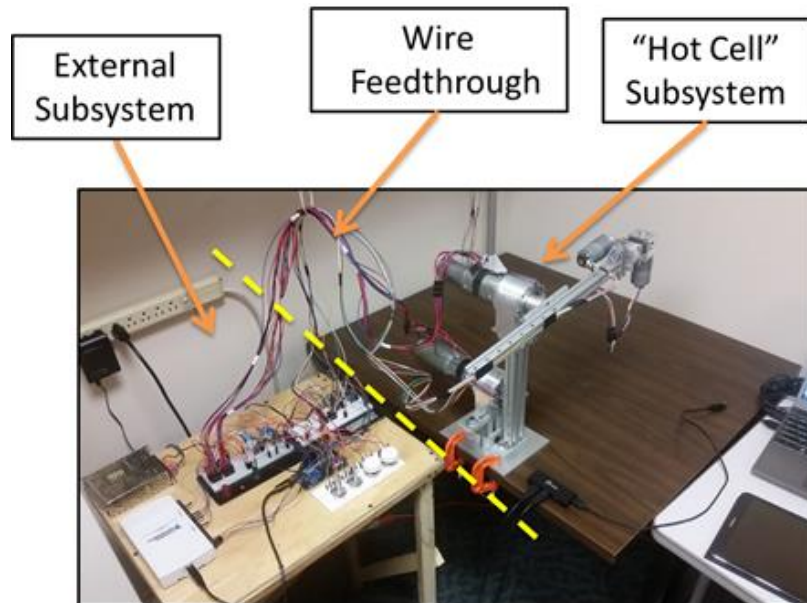


Figure 47: Robot Arm Prototype.

As described in the previous section, shoulder and elbow positions are measured with an array of Hall Effect sensors. Calibration of the sensor array is achieved with an optical encoder that is used to measure angular rotation directly. Signals from the hall array are analyzed and a relationship between them and angular position obtained from the rotary encoder is determined. A detailed description of how this calibration is obtained can be found in Appendix C.

Wrist positions are measured directly by rotary Hall Effect encoders that are integrated with the motors used on these joints. The hall sensor arrays, calibration jig and wrist position sensors are shown in Fig. 48.

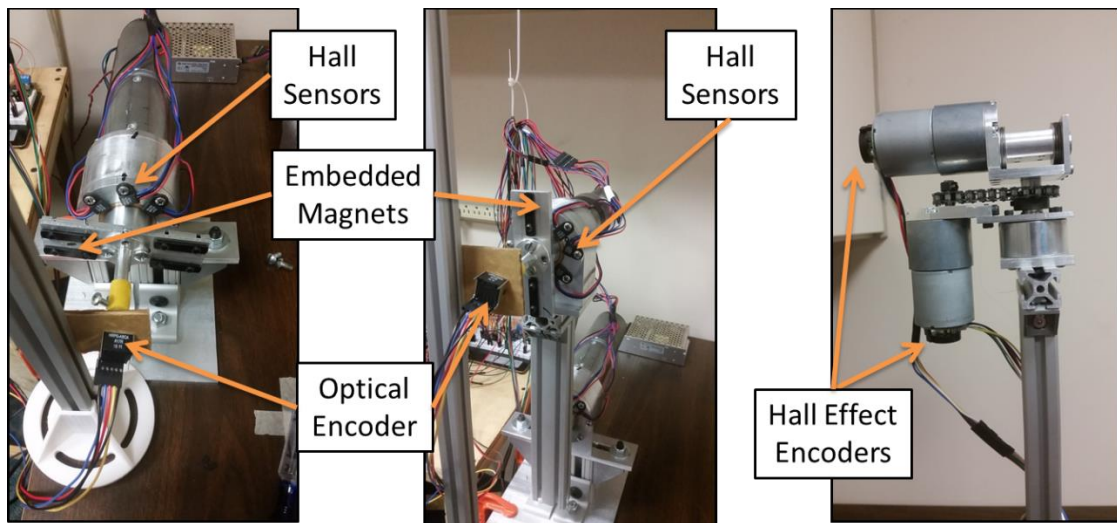


Figure 48: Position Sensor Location and Calibration.

With the prototype constructed and sensors providing reliable position feedback, model validation testing is conducted. The ultimate goal for the design is to control the manipulator such that it accomplishes a pick-and-place task. In order to achieve control over this task, an algorithm must be developed that accepts position feedback from joint

sensors and generates a “control input” that acts on the manipulator to drive it from the current state to a desired state. To avoid damage to the manipulator, this algorithm must be designed and simulated numerically before it can be integrated with the physical device. In order to ensure reliable controller design through simulation, the numerical model must be accurate with respect to the physical system. Accuracy is determined by comparing dynamic response data obtained from device testing to simulated dynamic responses obtained from the model.

At this point in the design, the equations of motion for the manipulator are available for computing the torque required for executing any set of angular transits without the presence of disturbances. The manipulator model does not yet include the dynamics of the motors (which relate applied voltage to torque output). The control input at this point is motor torque and it is assumed that full control is available over it. In other words, it is assumed that arbitrary torque profiles can be commanded of the motors. This description is useful in model validation because the motor shafts can be disconnected from the joint axles by removing key inserts and set screws, and the dynamic response of the arm to varying initial condition tests can be measured and compared to results obtained from the model via simulation of these same situations.

Simulated angular position, velocity and acceleration results are obtained by numerical integration of Eq. 5.2.10 in MATLAB™ and Simulink™. Rearranging this equation, an expression for angular acceleration is obtained and has the form:

$$\ddot{\vec{\theta}} = M^{-1}(\vec{\theta})[\vec{\tau} - C(\vec{\theta}, \dot{\vec{\theta}})\dot{\vec{\theta}} - N(\vec{\theta}, \dot{\vec{\theta}})] \quad (5.3.1)$$

Matrix terms of this equation are computed each time step by substitution of angular position and velocity from the integration.

For model validation, the physical system is configured for, and subjected to six different initial condition tests, one of which can be seen in Fig. 49 below.

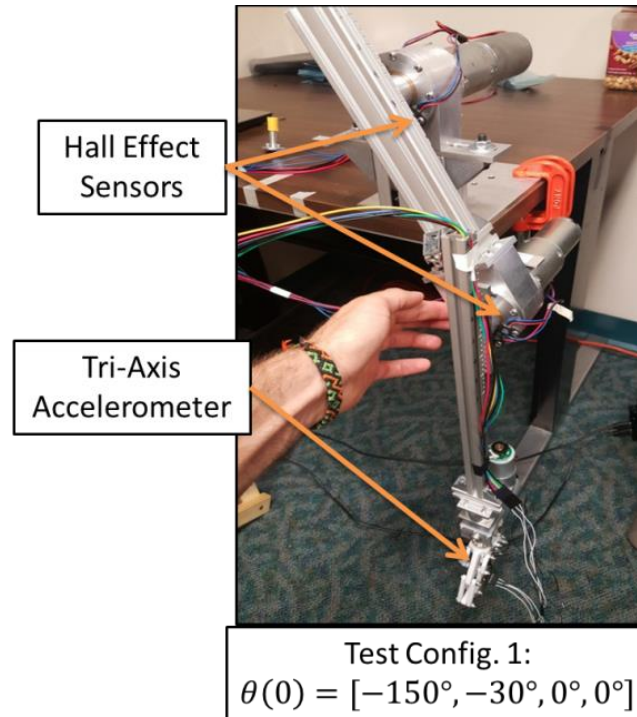


Figure 49: Model Validation Test Configuration 1.

During these test, shoulder and elbow position measurements are recorded directly. Due to the nature of the test however, *direct* wrist position measurements cannot be obtained. During regular operation these measurements would be provided by the Hall Effect encoders that are integrated with the wrist motors, however with the motor shafts disconnected, the shafts do not rotate and the sensors provide no measurement. In order

to capture the dynamics in this region, an accelerometer is mounted on the end effector at the origin of its body reference frame as shown on the next page.

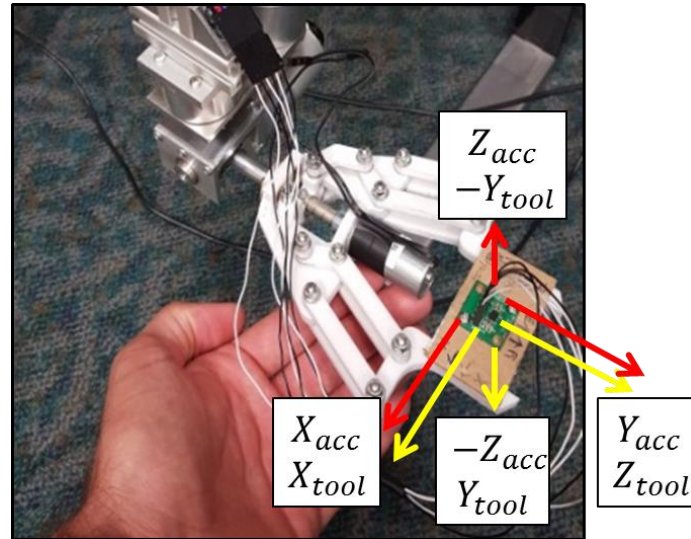


Figure 50: End Effector Acceleration Measurement.

End effector (tool) acceleration is directly related to the angular rotation of each joint in the manipulator chain. This acceleration can be obtained from simulation by simple transformation of the tool frame acceleration vector from base frame to tool frame. Tool position in the base frame is strictly a function of joint position, $\vec{\theta}$ (obtained by integration of Eq. 5.3.1) by the forward kinematic equation (Eq. 5.1.12). Tool position can be twice differentiated to obtain tool acceleration in the base frame. From here, the reverse kinematic transformation of base frame with respect to tool frame is used to express the acceleration vector in tool frame coordinates. This transformation is defined as:

$$g_{ts}(\vec{\theta}) = \begin{bmatrix} R^T & -R^T \vec{p} \\ 0 & 1 \end{bmatrix} \quad (5.3.2)$$

Thus the acceleration of the tool frame in its own coordinates is obtained by:

$$a_{t,b} = g_{ts}(\vec{\theta})a_{t,s} \quad (5.3.3)$$

The acceleration expressed in this equation is essentially what the accelerometer *should* measure. The orientation of the sensor body frame (shown with red arrows in Fig. 50) is slightly different than the end effector body frame for mounting purposes, thus an additional transformation must be performed for direct comparison of the data. From the figure, it can be seen that the X axes of the two frames are in the same direction, thus a simple rotation matrix is used to “rotate” the accelerometer data from its own body frame, to the frame of the tool. Methods of obtaining and conditioning the data from the accelerometer can be found in Appendix D.

With sensors configured to obtain measurements of the system response, model validation testing can begin. The remainder of the initial condition test configurations can be seen in Fig. 51 on the next page. These tests are meant to isolate the dynamics of various parts of the arm for detailed comparison. The device is released from rest in each of the configurations shown, and measurements of the transient response are obtained until the device reaches a steady state configuration. Experimental results are plotted with simulated results and model parameters are tuned such that the two responses match as closely as possible.

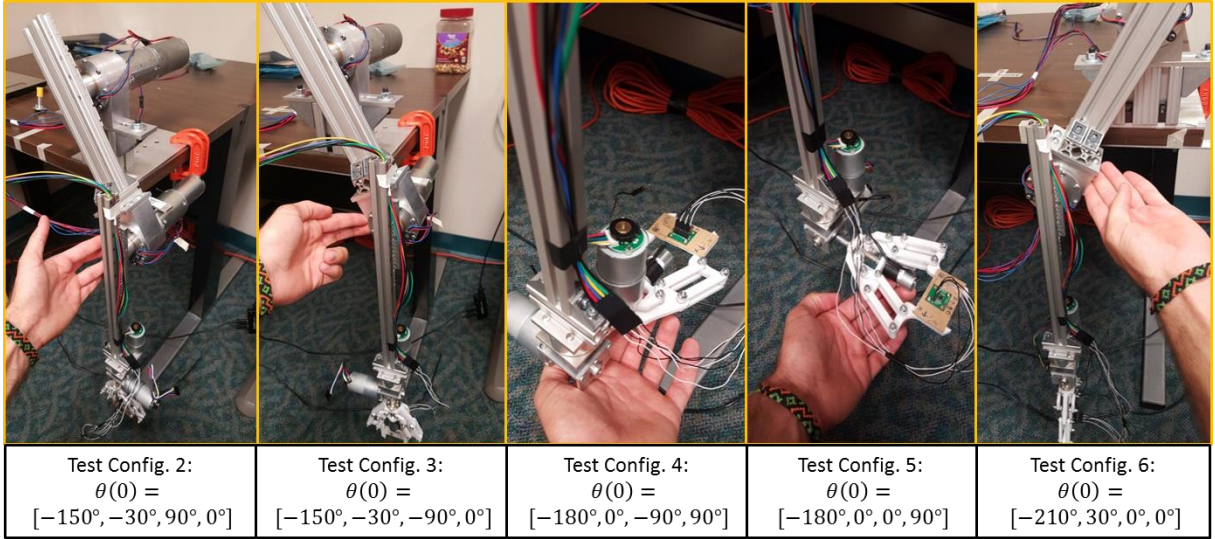


Figure 51: Other Model Validation Test Configurations.

Results obtained from the first iteration of model simulation comparison and tuning can be seen in the figure below.

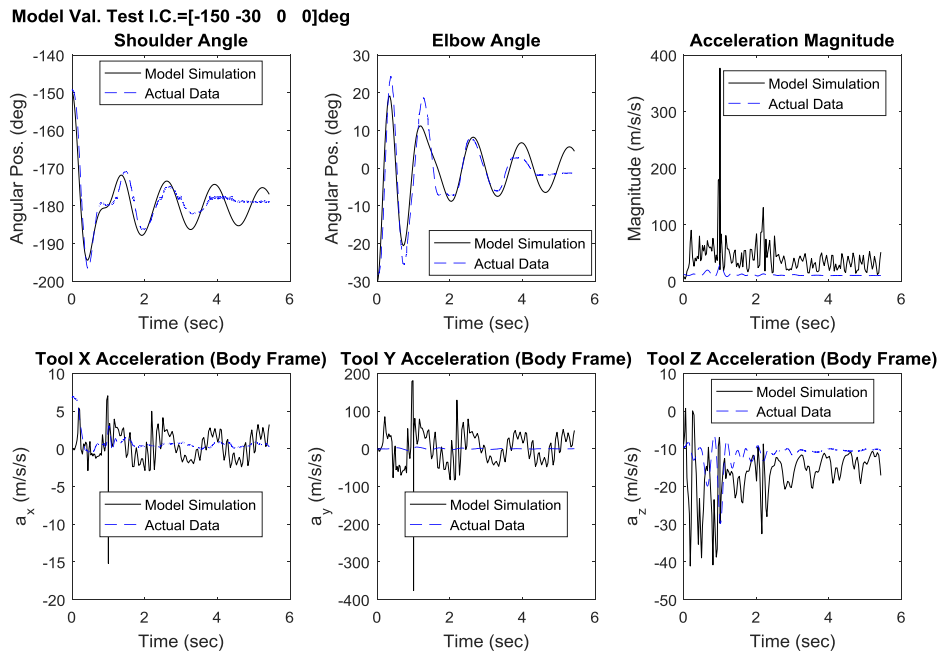


Figure 52: First Model Validation Response Comparison.

Looking at this figure it is evident that there are flaws in the model. The initial responses of the shoulder and elbow joints are similar to those predicted by simulation in terms of amplitude and frequency; however the “long term” responses differ substantially. Simulation results indicate the presence of oscillations long after the experimental data converges to steady state. In addition, simulated tool acceleration differs by orders of magnitude from data obtained from the accelerometer. Initial shoulder and elbow responses indicate that the modelling of inertia in the system is accurate but prolonged oscillations suggest there is a problem with the damping. Damping in this particular system is introduced with friction, which at this point is modelled as simple viscous friction. More damping can be added to the model by simply increasing the magnitude of the viscous friction coefficient related to each joint. However doing so causes inaccuracy in the initial response as shown in Fig. 53.

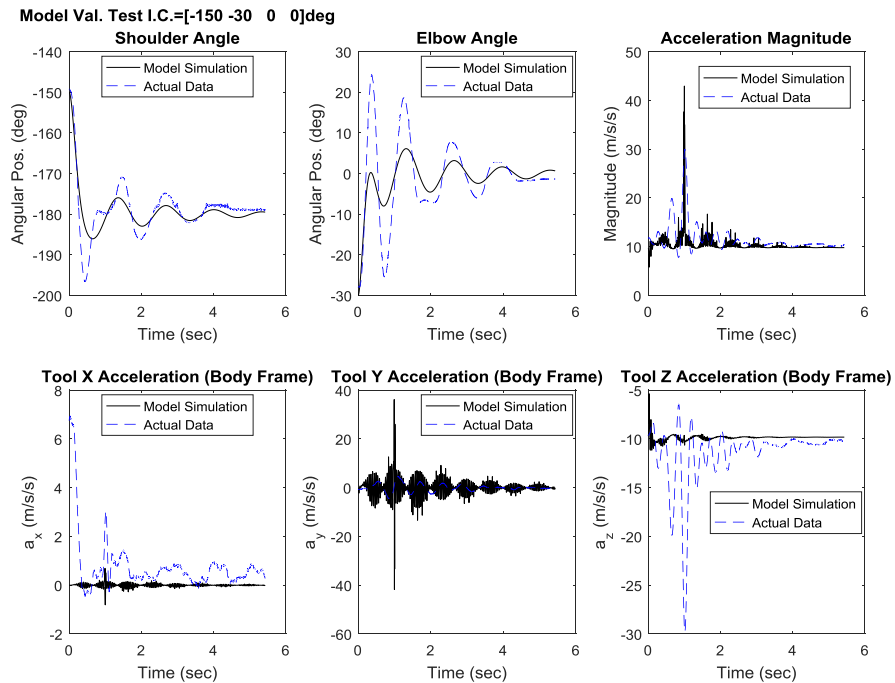


Figure 53: Model Validation Response with Added Viscous Friction.

These results suggest that at relatively large velocities, the viscous friction model of damping (with coefficients similar to those used to produce Fig. 52) is accurate, however as angular velocity nears zero, there is insufficient damping, causing sustained oscillations. What is needed is a more accurate description of friction.

A more detailed model of friction includes a *Coulomb*, or dry friction, component and a viscous friction component. The Coulomb friction coefficient is constant and is specific to the materials that are interacting. The coulomb friction force is a function of this coefficient and the normal force between contacting surfaces. Adding Coulomb friction to the model creates an offset in the friction force at zero velocity (seen in Fig. 54), thus providing a model of sticking friction in the joint as well. The friction force derived from this description will be similar to that of the purely viscous model at large angular velocities, but much greater at velocities near zero.

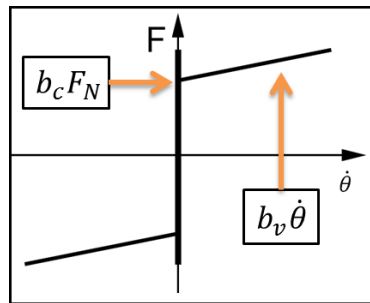


Figure 54: Model of Friction with Coulomb and Viscous Components.

One computational problem that presents itself with this description is the hard non-linearity (switching) that occurs at $\dot{\theta} = 0$. This feature results in a net friction torque at zero angular velocity (unrealistic), and can also cause high frequency oscillations in the model at small angular velocities which yield inaccurate results. In order to avoid this, a

smooth polynomial function is defined to model friction at velocities very close to zero (on the order of 10^{-3} rad/s). The boundary conditions for defining this polynomial are that it should pass through the origin and match the slope and location of the viscous friction component of the model at some angular velocity threshold, ω_{th} and $-\omega_{th}$. Because there are 5 boundary condition equations to satisfy (one for zero-crossing, and 4 for slope/point agreement), it is necessary to define a polynomial with 5 coefficients, or a 4th order polynomial, for the “Coulomb” portion of the friction model. A visual representation of this model in the vicinity of zero velocity is shown below.

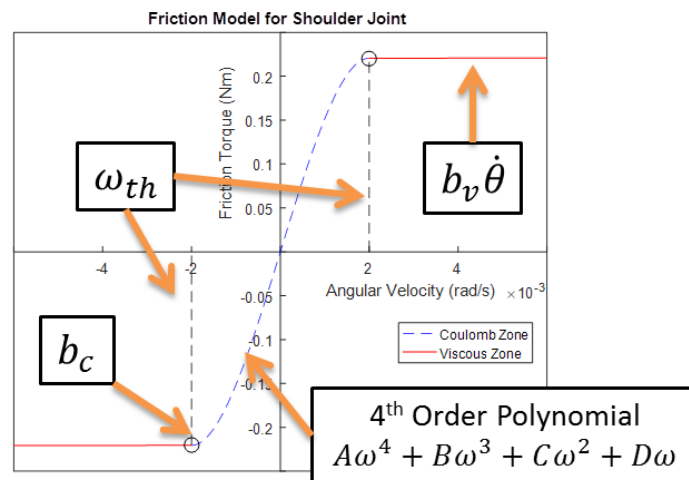


Figure 55: Critiqued Model of Coulomb and Viscous Friction.

In order to build this piecewise function, three components must be defined, angular velocity threshold, ω_{th} , viscous friction coefficient, b_v , and Coulomb friction coefficient, b_c . These are free model parameters that are tuned with iterative simulation to achieve model validation. When viewed from the scope of normal angular velocities, this friction model looks much like that presented in Fig. 54 on the previous page.

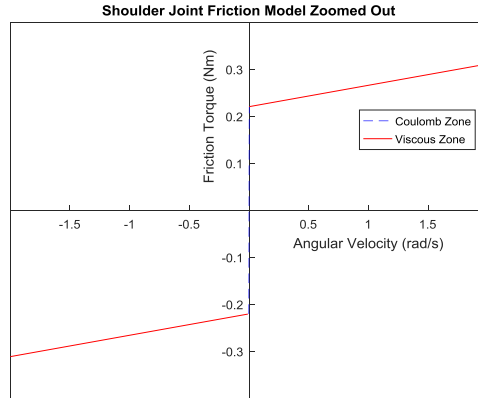


Figure 56: Expanded View of New Friction Model.

With a new friction term comes a change to the model equations of motion. This term is no longer grouped into the “ N ” matrix of Eq. 5.2.10 and Eq. 5.3.1. Instead, N is left as a description of the gravitation forces ONLY. Friction forces are computed separately and added to the other terms in the equations of motion to obtain angular acceleration as follows:

$$\ddot{\vec{\theta}} = M^{-1}(\vec{\theta})[\vec{\tau} - C(\vec{\theta}, \dot{\vec{\theta}})\dot{\vec{\theta}} - N(\vec{\theta}) - F_f(\dot{\vec{\theta}})] \quad (5.3.4)$$

The amended model is now simulated and compared once again to the response data with much more desirable results. Response comparison for *initial condition test configuration 1* can be seen in Fig. 57 on the next page, and comparisons for the rest of the model validation tests can be found in Appendix E.

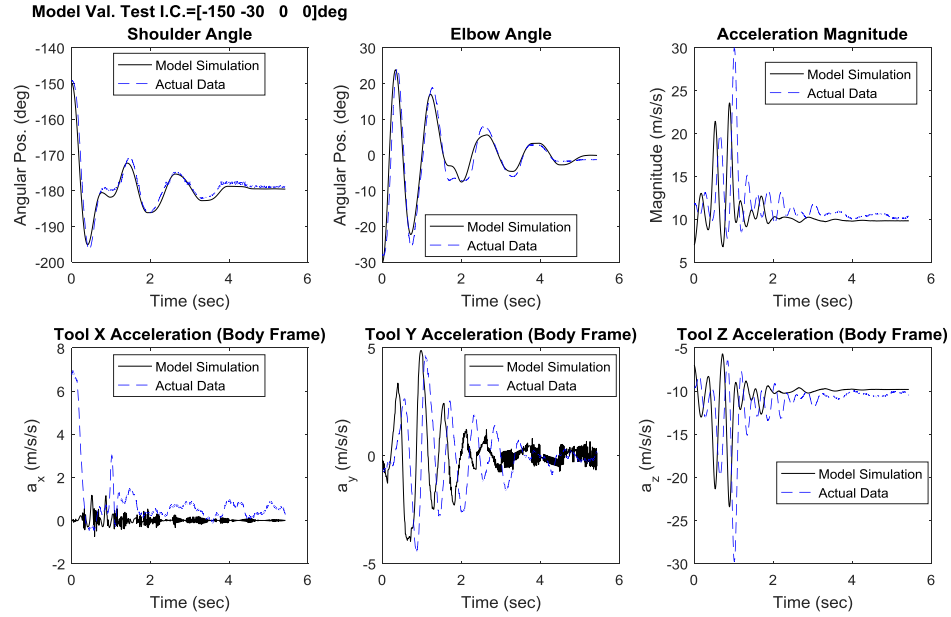


Figure 57: Model Validation Response Comparison with New Friction Model.

The root-mean-squared errors for each model validation test are shown in Table 10. The errors presented in this table are assumed to be in the tolerable range (as analysis presented in the next chapter will prove) thus model validation for the dynamics of the mechanical arm is obtained.

	Root-Mean-Squared Error (degrees,m/s/s)					
Initial Conditions	Shoulder Angle	Elbow Angle	X-Axis Acceleration	Y-Axis Acceleration	Z-Axis Acceleration	Acceleration (Magnitude)
[-150°,-30°,0°,0°]	1.832	2.723	1.444	2.117	4.03	3.843
[-150°,-30°,90°,0°]	2.202	3.851	1.475	0.257	1.3	1.278
[-150°,-30°,-90°,0°]	3.7	6.24	2.077	0.495	1.744	1.667
[-180°,0°,-90°,90°]	1.568	0.889	0.311	3.585	7.605	6.927
[-180°,0°,0°,90°]	1.915	1.371	0.745	1.617	1.937	1.81
[-210°,30°,0°,0°]	1.189	1.904	0.591	2.052	3.666	3.494

Table 10: Model Validation Root-Mean-Squared Errors.

Going forward with the design, it is assumed that expressions of arm motions and generated torques are accurate with respect to the prototype. This means that control design can be achieved with simulation of the numerical model before integration with the physical device. Before this can be achieved however, an understanding of the electro-mechanical dynamics of the motor actuators must be obtained. This is covered in the following section.

5-4: Actuator Dynamic Model and Validation

Up until this point in the design, modelling has assumed *torque* as the external input to the dynamic equations. Although this is true from a structural-dynamics perspective, direct control over the torque is not possible and thus it cannot be used as a control input for manipulating the robot. The torque applied by the motors is a function of their own dynamic properties that are described by their electrical configurations and the loads placed upon them. An understanding of these properties must be obtained so that the motors can be commanded to manipulate the robot in a way that is desired.

As an electro-mechanical system, the robot arm has a schematic representation like the one shown in Fig. 58 on the next page.

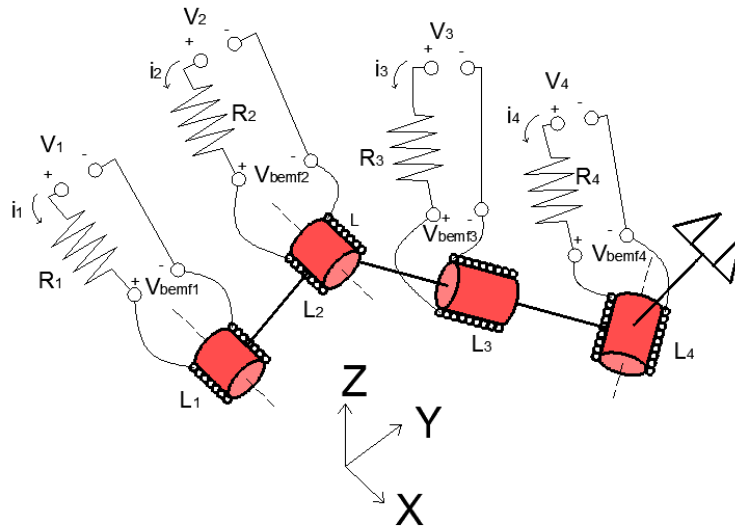


Figure 58: Electro-Mechanical Representation of the Robot Arm.

DC motor functionality is based on the “Lorentz force” that acts on a current carrying conductor in the presence of a magnetic field. A loop of wire is surrounded by permanent magnets and the application of a voltage difference across the two ends of the wire induces a current and thus a Lorentz force that tends to rotate the coil (armature). In “Brushed DC Motors,” voltage is applied to the coil through a brush that makes contact with a segmented ring (commutator) that is divided such that the direction of current flow is alternated, and the direction of the Lorentz force induces rotation in a constant direction. As the coil rotates, a potential is developed that opposes the applied voltage. This is known as *back emf*, and happens as a result of electromagnetic induction by forced rotation of a current carrying conductor in a magnetic field. Each motor is modeled as two components, an electrical system and a mechanical system. The electrical system is characterized by the current flowing through the motor, I , the resistance of the coil, brush and commutator, R , the inductance of the coil, L , the back emf, V_{bemf} , and the

applied voltage, V . The mechanical system is characterized by the torque load exerted on the motor shaft, T_L , the inertia of the motor shaft, J , friction on the motor shaft, b , and the torque generated by the Lorentz force. A schematic representation of a single motor system can be seen in Fig. 59 below.

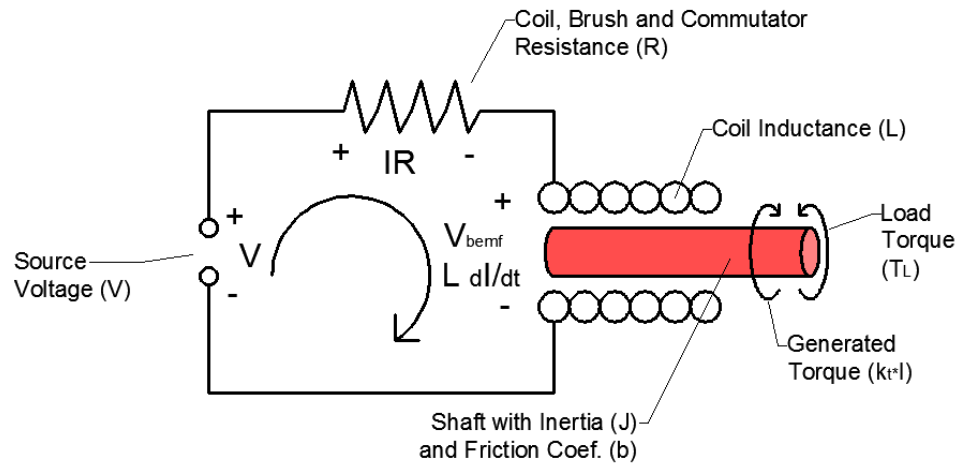


Figure 59: DC Motor Schematic Representation.

The governing equations for the motor can be developed using simple application of Kirchoff's Voltage Law and sum-of-torques about the motor shaft. Kirchoff's Law for the DC motor has the following form:

$$\sum_{loop} V = 0 \rightarrow V - IR - L\dot{i} - V_{bemf} = 0 \quad (5.4.1)$$

The back emf voltage is proportional to the angular velocity of the armature by a factor, k_v , known as the motor voltage constant, and the expression:

$$V_{bemf} = k_v \dot{\theta} \quad (5.4.2)$$

Combining these two equations and solving for the derivative of current, the governing equation for the electrical system is obtained:

$$\dot{i} = \left(\frac{1}{L}\right) [V - IR - k_v \dot{\theta}] \quad (5.4.3)$$

In similar fashion, the governing equation for the mechanical system is obtained by writing sum-of-torques about the motor shaft:

$$\sum_{shaft} \tau = J\ddot{\theta} \rightarrow k_t I - b\dot{\theta} - T_L = J\ddot{\theta} \quad (5.4.4)$$

The term, k_t , is called the motor torque constant, and the expression, $k_t I$, is the definition of the torque developed as a result of the Lorentz force. Solving for the highest derivative of position, $\ddot{\theta}$, the equation of motion for the motor shaft is obtained:

$$\ddot{\theta} = \left(\frac{1}{J}\right) [k_t I - b\dot{\theta} - T_L] \quad (5.4.5)$$

Equations 5.4.3 and 5.4.5 are linear, co-dependent, differential equations that can be formatted into state-space-representation (SSR) and solved easily using MATLAB™.

The state vectors for the motor system are defined as: $\vec{x} = [\theta, \dot{\theta}, I]^T$, $\dot{\vec{x}} = [\dot{\theta}, \ddot{\theta}, \dot{I}]^T$, $\vec{u} = [V, T_L]^T$. Using this definition, the SSR of the motor system has the form:

$$\dot{\vec{x}} = \begin{bmatrix} 1 & 0 & 0 \\ 0 & -\frac{b}{J} & \frac{k_t}{J} \\ 0 & -\frac{k_v}{L} & -\frac{R}{L} \end{bmatrix} \vec{x} + \begin{bmatrix} 0 & 0 \\ 0 & -\frac{1}{J} \\ \frac{1}{L} & 0 \end{bmatrix} \vec{u} \quad (5.4.6)$$

The inputs to the DC motor model are applied voltage and torque load, and the states are shaft angular position and velocity, and armature current. The model is simulated in MATLAB™ to evaluate the state response to varying input conditions.

The motors are provided with spec sheets that give information related to the performance of the motor. This information can be used as a basis of comparison for model validation as done with the mechanical structure of the robot arm. For the shoulder and elbow motors, a characteristic diagram is provided that gives efficiency, angular velocity, and current profiles under varying load torque conditions. These diagrams are shown in Fig. 60 and 61 respectively.

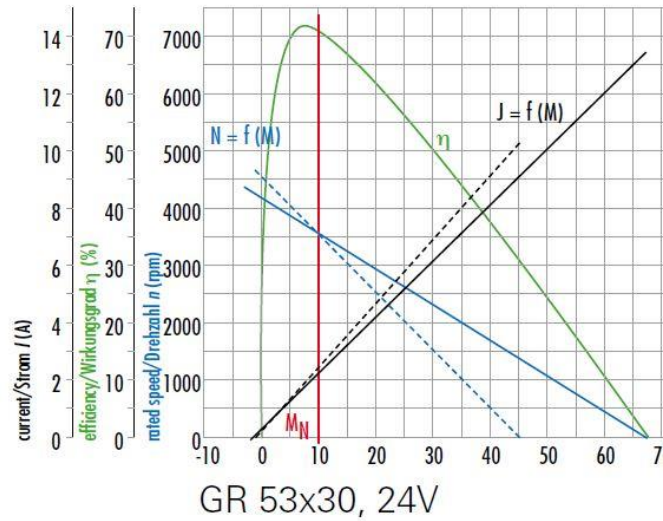


Figure 60: Characteristic Diagram of Shoulder Motor from Spec Sheet.

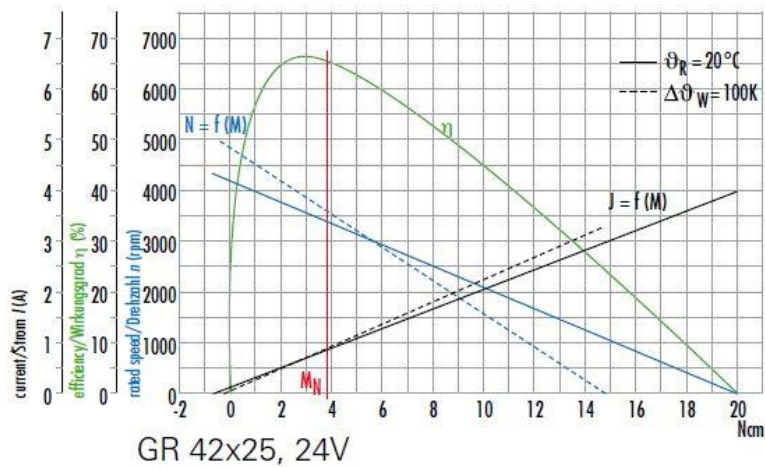


Figure 61: Characteristic Diagram of Elbow Motor from Spec Sheet.

The SSR of Eq. 5.4.6 can be used to “re-create” these spec sheets with iterative simulation. After varying model parameters to fit the simulated diagrams to the actual diagrams, an accurate model of the shoulder and elbow motors is obtained. The simulated diagrams for both motors can be seen in Fig. 62 and 63 respectively. Specifications provided by the manufacturers can be found in Appendix E.

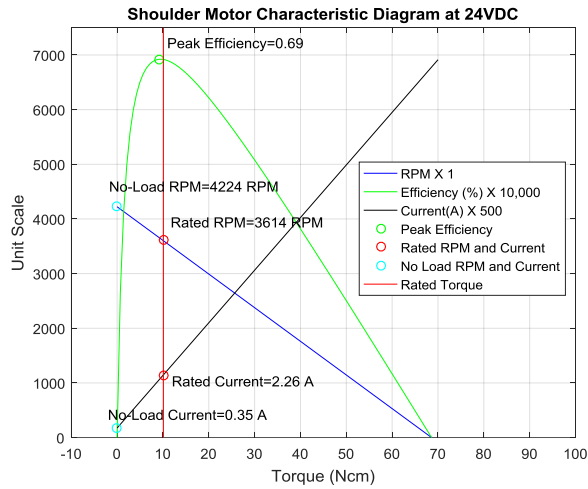


Figure 62: Simulated Characteristic Diagram of Shoulder Motor.

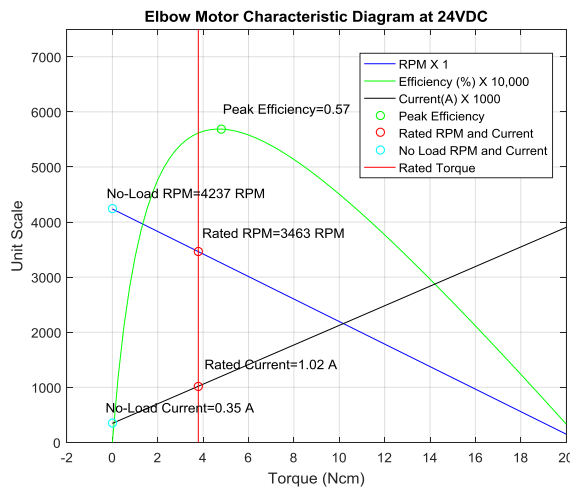


Figure 63: Simulated Characteristic Diagram of Elbow Motor.

Model validation for the wrist motors is done in similar fashion. Though a spec sheet containing current, angular velocity, and efficiency response information for these motors is not available, comparison information is available in the form of stall current, stall torque, no-load speed, and no-load current. Matching these parameters with

simulation, the characteristic diagram for the wrist motors is obtained and is shown in Fig. 64 below.

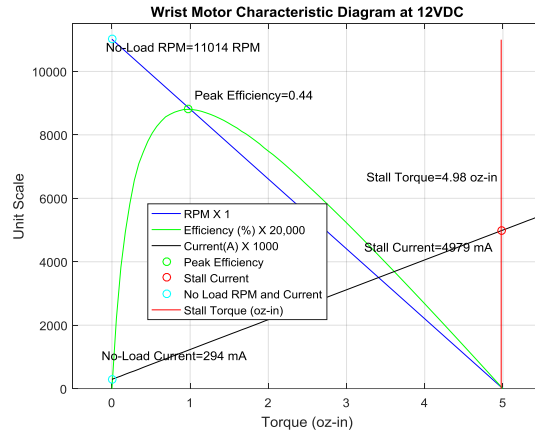


Figure 64: Simulated Diagram of Wrist Roll and Wrist Pitch Motors.

An evaluation of the errors in the actuator model validation is tabulated and shown in the following table.

Parameter	Shoulder			Elbow			Wrist		
	From Spec. Sheet	From Model	% Error	From Spec. Sheet	From Model	% Error	From Spec. Sheet	From Model	% Error
Rated Speed	3600 RPM	3614 RPM	0.30	3600 RPM	3463 RPM	3.80			
Rated Current	2.3 A	2.26 A	1.70	0.9 A	1.02 A	13.00			
Stall Current							5000 mA	4979 mA	0.42
Stall Torque							5 oz-in	4.98 oz-in	0.40
No-Load Speed	4200 RPM	4224 RPM	0.60	4200 RPM	4237 RPM	0.88	11000 RPM	11014 RPM	0.13
No-Load Current	0.28 A	0.35 A	25.00	0.17 A	0.35 A	105.80	300 mA	294 mA	2.00

Table 11: Motor Model Validation Results.

For the most part, the comparison between model and provided specifications shows desirable results. However, some of the errors presented in this table might suggest significant inaccuracies in the motor models. It will be shown later in this paper that a controller can be synthesized such that the manipulator performance is robust enough to attenuate the effects of these errors and the model uncertainties from which they are derived.

Now that the characteristic parameters of the motor models have been determined and validated, a full system dynamic model can be obtained. The DC motor model obtained for validation only includes the dynamics of the *motor shaft* in the sum-of-torques equation (Eq. 5.4.6). In order to integrate the dynamics of the robot arm presented in Section 5-2-2 with the dynamics of the motor actuators presented in this section, Eq. 5.4.5 is replaced with Eq. 5.3.4 so that the shaft dynamics for each motor are a function of the dynamics of the robot arm. The applied torques term in Eq. 5.3.4, $\vec{\tau}$, is replaced by the torque generated by the motor. In addition, new terms are introduced to express shaft angular position, velocity and acceleration ($\vec{\theta}_M, \dot{\theta}_M, \ddot{\theta}_M$) vs. joint angular position, velocity and acceleration ($\vec{\theta}_A, \dot{\theta}_A, \ddot{\theta}_A$), as well as gearbox reduction ratio (N), gearbox efficiency (gb_{eff}), and gearbox friction ($F_{fm}(\dot{\theta}_A)$). The complete model of the robot arm system has the following form:

$$\ddot{\theta}_A = \left(\frac{1}{M(\vec{\theta}_A)} \right) \left[k_t \vec{I} (N gb_{eff}) - C(\vec{\theta}_A, \dot{\theta}_A) - N(\vec{\theta}_A) - F_{fm}(\dot{\theta}_A) - F_{fj}(\dot{\theta}_A) \right] \quad (5.4.7)$$

Adding the electrical model of the motor:

$$\dot{I} = \left(\frac{1}{L}\right) [\vec{V} - \vec{I}R - k_v \dot{\theta}_M] \quad (5.4.8)$$

where the angular velocity of the motor shaft, $\dot{\theta}_M$, is related to the angular velocity of the joint by the expression:

$$\dot{\theta}_M = N\dot{\theta}_A \quad (5.4.9)$$

The additional friction term related to the motor and gearbox is modeled in the same fashion as joint friction ($F_{fj}(\dot{\theta}_A)$) and model parameters are estimated with static tilt angle threshold and step input response tests discussed in the next chapter. The moment of inertia of the motor shaft is assumed to be *very* small in comparison to the inertia of the link and is neglected in Eq. 5.4.7.

Equations 5.4.7 and 5.4.8 represent the full model of the robotic system. The only input to the system is applied voltage across each motor terminal, and the states of the system are the joint angular positions and velocities, and motor currents. With the model presented in this format, control design can commence, and an algorithm to manipulate the state of the robot by controlling voltage input can be developed.

CHAPTER 6: CONTROL AND ACCURACY/RELIABILITY STUDY

6-1: Control Design

Controlling the robotic manipulator involves knowing what input signals to give the system in each state such that it is stable and performs its task in an accurate and reliable manner. The control system must be *robust*, meaning that it must be able to keep the robot in a stable and accurate state despite unforeseen disturbance forces, position errors, and uncertainties in the dynamic model upon which it is developed. The block diagram representation of an idealized control system for the robotic manipulator is shown below.

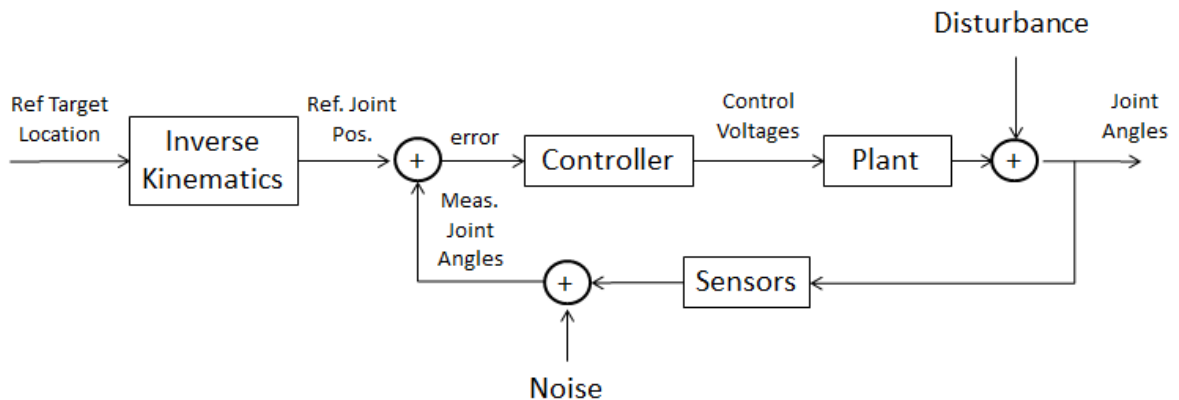


Figure 65: Block Diagram Representation of Robotic Control System.

The task presented to this robot involves locating an object, moving to the object, grasping it with its end effector tool, moving the object to a new location, and placing the object in a desired spot. In terms of a control algorithm, this process involves identifying

the position of the object in terms of its spatial orientation and coordinates in the base frame. This information is called the *reference target location* (as shown in Fig. 65) and is fed into the inverse kinematics algorithm, where the joint angles necessary for positioning and orienting the tool in this location are computed. These are called the *reference joint positions*. At this point, a control algorithm executing in real-time obtains joint position measurements from the sensors and compares them to the reference joint positions. The error margins between measured and desired position cue the controller to send voltage commands to the physical system that seek to drive it from its current (measured) state, to the desired state.

For systems that are characterized by linear differential equations, controller synthesis can be achieved with conventional methods such as PID or Pole Placement. This robotic manipulator system however is characterized by highly non-linear dynamics, thus linear control techniques cannot be fully trusted over the entire range of states. One method of obtaining effective non-linear control of a robotic manipulator would be to linearize the dynamics of the system about a series of "operating points", and schedule controller gains that are specific to configurations in the vicinity of these points to act on the manipulator as it moves. This is no small task for a robot with four D.O.F. let alone six because one operating point is defined as one set of $\vec{\theta}$, thus a very large number of operating points and gains would need to be defined to control the manipulator over its full range of motion. Another method of non-linear robotic manipulator control is the *computed torque* method [2]. This method makes direct use of the manipulator equations of motion (Eq. 5.3.4) to compute a torque trajectory profile that will theoretically drive the system from an initial state to a final state. Recall the torque profiles generated in

Section 5-2-2 to evaluate the torque loads for structural and motor capability evaluation.

Torque was computed by developing arbitrary expressions for angular position, velocity and acceleration, and using them to evaluate Eq. 5.2.10. The same principle is used in computed torque control. Once the initial and final joint positions are obtained from object location detection and inverse kinematics, desired angular trajectory functions

$(\vec{\theta}_d, \dot{\vec{\theta}}_d, \ddot{\vec{\theta}}_d)$ can be defined for each joint. These functions can be evaluated with respect to time and used to compute a torque trajectory ($\vec{\tau}_{traj}$) by the rearranged form of Eq.

5.3.4:

$$\vec{\tau}_{traj} = M(\vec{\theta}_d)\ddot{\vec{\theta}}_d + C(\vec{\theta}_d, \dot{\vec{\theta}}_d)\dot{\vec{\theta}}_d + N(\vec{\theta}_d) + F_f(\dot{\vec{\theta}}_d) = f(\vec{\theta}_d, \dot{\vec{\theta}}_d, \ddot{\vec{\theta}}_d) \quad (6.1.1)$$

The key in this control algorithm is in the definition of the joint trajectory functions. As stated in Section 5-2-2, the desired joint angular position trajectories must be twice differentiable to obtain continuous expressions for velocity and acceleration. Recalling that the workspace conditions of this robot are unobstructed and the task is path-independent, the trajectory for the control algorithm is arbitrary (as it was in the analysis presented in Section 5-2-2). With this in mind, the joint trajectories can be constructed with polynomials. These functions must accomplish two objectives: they must transition the manipulator from its initial state, to the final state as defined by the inverse kinematics. The manipulator must also start and end at rest. The latter constraint can be further defined to state that the manipulator must *stay* at rest. In other words, there must be no inertia left in the system that tends to “carry” the system away from its desired end

position. These objectives can be expressed mathematically as boundary conditions written as:

$$\ddot{\theta}_a(0) = \ddot{\theta}_a(t_f) = \dot{\theta}_a(0) = \dot{\theta}_a(t_f) = \theta_a(0) = \theta_a(t_f) = 0 \quad (6.1.2)$$

and

$$\vec{\theta}_a(0) = \vec{\theta}_0, \quad \vec{\theta}_a(t_f) = \vec{\theta}_f \quad (6.1.3)$$

The third derivate of angular position, $\ddot{\theta}_a$, is called “angular jerk.” This dynamic property must be constrained with zero-end-conditions such that the *slope* of the angular acceleration function at time-zero and final time, is equal to zero. This will ensure that the manipulator transitions smoothly out of its initial configuration, and into its final configuration, and stays there. Thus there are four functions that must be defined to govern the motion of the manipulator: angular jerk, acceleration, velocity, and position. With four equations to develop, four free parameters are needed to ensure one unique solution. Using the time-zero boundary conditions for each parameter, these four equations can be written as:

$$\begin{aligned} \ddot{\theta}_a(t) &= At^4 + Bt^3 + Ct^2 + Dt \\ \ddot{\theta}_a(t) &= \frac{At^5}{5} + \frac{Bt^4}{4} + \frac{Ct^3}{3} + \frac{Dt^2}{2} + const. \\ \dot{\theta}_a(t) &= \frac{At^6}{30} + \frac{Bt^5}{20} + \frac{Ct^4}{12} + \frac{Dt^3}{6} + const. \\ \theta_a(t) &= \frac{At^7}{210} + \frac{Bt^6}{120} + \frac{Ct^5}{60} + \frac{Dt^4}{24} + const. + \vec{\theta}_0 \end{aligned} \quad (6.1.4)$$

The expression for angular jerk must be a 4th order polynomial so that four coefficients (A , B , C , and D) are left over after application of the time-zero boundary conditions. All constants of integration cascading through these equations are either zero, or paired with coefficients of zero in order to satisfy the time-zero condition. The one exception to this is the time independent coefficient in the $\vec{\theta}_d(t)$ equation. This term is equal to initial position $\vec{\theta}_0$ to satisfy Eq. 6.1.3. In order to solve for the coefficients, A , B , C , and D , the final time (t_f) conditions are used. Applying Eq. 6.1.2 and 6.1.3 to Eq. 6.1.4 yields the following four equations with four unknowns:

$$\begin{aligned}
 0 &= At_f^3 + Bt_f^2 + Ct_f + D \\
 0 &= \frac{At_f^3}{5} + \frac{Bt_f^2}{4} + \frac{Ct_f}{3} + \frac{D}{2} \\
 0 &= \frac{At_f^3}{30} + \frac{Bt_f^2}{20} + \frac{Ct_f}{12} + \frac{D}{6} \\
 \vec{\theta}_f - \vec{\theta}_0 &= \frac{At_f^7}{210} + \frac{Bt_f^6}{120} + \frac{Ct_f^5}{60} + \frac{Dt_f^4}{24}
 \end{aligned} \tag{6.1.5}$$

Observing these equations, it is clear that joint angular acceleration, velocity and position are strictly functions of the initial and final positions, and the travel time. Thus the nominal torque trajectory used in control is simply a function of these three terms. The initial and final positions, $\vec{\theta}_0$ and $\vec{\theta}_f$ are provided by joint sensor measurements, object location and inverse kinematics, and the final time, t_f is available for manipulation. As discussed in Section 5-2-2, the shorter the travel time, the larger the dynamic loading as a result of inertial forces. Travel times of greater than 3 seconds for

angular transits of 360° were found to induce little change in the maximum torque requirements during transit. Thus travel time can be arbitrarily chosen past this threshold. For operations that require optimized travel time (such as assembly line type tasks), travel time can be iteratively adjusted in 6.1.5, to develop functions for angular motion, then the torque equation (Eq. 6.1.1) can be evaluated to analyze the maximum torque during transit. This computation can be iterated with an optimization function in the control software to solve for a travel time that yields a specific, defined torque threshold (such as half of the maximum allowable torque for a factor of safety). Samples of angular trajectory and torque trajectory computed in this fashion can be seen in Fig. 66 and Fig. 67.

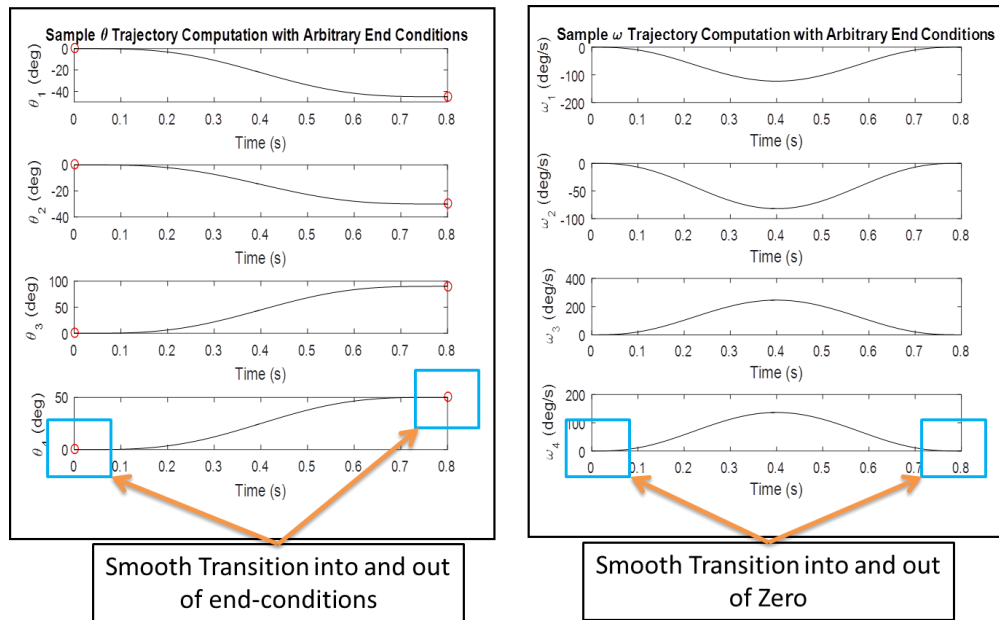


Figure 66: Angular Pos. and Vel. Trajectories for Computed Torque Control.

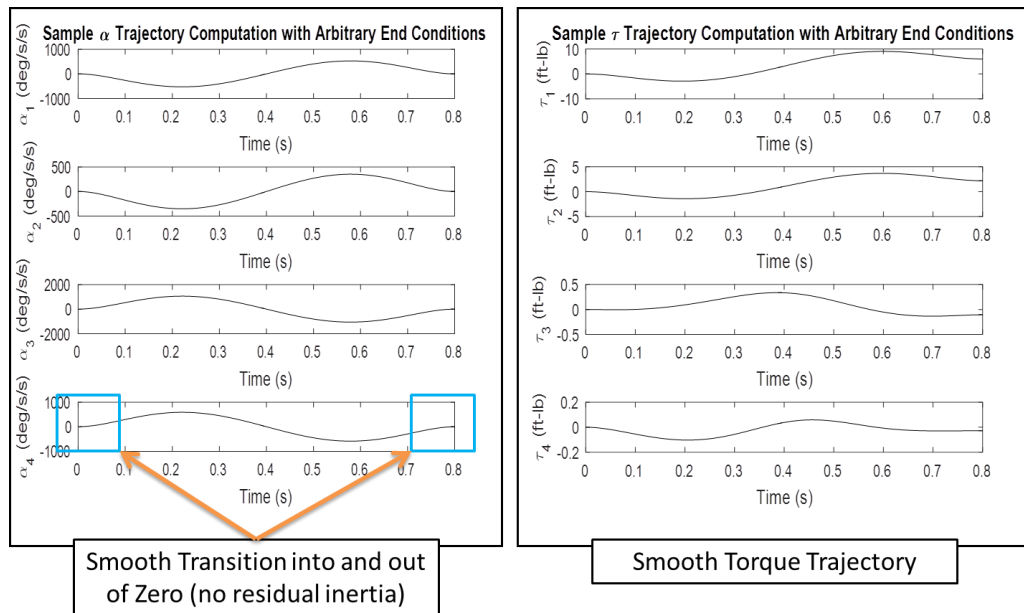


Figure 67: Angular Acc. and Torque Trajectories for Computed Torque Control.

The torque profile shown in Fig. 67 is the *nominal* torque profile that will theoretically transition the robot arm from an initial configuration to a final configuration. In an idealized situation where the robot arm device is described with 100% accuracy by the numerical model, this would be the only torque control component necessary. However, perfect models are not attainable and there will always be uncertainty involved in estimation of model parameters. In addition, uncertainties in the robot’s interaction with the environment could play havoc with a feedforward controller such as this one. The primary objective of control is that the manipulator is robust in its ability to accomplish the task in spite of model uncertainties, position measurement uncertainties, and environmental disturbances. In order to accomplish this, the controller needs a feedback term that analyzes errors between present and desired state, and adds an additional control input component to correct them. As long as these errors are kept small by the feedforward controller (i.e. the system dynamic model is “fairly” accurate), a

linear controller such as a PID can be used to act on the positioning errors. A computed torque control system with a feedback component can be seen in the diagram below.

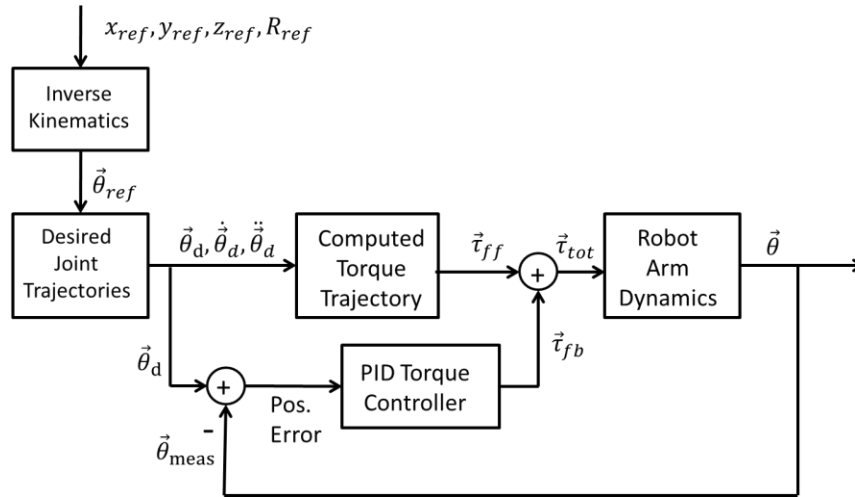


Figure 68: Computed Torque Controller with Feedback.

As discussed before, direct control over torque is not attainable in this design; however as the dynamics of the DC motors derived in the previous section show, torque is directly related to current, and in turn related to input voltage by the governing equations. Therefore the torque controller can be used to compute desired torque and this can be easily translated into a voltage command, as shown a bit later. First, it is necessary to “tune” the PID torque controller such that it and the computed torque controller have command over the dynamics of the robot arm. This is done via a simulation in which only the mechanical dynamics of the robot arm and gearbox are considered. This is done because the objective is to determine a set of PID control gains that generate correction torques capable of stabilizing the system on its desired joint trajectory. Later on it will be shown how this torque profile is used to control the DC motors.

Before the simulation can be run, several things must be considered. The first is the primary objective of the control design, robust stability and performance. In order to obtain results that offer a degree of confidence that the controller will accomplish robust performance and stability when integrated with the actual device, model parameter and disturbance uncertainty must be factored into the simulation. In order to do this, the ‘Robot Arm Dynamics’ (Fig. 68) used to simulate the system are perturbed by uncertainties while the arm dynamics that are used to calculate the nominal, feedforward torque (‘Computed Torque Profile’) are left alone. Until this point in the design, these two entities have been identical; however, a realistic control simulation can be obtained if they are slightly different. The Torque Trajectory Dynamics will be left alone because they represent the idealized model of the manipulator upon which all of the design work so far has been aimed toward developing. This concept is equivalent to the controller “thinking” that the dynamics of the robot arm are described in a certain way, when in reality, they are described *slightly* differently. If parameters in the ‘Robot Arm Dynamics’ are randomly perturbed and the control model is simulated, then the results will indicate how the controller responds to an uncertain plant. Doing so over a large number of iterations with Monte Carlo Simulation can result in testing of a wide variety of uncertainty conditions. If stability and performance is achieved over all simulations, then a degree of confidence that the controller will perform well with the actual device is obtained.

The second item to consider while designing a simulation to test the control algorithm shown in Fig. 68 is the sampling capability of the *real-time* controller. From a real world control standpoint, it is impossible to monitor the state of the system at *every*

instant in time, and it is also impossible to change the control input at every instant. Data acquisition and signal generation are constrained by the sampling rates of their internal clocks and software. The iterative process of acquiring data, extracting state measurements from the data, computing control inputs, and generating control signals is called the *servo loop*. The speed at which this process can be iterated is called the *servo rate*. In order to obtain an accurate simulation, the dynamics that describe the motion of the robot arm must be solved in continuous time, but all state feedback and control input must be held to the servo rate. Block diagram code to enact this principle can be seen outlined in blue on the computed torque simulation block diagram on the next page. Position measurement uncertainty and noise, as well as environmental disturbance torques are also included in the simulation and can be seen outlined in red.

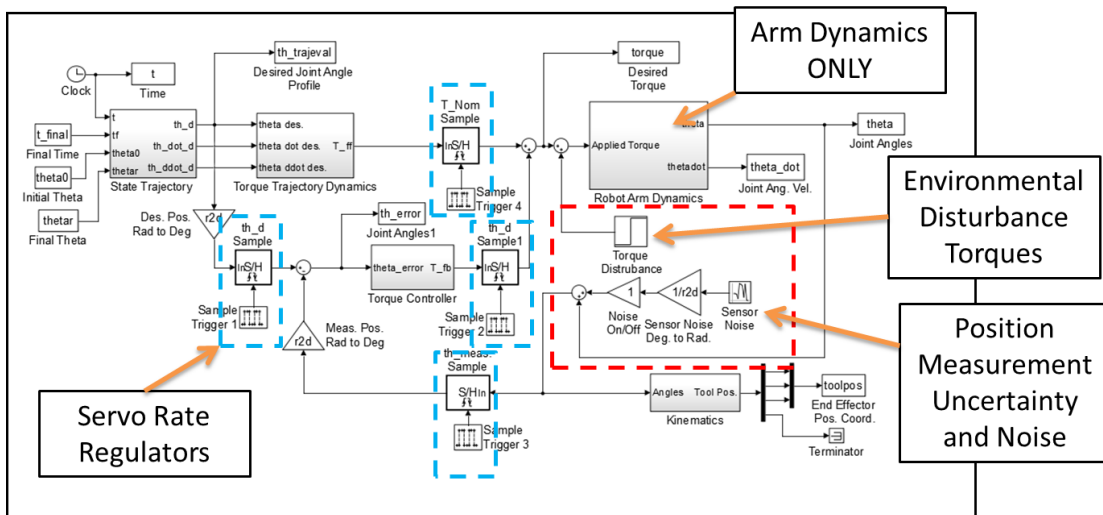


Figure 69: Computed Torque Control Simulation Block Diagram.

The PID torque controller shown in this block diagram is tuned using a simulation defined by an angular transit from the Reference Zero Configuration, to a configuration

that simulates the robot arm reaching for an object near the extent of its work envelop. In mathematical notation: $\vec{\theta}_0 = \vec{\theta}_{zero}$ and $\vec{\theta}_{ref} = [-70^\circ, -50^\circ, 70^\circ, 30^\circ]$. Using an iterative Monte Carlo type simulation approach that includes uncertainty in the robot arm dynamics, the system is simulated and the joint trajectory tracking is analyzed. Figures 70 and 71 show the joint position response and torque control input of the robot respectively for 10 iterations of simulation. From these figures it is evident that the torque controller is doing a satisfactory job of stabilizing the system on its nominal path without exceeding torque limitations of the design. A servo rate of 20Hz is used for this simulation to approximate that of the experimental set-up used for device testing that will be shown later.

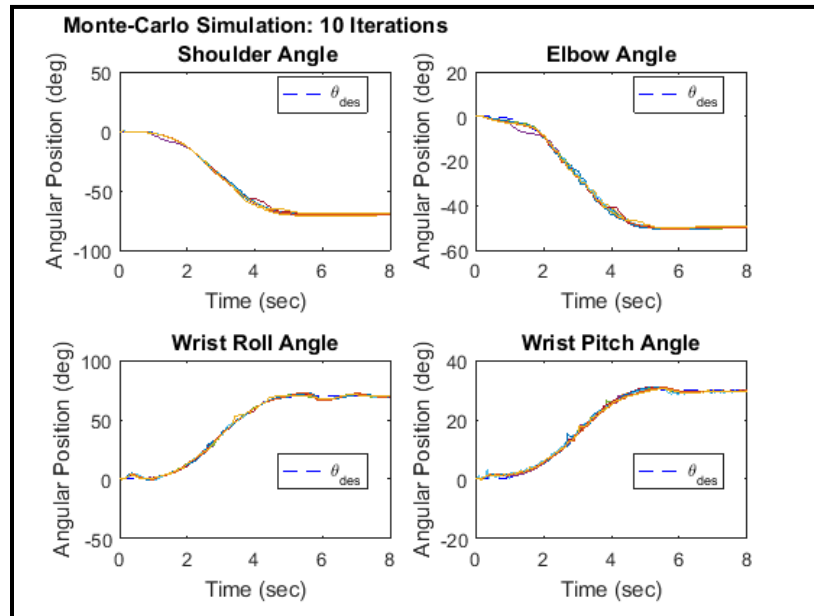


Figure 70: Computed Torque Control Joint Position Tracking Results: 10 Iterations.

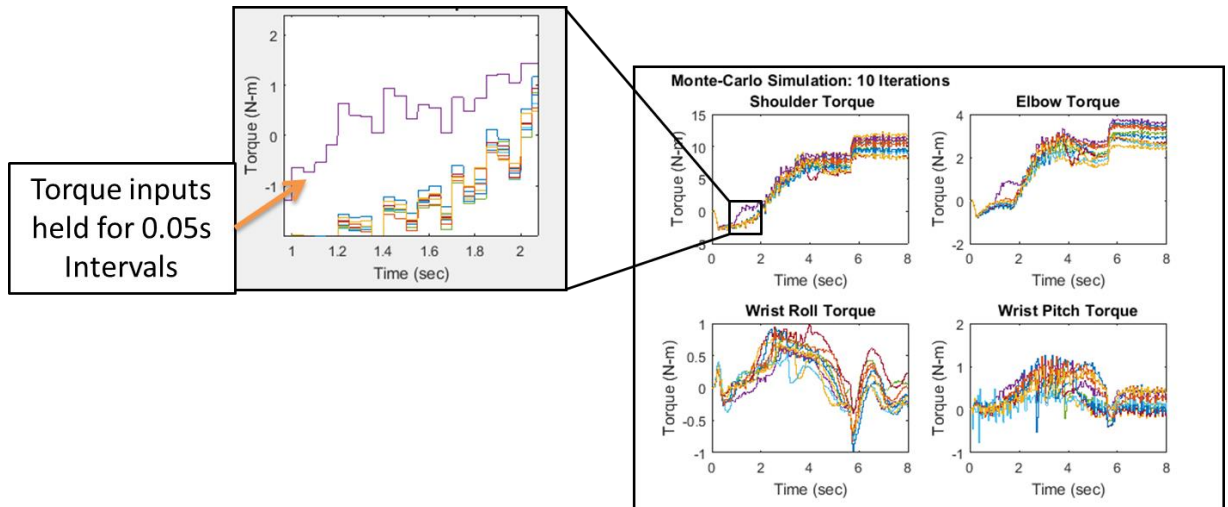


Figure 71: Computed Torque Control Input Results: 10 Iterations.

Although 10 iterations do not provide enough confidence to say the control system has *robust stability and performance*, it suggests that the PID gains of the Torque Controller are in the right neighborhood and the control design can now include the motor dynamics.

As discussed earlier, DC motor control is achieved by varying the voltage across motor terminals. The voltage input along with the torque load upon the shaft, determines the dynamic response of the motor states: position, velocity, and current. A controller that converts angular position errors into voltage commands could indeed be added to the simulation shown in Fig. 69 along with the dynamics of the motors as a means of voltage control. This method would not be robust to implement with the motor drivers that are used in the prototype however, due to lack of assurance that the generated voltages are indeed what they should be. In order to monitor the state of the motors during control, there needs to be feedback. The computed torque controller provides an estimate of the *necessary torque* required to stabilize the system on its nominal path, and the torque

generated by the DC motor is directly proportional to the current in the motor coil.

Therefore the torque command can be converted into a reference current by the following equation from the motor dynamics presented in Section 5-4:

$$\tau = k_t I * N g b_{eff} \rightarrow I_{ref} = \frac{(\tau_{ff} + \tau_{fb})}{k_t N g b_{eff}} \quad (6.1.6)$$

This reference current, I_{ref} , can be compared to a feedback current obtained from the motor driver circuit, and fed into a PID *current regulator* that converts it into a voltage command sent to the system. This method utilizes direct state feedback from the motors and provides a greater degree of confidence that control voltages are behaving as desired than a voltage controller that just uses angular position errors obtained from joint position sensors. A conceptual diagram of the robot arm and motor dynamics with a computed torque controller and current regulator can be seen in the figure on the next page.

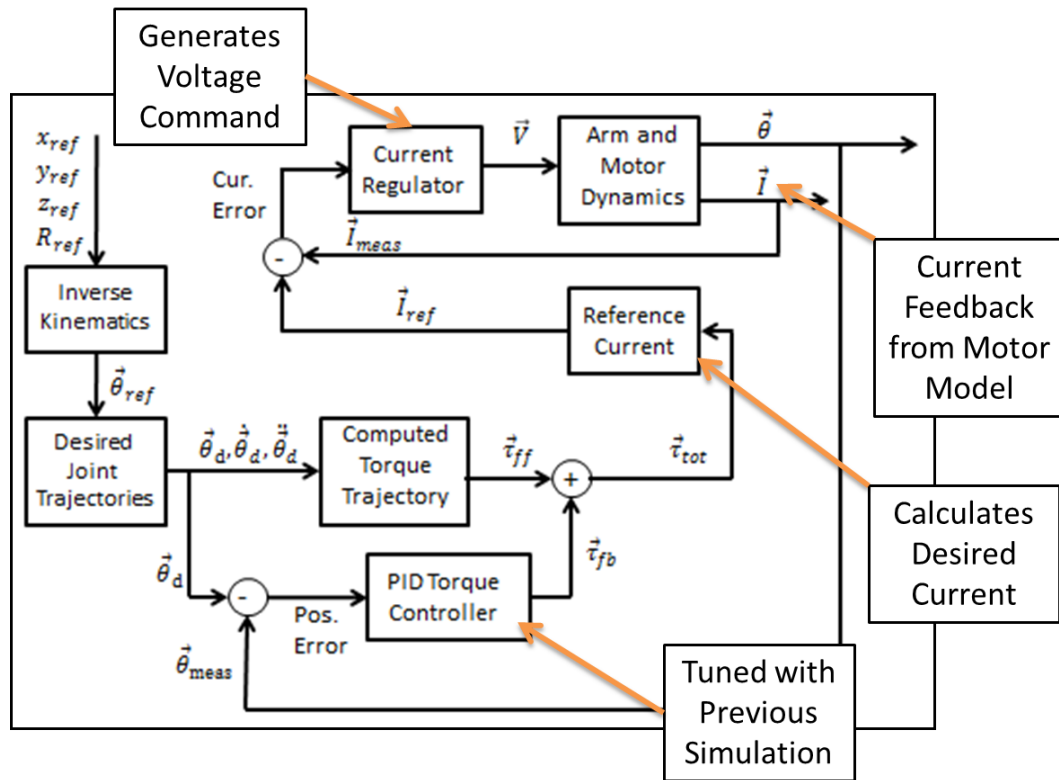


Figure 72: Robot Arm and Motor Control Diagram with Computed Torque Controller and Current Regulator.

The block diagram of this system used for simulation can be seen in Fig. 73 on the next page. With the addition of another controller and feedback term to the servo loop, two more rate regulator blocks (outlined in blue) are added to the code. The dynamics contained in the *plant* of this system represent the full dynamic model of the robot arm and its motor actuators.

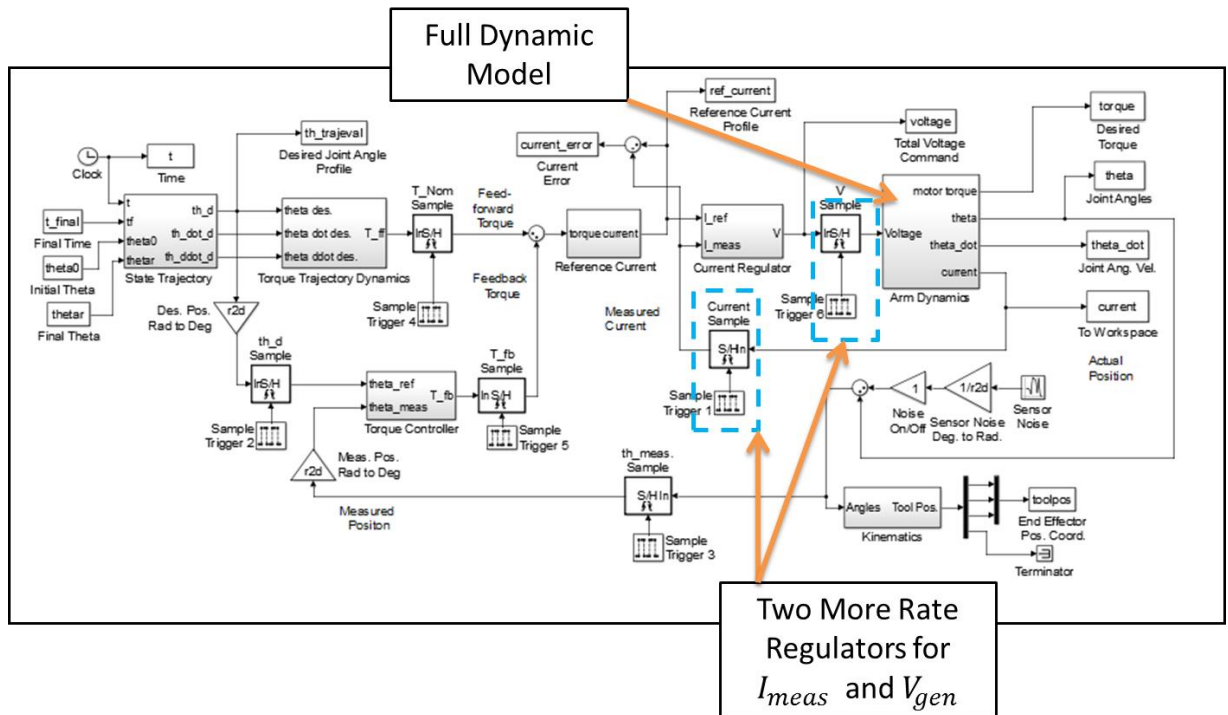


Figure 73: Block Diagram of Robot Arm and Motor Control Simulation with Current Regulator.

To begin tailoring this system for robust performance and stability, the gains of the PID torque controller are initialized to those that produced the responses of Fig. 70 and 71. The gains will not stay at these *nominal* values because the addition of a new controller brings a new input to the system that affects dynamic response, but they are a good place to start. Using the same transit that was used in the previous simulation, the gains of the PID torque controller and voltage regulator are tuned such that the simulation achieves performance and stability. As an added analysis component, simulations in which the arm returns to its Reference Zero Configuration from the reached position are conducted. Joint trajectory tracking results for these two simulations can be seen in Fig. 74a and 74b on the next page. Simulation results for voltage, current and joint torque can be found in Appendix F.

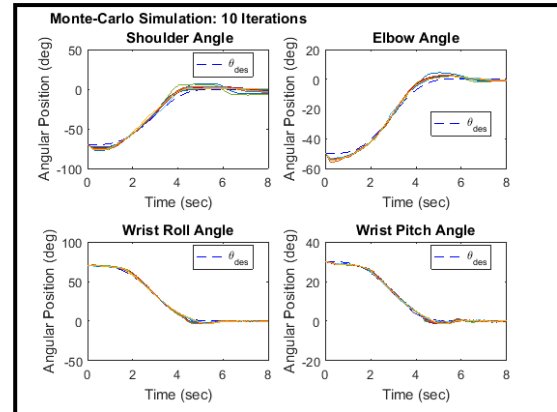
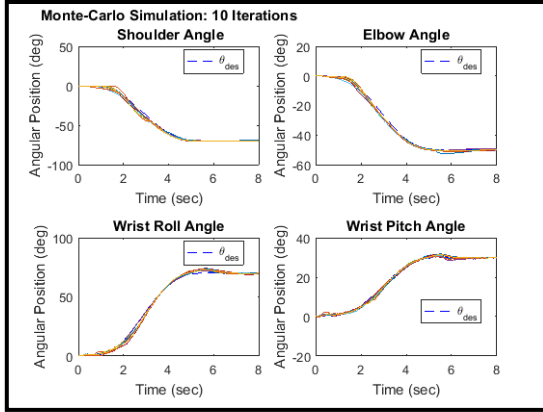


Figure 74a: Joint Trajectory Tracking for $\vec{\theta}_0 = [0^\circ, 0^\circ, 0^\circ, 0^\circ], \vec{\theta}_f = [-70^\circ, -50^\circ, 70^\circ, 30^\circ]$. **Figure 74b: Joint Trajectory Tracking for** $\vec{\theta}_0 = [-70^\circ, -50^\circ, 70^\circ, 30^\circ], \vec{\theta}_f = [0^\circ, 0^\circ, 0^\circ, 0^\circ]$.

The controller simulation results presented here are still not enough to confidently suggest robust stability and performance. In the next section, more extensive Monte Carlo simulation results will show that stability and performance are obtained over a large number of iterations. The analysis in this section suggests that the system is theoretically controllable with the array of instruments, hardware, and software that are available. The rest of the design will focus on *how* well suited these tools are in terms of controlling the robot in a way that is accurate, robust, and reliable.

6-2: Accuracy and Reliability Study

As discussed in the Literature Review section of this paper, accuracy and reliability are two very important areas of concern for a hazardous environment robotic manipulator because of its isolated nature. The manipulator must be trusted to perform its task well because errors and sustained damage are difficult to fix without direct manual access to the device.

Recall that the accuracy of this robotic manipulator was defined as how closely it can locate its end effector to a desired location in space. For a “pick and place” robot, this accuracy will determine whether or not it is successful at grasping and handling an object. There are essentially two categorical sources of uncertainty that affect the accuracy of the robot: dynamic uncertainty and kinematic uncertainty. The former refers to the dynamic properties of the manipulator, including link moments of inertia, link masses, center of mass locations, location and mass of objects grasped by the robot, friction coefficients, and motor dynamic parameters (resistance, inductance, voltage and torque constants, gearbox efficiency and gearbox reduction ratio). Uncertainties in these parameters affect the dynamic response of the robot arm during transit and perturb the device off of its nominal trajectory. Effects of these uncertainties can be seen in Fig. 74 as variations in the path that robot takes from initial to final configuration. The second type of uncertainty, kinematic, includes uncertainties in the kinematic dimensions of the robot arm such as link lengths and coordinate frame reference dimensions $(x_{0 \rightarrow 1}, y_{0 \rightarrow 1}, z_{0 \rightarrow 1})$, and also in the position measurements obtained by the sensors at each joint. Dynamic uncertainty has a more benign effect on accuracy than kinematic uncertainty because errors born of this type can be compensated for by the controller during transit. If the controller is tuned properly and it is robust to model uncertainties, the final positioning error (called the steady-state error) can be very small despite large dynamic uncertainty. Kinematic uncertainties on the other hand cannot be compensated for by the controller. They are caused by small errors introduced by manufacturing and machining tolerances and assembly of structural components, and the sensitivity and resolution of sensing devices. Kinematic uncertainties result in link length and state

measurement errors that are “unseen” by the controller because in essence, the controller “thinks” that the system is in a certain state, when in fact it is in a slightly different one.

Monte Carlo iterative simulation can be used to evaluate the accuracy of the robot over many simulations and suggest a degree of robust performance and stability. In order to obtain rough estimates of dynamic and kinematic uncertainty it is helpful to look at how they affect the system. Dynamic uncertainty can essentially be made *as large as possible* such that the system maintains stability and performance. Obtaining a threshold margin of error can be very helpful in suggesting *how accurately* the dynamic parameters must be known. Large dynamic uncertainty can also shed light on how the system will perform after prolonged exposure to radiation its potential effect on the dynamics of the motors. Another key component of dynamic uncertainty that must be modelled carefully is the uncertainty associated with picking up an object of unknown size and weight. Analysis of this can shed light on the lifting capabilities of the robot arm. Picking up an object will essentially have the effect of changing the mass and inertial properties of the end effector link. A detailed description of how this uncertainty is included can be found in Appendix F.

Kinematic uncertainty on the other hand must be evaluated using knowledge of manufacturing and machining precision, and position sensing resolution. Stepping through the assembly of each mechanical subsystem of the robot, the effect of machining, manufacturing and assembly errors must be added to each kinematic parameter to obtain a total uncertainty margin for each parameter. The uncertainty calculation for the kinematic parameter $x_{0 \rightarrow 1}$ can be seen in Table 12 on the next page as an example of this process. A more detailed description of the uncertainty calculation, along with the

specific calculations for the rest of the parameters (including some of the dynamic uncertainties), can be found in Appendix F. It should be noted that the uncertainty calculations shown in Appendix F are the same ones used in the iterative control simulations of the previous section to model plant uncertainty.

Kinematic Parameter: X0					
Source of Uncertainty	Area	Type of Uncertainty	Value of Uncertainty (+ -) in inches	Uncertainty Multiplier	Total Uncertainty
Fastening Hole Pattern of 1 1/2" T-Slot Lower Brackets to Base Plate	Base Assembly	Machining	0.0010	1	0.001
Width of 1 1/2" T-Slot	Base Assembly	Manufacturing	0.0100	1/2	0.005
Crosswise Fastening of 1 1/2" T-Slot Upper Brackets to Base Adapter Plate	Base Assembly	Human	0.0100	1	0.01
Fastening Hole Pattern of Shoulder Joint Block to Base Adapter Plate	Base Assembly	Machining	0.0010	2	0.002
Width of Thrust Bearings in Shoulder Joint Housing	Shoulder Assembly	Manufacturing	0.0021	2	0.0042
Width of Shoulder Axel Bearing Surface	Shoulder Assembly	Machining	0.0020	1	0.002
Shoulder Axel Length	Shoulder Assembly	Machining	0.0050	1	0.005
Width of Shoulder Axel to Bicep Connector Plate	Bicep Assembly	Machining	0.0050	1	0.005
Width of Bicep 20mm T-Slot (Short Dimension)	Bicep Assembly	Manufacturing	0.0100	1	0.01
Lengthwise Fastening of Short Bicep 20mm T-Slot to Long T-Slot and Bicep/Elbow Conn. Plate	Bicep Assembly	Human	0.0625	1	0.0625
Fastening Hole Pattern of Bicep/Elbow Conn. Plate to Elbow Joint Block	Bicep Assembly	Machining	0.0010	2	0.002
Width of Thrust Bearings in Elbow Joint Housing	Elbow Assembly	Manufacturing	0.0021	2	0.0042
Width of Elbow Axel Bearing Surface	Elbow Assembly	Machining	0.0020	1	0.002
Length of Elbow Axel	Elbow Assembly	Machining	0.0050	1	0.005
Width of Elbow Axel to Forearm Conn. Plate	Forearm Assembly	Machining	0.0050	1	0.005
Width of Forearm 20mm T-Slot	Forearm Assembly	Manufacturing	0.0100	1/2	0.005
Cross-Wise Fastening of Short Forearm 20mm T-Slot to Long T-Slot and Lower Wrist Roll Joint Mounting Plate	Forearm Assembly	Human	0.0625	1	0.0625
Fastening Hole Pattern of Wrist/Forearm Adapter Plate to WR Cyl.	Forearm Assembly	Machining	0.0010	2	0.002
X-Axis Location and Alignment of WR Axel in WR Housing	Forearm Assembly	Machining	0.0020	1	0.002
Fastening Hole Pattern of WR Axel to Wrist Pitch Block Base	Wrist Pitch Assembly	Machining	0.0010	2	0.002
Width of Wrist Pitch Thrust Bearings	Wrist Pitch Assembly	Manufacturing	0.0021	2	0.0042
Fastening Hole Patterns for Connection of End-Eff Mount Plate to WP Axel and End-Eff	Wrist Pitch Assembly	Machining	0.0010	3	0.003
Fastening Hole Pattern of End-Eff Base and X-Axis Alignment of Solenoid Mount Hole	End Effector Assembly	Manufacturing	0.0100	1	0.01
Total Uncertainty:					0.2156

Table 12: Kinematic Uncertainty of $x_{0 \rightarrow 1}$.

With specific values of uncertainty obtained, Monte Carlo performance analysis can begin. The first Monte Carlo accuracy simulation involves the motions described in

Fig. 74a and 74b. The first simulation includes *only* dynamic uncertainties as an illustration of how their effects differ from the effects of kinematic uncertainty. Specific details related to the amount of uncertainty in this simulation (and successive simulations) are presented in Appendix F. Accuracy results for the first analysis study containing data from 1000 iterations can be seen in Fig. 75 below. Accuracy is expressed as an absolute *distance* from the final, steady-state position of the end effector reference coordinate frame (calculated using the forward kinematic transformation) to the desired reference position of the end effector.

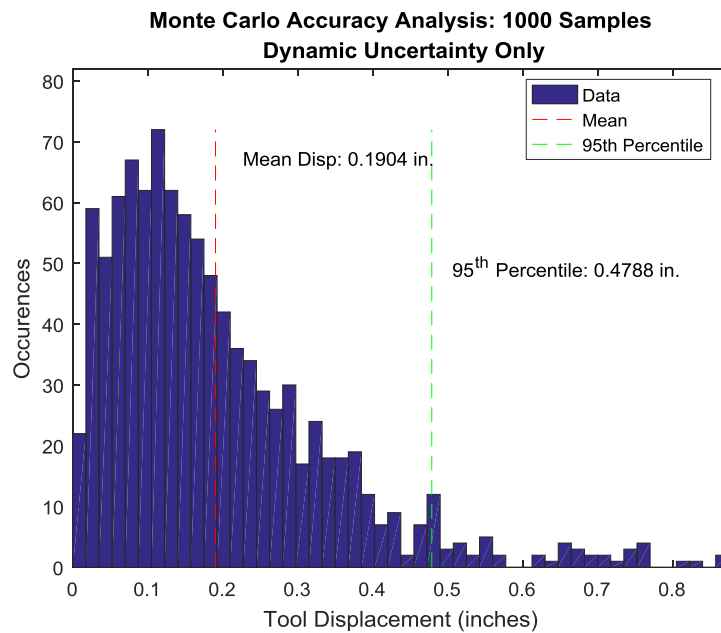


Figure 75: Monte Carlo Accuracy Analysis $\vec{\theta}_0 = [0^\circ, 0^\circ, 0^\circ, 0^\circ]$ to $\vec{\theta}_f = [-70^\circ, -50^\circ, 70^\circ, 30^\circ]$ Dynamic Uncertainty Only.

The results of the same transit, including kinematic uncertainty, are shown on the next page.

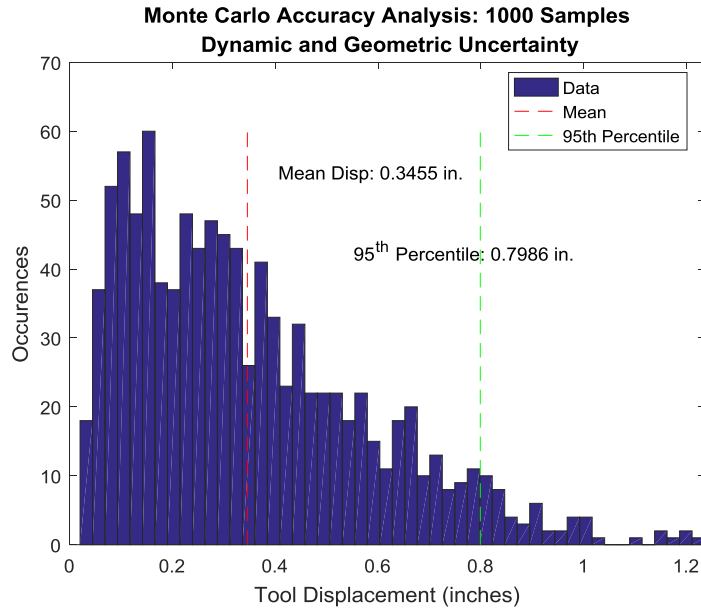


Figure 76: Monte Carlo Accuracy Analysis $\vec{\theta}_0 = [0^\circ, 0^\circ, 0^\circ, 0^\circ]$ to $\vec{\theta}_f = [-70^\circ, -50^\circ, 70^\circ, 30^\circ]$ Dynamic and Kinematic Uncertainty.

The effects of kinematic uncertainty are evident in comparison of these two simulations, as the mean tool position error nearly doubles after it is added. What this suggests is that the primary limiting factor in obtaining very high degrees of accuracy with the robot are machining and manufacturing precisions and position sensing. It makes intuitive sense that in order to know where the position of the end effector is with a high degree of precision, the lengths of all of the arm links and the positions of each joint must also be known with a high degree of precision. The results for the return trip back to the Reference Zero Configuration are shown on the next page and suggest some interesting results.

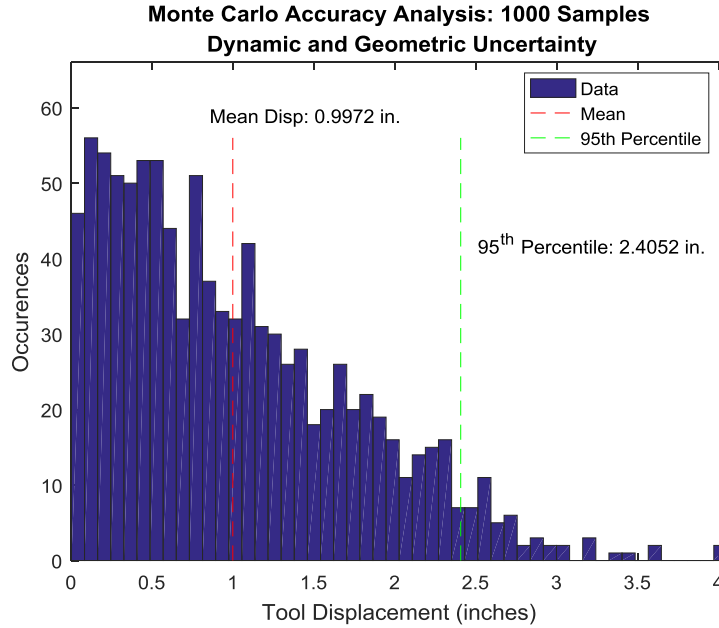


Figure 77: Monte Carlo Accuracy Analysis $\vec{\theta}_0 = [-70^\circ, -50^\circ, 70^\circ, 30^\circ]$ to $\vec{\theta}_f = [0^\circ, 0^\circ, 0^\circ, 0^\circ]$ Dynamic and Kinematic Uncertainty.

The mean tool displacement results from this simulation are nearly three times greater than those observed with the transition from the reference configuration to an extended configuration. The reason for this lies in the nature of the Zero Configuration; in this position, the torque loads on each joint are at a minimum, thus small angular position errors that trigger responses from the controller have large effects on the dynamics of the system. What is observed here is a “quasi-equilibrium” state in which the position of each joint oscillates over a small range of angles. This is undesirable from an accuracy standpoint and can potentially lead to growing oscillations and instability. For this reason a new “Home Configuration” is defined where the manipulator will reside when it is not reaching for, or placing an object. This principle was suggested earlier in Section 4-1, Fig. 13. The Home Configuration is potentially the state in which the robot will remain while it is being “transported” by a theoretical base. Thus it must be compact

such that the robot maintains a small profile, and it must be stable. Let the Home Configuration be defined as shown in the figure below.

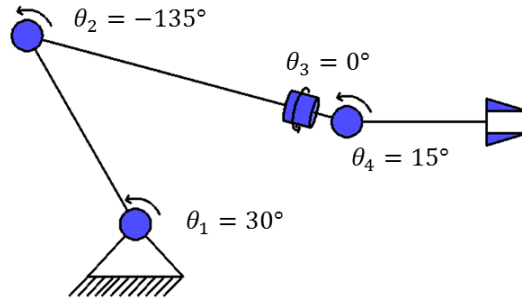


Figure 78: Manipulator in Home Configuration.

Results of a new accuracy analysis simulation in which the robot transitions from the “reached” position to the Home Configuration can be seen in Fig. 79 below.

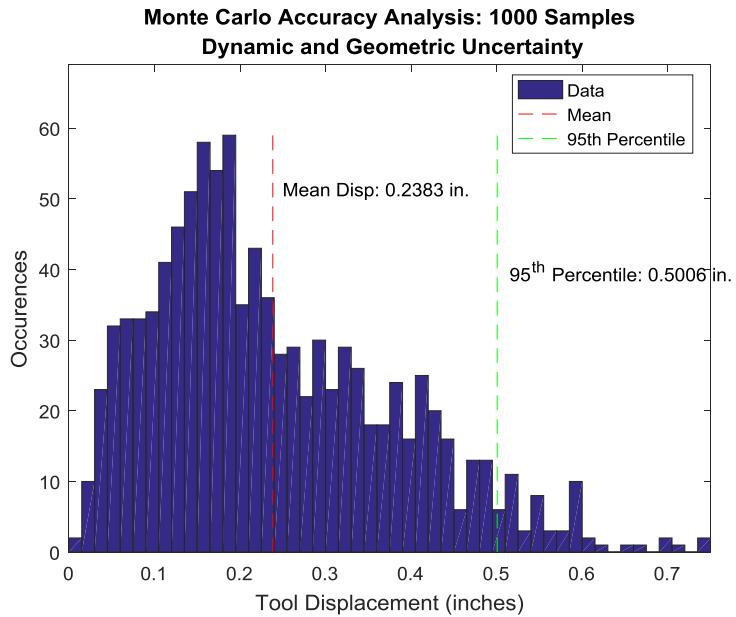


Figure 79: Accuracy Analysis for $\vec{\theta}_0 = [-70^\circ, -50^\circ, 70^\circ, 30^\circ]$ to Home Config.

The results of this simulation suggest that the Home Configuration shown in Fig. 77 is very stable (mean tool position steady state error is small), and definitely an improvement over transitioning the robot back to the Zero Configuration after it has grasped an object.

Overall, the accuracy analysis results presented in this section indicate satisfactory performance for the robotic manipulator. A visual representation consisting of the probabilistic error regions as they compare to the size of the end effector can be seen in the figure below.

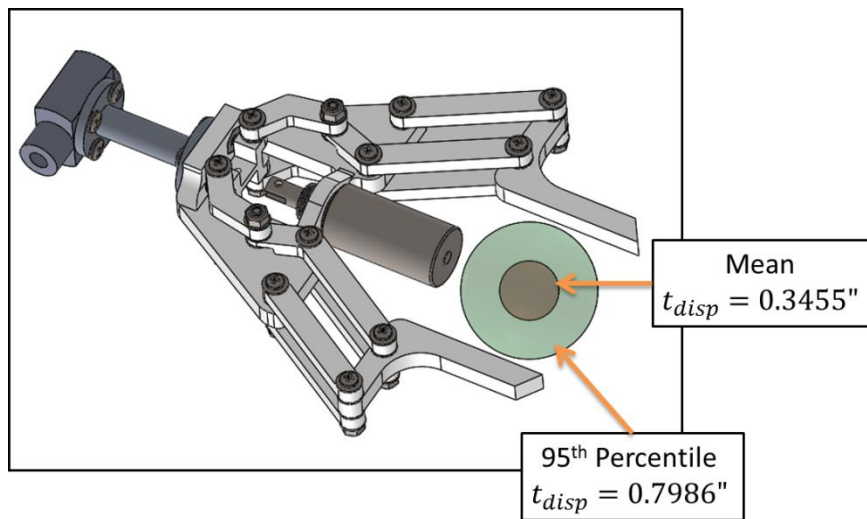


Figure 80: Probabilistic End Effector Position Relative to a Target Location.

Even cases that lie just within the 95th percentile of the accuracy range are still within the grasping capability of this end effector design. There are a multitude of ways in which object handling capability can be added to the end effector such that, once it is in this position (i.e. in the “neighborhood” of an object), fine tuning adjustments can be made such the object is grasped in a secure and reliable fashion. This would require the addition of extra sensors and actuators however, and is outside the scope of this paper.

For purpose of this design and task definition it is determined that robot is sufficiently accurate.

Accuracy evaluation is not the only valuable information that can be observed from the Monte Carlo simulations. The maximum voltage, current, and torque requirement of each motor can be extracted from each simulation, thus providing a wealth of data to suggest whether or not the limits of the actuator capabilities will ever be exceeded during operation. The specific results of this analysis for the simulation used in Fig. 76 can be seen in the following figures. The results for rest of the simulations can be found in Appendix F.

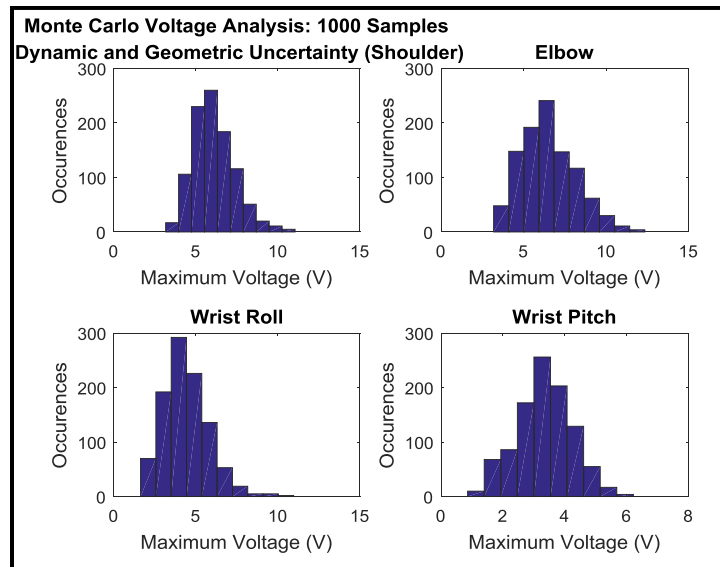


Figure 81: Monte Carlo Analysis: Maximum Voltage.

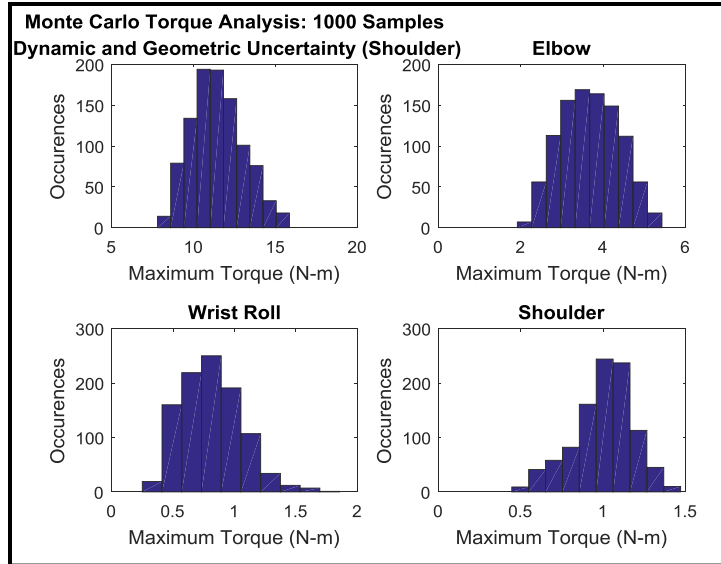


Figure 82: Monte Carlo Analysis: Maximum Torque.

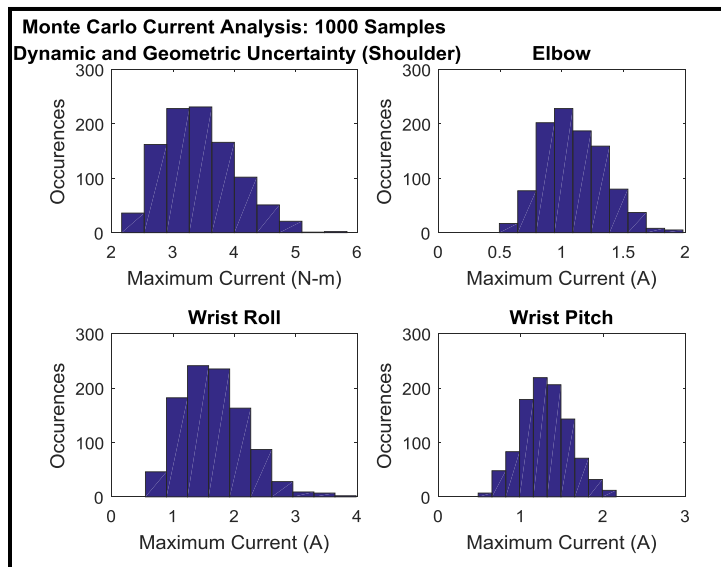


Figure 83: Monte Carlo Analysis: Maximum Current.

In none of the simulations were the maximum allowable thresholds for voltage, current or torque exceeded. In total, the results of 4000 simulations are included in Figs. 75, 76, 77, 79, and 81-83. The simple fact that each simulation was able to execute and

yield results in an expected range indicates that the design is stable for at least 4000 different combinations of perturbed dynamic and kinematic properties. This is a reliability margin of at least **99.975%** that the device will not fail as a result of the dynamic loads that are likely to be placed upon it, unknown environmental disturbance forces, measurement uncertainty/noise, servo rate limitations, and uncertainty in motor dynamics brought on by the effects of radiation.

The simulation does not take into account the probability of failure in the manipulator due to changes in its material properties caused by radiation or faults in its electronics; however the likelihood of these failure modes are considered to be low due to the fact that they can be avoided by routine inspection. Quantifying the probability of structural failure or integrated circuit upset due to radiation is a highly complex and situationally dependent problem that lies outside the scope of this paper. The Monte Carlo simulation results provide a good *bulk estimation* of the probability of failure and it is determined that the design is robustly stable and reliable.

6-3: Control Implementation and Preliminary Testing

With simulation results suggesting a high degree of confidence that the robot will be able to withstand expected dynamic loads and execute the motion required to accomplish its intended task, the device can be fully assembled and subjected to preliminary input response testing.

The real-time programming language chosen for this robot is LabVIEW™ due to its proven success as a platform that can seamlessly communicate through software with a wide range of hardware devices such as data acquisition devices (DAQs), signal generators, and microcontrollers. LabVIEW™ can handle very large numbers on data inputs and outputs, and execute algorithms at speeds fast enough to satisfy the servo rate requirements discussed in the previous section. In addition, LabVIEW™ is a graphical programming language and is natively equipped with a graphical-user-interface (GUI) that allows the operator to monitor the state of a system via virtual displays such as plots and gauges. A schematic diagram for executing real-time control of the robot arm can be seen in the figure below.

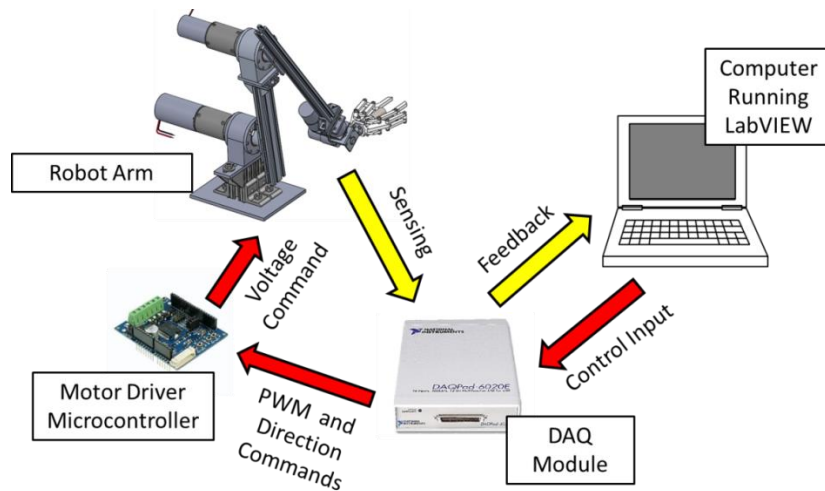


Figure 84: Robot Arm Real-Time Control Schematic Diagram.

The LabVIEW™ programming environment interacts with the robot arm by iterating in a constant loop, during which, angular position and current feedback signals from sensors

at the joints and on the motor drivers respectively are sampled via the data acquisition module (DAQ). These signals are interpreted by the program, and the desired system inputs are computed. For brushed DC motor control, these inputs are generated in the form of a Pulse-Width-Modulated (PWM) square waveform, in which the *percent-duty-cycle* of the wave corresponds to the voltage applied across the motor terminals. The directions of rotation are expressed via digital signals and logic gates. This information is sent from the DAQ to motor-driver microcontrollers that interpret them and apply the desired voltages across the motor terminals. The actual representation of this setup can be seen in the figure below.

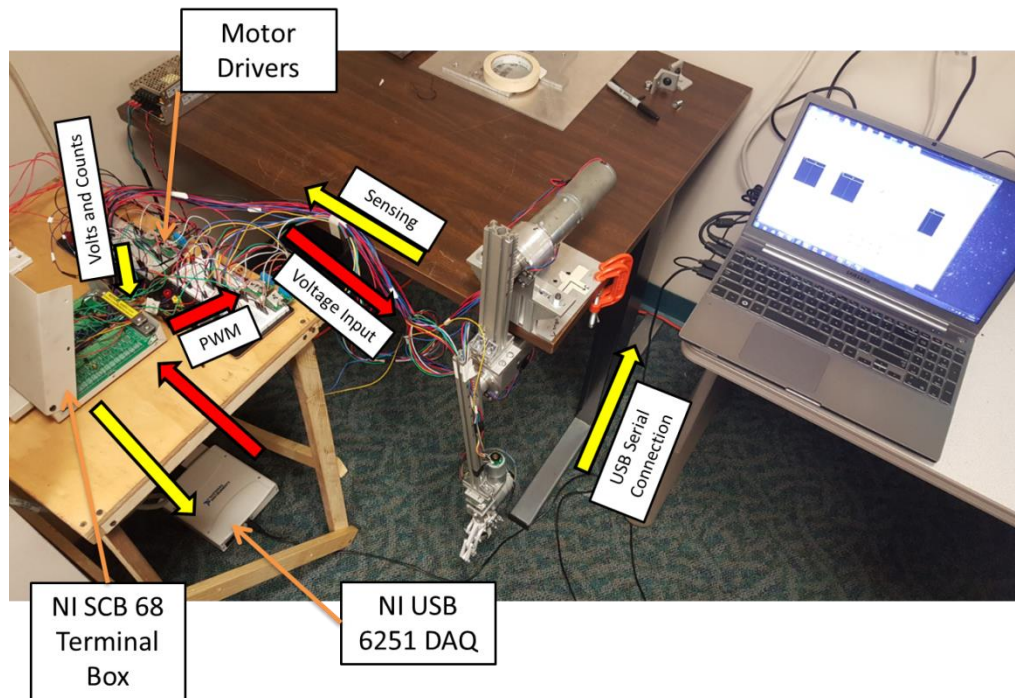


Figure 85: Robot Arm Real-Time Control Configuration.

To integrate the control algorithm designed in the previous section with the physical system, a National Instruments NI USB-6251 DAQ device with an SCB-68 terminal connector block is used to interface the software with the sensors and motor drivers. The USB-6251 is connected via a USB serial cable to a computer where the control algorithm (written in the LabVIEW™ language) runs in a continuous loop. Before the control system can go online, it is necessary to test the input/output response of the physical system. Several step input tests are conducted and the steady-state results are compared to the model predictive values. The results of this can be seen in Table 13 below.

Shoulder Step Input Response Comparison					
Step Input (% Duty Cycle)	Steady State Voltage Response (V)	Steady State Current (A)	Steady State Angular Response	Model SS Angle from Voltage Step	Model SS Current (A)
10	1.44	1.33	-163°	-158°	0.82
15	2.18	1.83	-126°	-145°	1.24
Elbow Step Input Response Comparison					
Step Input (% Duty Cycle)	Steady State Voltage Response (V)	Steady State Current (A)	Steady State Angular Response	Model SS Angle from Voltage Step	Model SS Current (A)
10	1.7	0.41	4.85°	28°	0.28
20	3.57	0.79	32.6°	60°	0.6
30	5.53	1.12	90°	90° @ ≈ 4.7V	0.8
Wrist Roll Step Input Response Comparison					
Step Input (% Duty Cycle)	Steady State Voltage Response (V)	Steady State Current (A)	Steady State Angular Response	Model SS Angle from Voltage Step	Model SS Current (A)
5	1.19	0.3			0.5
10	3.1	0.4			0.7
Wrist Pitch Step Input Response Comparison					
Step Input (% Duty Cycle)	Steady State Voltage Response (V)	Steady State Current (A)	Steady State Angular Response	Model SS Angle from Voltage Step	Model SS Current (A)
5	0.5	0.41	-56°	34°	0.2
7	0.7	0.5	≈90°	52°	0.3

Table 13: Step Response Comparisons.

These results indicate some degree of error likely caused by inaccuracies in the friction model of the system. Observed motion of the device suggests that the friction

force within the joint is a function of angular position as well as angular velocity. In other words, certain parts of the range of motion tend to “stick” more than others. These sorts of forces are included in the category of “environmental disturbances” discussed in the previous section, and it is assumed that the controller will be able to overcome them during operation.

With the control hardware in place and configured to send and receive information to and from the device, the project can transition from the modelling phase to the tuning, troubleshooting and testing phase. While online, the control system will need to be running continuously in order to keep the robot stable. In other words, there can be no point in time in which the controllers are not receiving feedback from the system and generating control inputs. This is accomplished with a “finite-state-machine” (FSM) control scheme. The FSM principle is a modular representation of real-time control in which a device (machine) is programmed to remain in one of a certain, finite number of predefined states until it is cued to transition to a new one. Each “state” of the device can either be a position that it is required to hold, or a sequence of actions that it is required to perform, and the “transition cues” can either be inputs from a human operator, or signals detected via sensors. For this single-arm robot to accomplish its task it must exist in one of two *finite-states* at any instant: these are defined as the *Hold Position Loop* and the *Transition Loop*. These two states are characterized by the robot holding its current position, and transitioning to a new (reference) position respectively. At any point, the robot is either in a desired, stable configuration with its end-effector in a desired location, or it has received the coordinates of a new target location, and it is tracking the reference trajectory required for it to execute the transition to it. The information passed between

the two loops are angular state of the robot before and after transition, $\vec{\theta}(0)$ and $\vec{\theta}(t_f)$, the reference position of the end-effector, z_{ref}, y_{ref} , and the nominal torque required to hold the manipulator its static configuration at the end of a transition, $\vec{\tau}(t_f)$. A schematic representation of this can be seen on the next page.

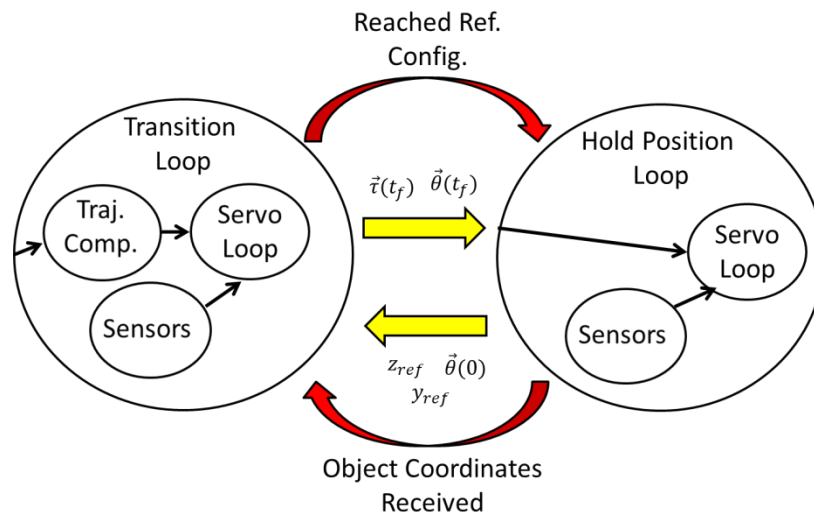


Figure 86: Robot Arm Finite-State-Machine Representation.

Control of the robot in this way is versatile and efficient because the transition cue that triggers the robot to move from *transition* to *hold* can either be a signal from an object detection sensor, or it can be an input from an operator, and LabVIEW™ is very well suited for implementing this type of control strategy. Once the control algorithm is written in LabVIEW and fully debugged, the robot arm can be put online and given sample reference positions, and its response to the controller can be observed and evaluated.

CHAPTER 7: CONCLUSIONS AND FUTURE WORK

The design of the single-arm robotic manipulator presented in this paper accomplishes each of the original objectives of simplicity, cost effectiveness, reliability, modularity, versatility and semi-autonomy. The kinematic shape of the four degree of freedom robot and its corresponding work envelop give it the freedom of a wide range of motion and orientation capabilities. The versatility of this robot is not limited by its shape due to the fact that it can be implemented with different varieties of base mobility. Furthermore, the adjustable nature of its links allows it to be configured for specific tasks and comply with space limitations. The mechanical design is very robust and tolerant to a harsh environment, and the assembly is modular and can compartmentalize damage.

The primary success of this project was the development of a comprehensive system kinematic and dynamic model. Up until this point in the project, an accurate and specific computational dynamic model had not been developed and this placed large limitations on the extent and confidence of accuracy and reliability studies. The model was found to be accurate with respect to the prototype through model validation testing and analysis. Once an accurate model was obtained, the project was able to proceed into developing a control specifically related to its own dynamic tendencies. Extensive testing of the controller via Monte Carlo simulation suggests robust stability and performance, as well as reliability against failure due to dynamic loading over a range of dynamic and kinematic uncertainties. The positioning accuracy of the robot was also determined to be within tolerable limits despite the application of uncertainties.

Construction of a full prototype has proven that the device can move in a desired fashion and support the predicted loading. Testing and configuration of the control hardware has proven that the process data required for achieving control can be collected, and that the necessary control signals can be generated.

The future of this project will be focused on preparing the robot arm for the transition from prototype to functional device. The primary focus of this will be on integrating the simulated control process with the physical robot arm and obtaining accuracy and repeatability measurements. This must be done by implementing object detection sensors and object handling capabilities. In addition, a convenient user interface that allows an operator to change the task of the robot arm or take manual control would be desirable.

Another focus should be on the position sensing at the shoulder and elbow joints. The hall arrays that were used in these areas are experimental and thus are attached to the device in a somewhat crude and inconvenient fashion. An optimized design of this could feature a rapid-manufactured “sensor-array-platform” that the sensors could be fastened onto before they are added onto the joint housing. This concept would certainly add modularity to the design and could also help with obtaining a consistent and reliable signal response from the sensing array.

Identifying and implementing a specific base design is another possible route. Once a base is designed and incorporated, a subroutine in the control program will need to be added to govern control over it.

Added sensing and handling capabilities to the end effector design as mentioned in the final chapter should also be considered. Furthermore, incorporating some design

and control algorithm in which the robot could select from a variety of different end effectors on its own would be a novel approach to accomplishing versatility.

In summary, there are numerous directions in which the project could theoretically proceed, and the design presented in this paper will be the foundation that will make that possible. With the structural design, dynamic model, and control scheme established and validated, design work can begin to focus on the interface between the robot and its surroundings and how to govern the interactions between the two.

BIBLIOGRAPHY

- 1) B. M. Harpel, J. B. Dugan, I. D. Walker, J. R. Cavallaro. "Analysis of Robots for Hazardous Environments," Proceedings of the Annual Reliability and Maintainability Symposium, p 111-116, 1997.
- 2) R. M. Murray, Z. Li, S. Shankar Sastry. "A Mathematical Introduction to Robotic Manipulation," CRC Press Inc., Boca Raton, FL, 1994.
- 3) L. Sciavicco, B. Siciliano. "Modelling and Control of Robot Manipulators," Springer-Verlag London, 2000.
- 4) H. Wang, S. Li, Y. F. Zheng. "Analysis of Radiation Effects on DC Motorized Manipulator," IEEE International Conference on Control, Automation and Robotics, p 238-242, 2016.
- 5) S. Li, Y. F. Zheng, J. Qiu, et al., "Performance analysis on radiation degraded BLDC motor in robot servo systems," IEEE International Conference on Electro Information Technology, p 038-043, 2015.
- 6) O. P. Kahkonen, S. Makinen, M. Talvitie, M. Manninen, "Radiation damage in Nd-Fe-B magnets: temperature and shape effects," Journal of Physics: Condensed Matter, Vol. 4, No. 4, p 1007, 1992.
- 7) J. Forlizzi, C. DiSalvo, "Service Robots in the Domestic Environment: A Study of the Roomba Vacuum in the Home," Proceedings of the 1st ACM SIGCHI/SIGART conference on Human-robot interaction, 2006
- 8) K. Kawamura, R. T. Pack and M. Iskarous, "Design Philosophy for Service Robots," Proceedings. IEEE Annual Reliability and Maintainability Symposium, p 111-116, 1997.
- 9) K. Iagnemma, S. Dubowsky, "Mobil Robot Rough-Terrain Control for Planetary Exploration," The 26th ASME Biennial Mechanisms and Robotics Conference, DETC, Vol. 2000, 2000.
- 10) J. Iqbal, A. M. Tahir, R. U. Islam, and R. U. Nabi, "Robotics for Nuclear Power Plants – Challenges and future Perspectives," IEEE 2nd International Conference on Applied Robotics for the Power Industry, 2012.
- 11) A. Hamilton, S. J. Burany, S. B. Peralta, and L. Greenland, "Robotic Removal of High-Activity Debris from a Nuclear Primary Heat Transfer System," IEEE 1st International Conference on Applied Robotics for the Power Industry, 2010.

- 12) A. Golderberg, M. Gryniewski, T. Campbell, "AARM: A robot arm for internal operations in nuclear reactors," IEEE 1st International Conference on Applied Robotics for the Power Industry, p 1-5, 2010.
- 13) IAEA technical report, "Nuclear power plant outage optimization strategy," Report no. EAEA-TECDOC-1315.
- 14) L. Gargiulo, P. Bayetti, V. Bruno, et. al. "Development of an ITER relevant inspection robot," Journal of Fusion Engineering and Design, vol. 83(10-12), p 1833-1836, 2008.
- 15) P. E. Dodd, and L. W. Massengill, "Basic mechanisms and modelling of single-event upset in digital microelectronics," IEEE Transactions on Nuclear Science, vol. 50, no. 3, p 583-602, 2003.
- 16) A. S. Keys, and M. D. Watson, "Radiation Hardened Electronics for Extreme Environments", vol. 4, 2007.
- 17) D. J. Barnhart, "Radiation Hardening by Design of Asynchronous Logic for Hostile Environments," IEEE Journal of Solid-State Circuits, vol. 44, issue 5, p 1617-1628, 2009.
- 18) K. Nagatani, et al, "Gamma-ray irradiation test of Electric components of rescue mobile robot Quince," IEEE International Symposium on Safety, Security, and Rescue Robotics (SSRR), 2011.
- 19) G. Piolain, et al, "Dedicated and Standard Industrial Robots used as Force-Feedback Telemaintenance Remote Devices at the AREVA recycling plant," IEEE 1st International Conference on Applied Robotics for the Power Industry (CAPRI), 2010.
- 20) J. Alderman, "Measurement of radiation-induced demagnetization of Nd-Fe-B permanent magnets," Nuclear instruments & methods in physics research: Section A, Accelerators, spectrometers, detectors and associated equipment, vol. 481, issue 1-3, p 9-28, 2002.
- 21) T.S. White, N. Hewer, B.L. Luk, and J. Hazel, "Design and Operational Performance of a Climbing Robot used for Weld Inspection in Hazardous Environments," IEEE International Conference on Control Applications, p. 451-455, Trieste, Italy, 1998.
- 22) I. D. Walker, J. R. Cavallaro, "The Use of Fault Trees for the Design of Robots for Hazardous Environments," Proceedings. IEEE Annual Reliability and Maintainability Symposium, p. 229-235, 1996.

- 23) Z. Shi, "Reliability Analysis and Synthesis of Robot Manipulators," Proceedings. IEEE Reliability and Maintainability Symposium, p. 201-205, Anaheim, CA, 1994.
- 24) M. L. Leuschen, I. D. Walker, J. R. Cavallaro, "Robot Reliability Using Fuzzy Fault Trees and Markov Models," Proceedings of SPIE, the International Society for Optical Engineering, vol. 2905, p. 73-91, October, 1996.
- 25) M. L. Leuschen, I. D. Walker, J. R. Cavallaro, "Investigation of Reliability of Hydraulic Robots for Hazardous Environments using Analytic Redundancy," Proceedings of IEEE Annual Reliability and Maintainability symposium, p. 122-128, 1999.
- 26) K. Nagatani et al., "Emergency Response to the Nuclear Accident at the Fukushima Daiichi Nuclear Power Plants using Mobile Rescue Robots," Journal of Field Robotics, Vol. 30, Iss. 1, pp. 44-63, January, 2013.
- 27) T. Oomichi et al., "Practical Design of Robots Operating in Radiation Environments," Journal of Advanced Robotics, Vol. 21, Iss. 5, pp. 515-532, 2007.
- 28) C. J. Hess and S. W. Metzger, "Steady Progress at TMI-2," IAEA Bulletin, 27, pp. 16-22, 1985.
- 29) E. Y. Chow and A. S. Willsky, "Analytical Redundancy and the Design of Robust Failure Detection Systems," IEEE Transactions on Automatic Control, Vol. 29, Iss. 7, pp. 603-614, July, 1984.
- 30) F. Lawrence, et al., "Radiation Degradation in the Mechanical Properties of Polyetheretherketone-alumina Composites," Journal of Nuclear Materials, Vol. 420, Iss. 1-3, pp. 338-341, January, 2012.
- 31) M. Celina, et al., "Polymer Materials and Component Evaluation in Acidic-Radiation Environments," Journal of Radiation Physics and Chemistry, Vol. 62, Iss. 1, pp. 153-161, July, 2001.
- 32) "Products and Services," www.murr.missouri.edu, University of Missouri Research Reactor.
- 33) H. Shulman, W.S. Ginell, et al., "Nuclear and Space Radiation Effects on Materials," NASA/SP-8053, pp. 6-16, June, 1970.
- 34) E. Ferner, A. Hoyer, and A. Sherif El-Gizawy "Remote Disassembly System for Annular Targets during Production of Mo-99," 2011 ANS Winter Meeting and Nuclear Technology Expo, Technical Conference Proceedings: The Status of Global Nuclear Deployment, Washington DC, October 30 - November 3, 2011 American Nuclear Society (2011) (CD-ROM).

Appendix A. Manipulator Kinematics

Joint Twist Coordinates:

$$\xi_1 = \begin{bmatrix} 0 \\ z_{0 \rightarrow 1} \\ -y_{0 \rightarrow 1} \\ 1 \\ 0 \\ 0 \end{bmatrix}, \xi_2 = \begin{bmatrix} 0 \\ L_1 + z_{0 \rightarrow 1} \\ -y_{0 \rightarrow 1} \\ 1 \\ 0 \\ 0 \end{bmatrix}, \xi_3 = \begin{bmatrix} y_{0 \rightarrow 1} \\ -x_{0 \rightarrow 1} \\ 0 \\ 0 \\ 0 \\ 1 \end{bmatrix}, \xi_4 = \begin{bmatrix} 0 \\ L_1 + L_2 + z_{0 \rightarrow 1} \\ -y_{0 \rightarrow 1} \\ 1 \\ 0 \\ 0 \end{bmatrix}$$

Joint Homogeneous Transformations:

$$e^{\xi_1 \theta_1} = \begin{bmatrix} 1 & 0 & 0 & 0 \\ 0 & \cos(\theta_1) & -\sin(\theta_1) & z_{0 \rightarrow 1} \sin(\theta_1) - y_{0 \rightarrow 1}(\cos(\theta_1) - 1) \\ 0 & \sin(\theta_1) & \cos(\theta_1) & -z_{0 \rightarrow 1}(\cos(\theta_1) - 1) - y_{0 \rightarrow 1} \sin(\theta_1) \\ 0 & 0 & 0 & 1 \end{bmatrix}$$

$$e^{\xi_2 \theta_2} = \begin{bmatrix} 1 & 0 & 0 & 0 \\ 0 & \cos(\theta_2) & -\sin(\theta_2) & (L_1 + z_{0 \rightarrow 1}) \sin(\theta_2) - y_{0 \rightarrow 1}(\cos(\theta_2) - 1) \\ 0 & \sin(\theta_2) & \cos(\theta_2) & -(L_1 + z_{0 \rightarrow 1})(\cos(\theta_2) - 1) - y_{0 \rightarrow 1} \sin(\theta_2) \\ 0 & 0 & 0 & 1 \end{bmatrix}$$

$$e^{\xi_3 \theta_3} = \begin{bmatrix} \cos(\theta_3) & -\sin(\theta_3) & 0 & y_{0 \rightarrow 1} \sin(\theta_3) - x_{0 \rightarrow 1}(\cos(\theta_3) - 1) \\ \sin(\theta_3) & \cos(\theta_3) & 0 & -y_{0 \rightarrow 1}(\cos(\theta_3) - 1) - x_{0 \rightarrow 1} \sin(\theta_3) \\ 0 & 0 & 1 & 0 \\ 0 & 0 & 0 & 1 \end{bmatrix}$$

$$e^{\xi_4 \theta_4} = \begin{bmatrix} 1 & 0 & 0 & 0 \\ 0 & \cos(\theta_4) & -\sin(\theta_4) & (L_1 + L_2 + z_{0 \rightarrow 1}) \sin(\theta_4) - y_{0 \rightarrow 1}(\cos(\theta_4) - 1) \\ 0 & \sin(\theta_4) & \cos(\theta_4) & -(L_1 + L_2 + z_{0 \rightarrow 1})(\cos(\theta_4) - 1) - y_{0 \rightarrow 1} \sin(\theta_4) \\ 0 & 0 & 0 & 1 \end{bmatrix}$$

Forward Kinematics Transformation:

Notation: $s_1 = \sin(\theta_1)$, $c_1 = \cos(\theta_1)$, $s_{12} = \sin(\theta_1 + \theta_2)$, $c_{12} = \cos(\theta_1 + \theta_2)$

$$g_{st}(\vec{\theta}) = \begin{bmatrix} c_3 & -c_4s_3 & s_3s_4 & x_{0 \rightarrow 1} + L_3s_3s_4 \\ c_{12}s_3 & c_{12}c_3c_4 - s_{12}s_4 & -s_{12}c_4 - c_{12}c_3s_4 & y_{0 \rightarrow 1} - L_1s_1 + L_2(-c_1s_2 - c_2s_1) + L_3(-c_1c_4s_2 - c_2c_4s_1 - c_1c_2c_3s_4 + c_3s_1s_2s_4) \\ s_{12}s_3 & c_{12}s_4 + s_{12}c_3c_4 & c_{12}c_4 - s_{12}c_3s_4 & z_{0 \rightarrow 1} + L_1c_1 + L_2(c_1c_2 - s_2s_1) + L_3(c_1c_2c_4 - c_4s_1s_2 - c_1s_2c_3s_4 - c_2c_3s_1s_4) \\ 0 & 0 & 0 & 1 \end{bmatrix}$$

Backward Kinematics Transformation:

$$g_{ts}(\vec{\theta}) = \begin{bmatrix} (g_{st,1:3,1:3})^T & -(g_{st,1:3,1:3})^T g_{st,1:3,4} \\ 0 & 1 \end{bmatrix}$$

Kinematic Properties:

Kinematic Lengths			
Link Lengths:	$L_1 = 8.5$	$L_2 = 13$	$L_3 = 6.28$
Base Frame Initial Offsets	$x_{0 \rightarrow 1} = 4.623$	$y_{0 \rightarrow 1} = -2.75$	$z_{0 \rightarrow 1} = 5.00$

Table 14: Kinematic Properties.

Appendix B. Manipulator Dynamics

Link Jacobians:

- *Link 1:*

$$\xi_{L_1}^+ = Ad_{(e^{\widehat{\xi}_1 \theta_1} g_{sl_1}(0))}^{-1} \xi_1$$

$$g_{sl_1}(0) = \begin{bmatrix} R_{0L_1} & \vec{p}_{0L_1} \\ 0 & 1 \end{bmatrix}$$

$$R_{0L_1} = \begin{bmatrix} 0.9598 & 0 & -0.2805 \\ 0 & 1 & 0 \\ 0.0116 & 0 & 0.9599 \end{bmatrix}$$

$$\vec{p}_{0L_1} = \begin{bmatrix} x_{0 \rightarrow 1} - c_2 \\ y_{0 \rightarrow 1} \\ z_{0 \rightarrow 1} + c_1 \end{bmatrix}$$

$$J_1 = \begin{bmatrix} 0 & 0 & 0 & 0 \\ -c_1 & 0 & 0 & 0 \\ 0 & 0 & 0 & 0 \\ 0.9598 & 0 & 0 & 0 \\ 0 & 0 & 0 & 0 \\ 0 & 0 & 0 & 0 \end{bmatrix}$$

- *Link 2:*

$$\xi_{L_1}^+ = Ad_{(e^{\widehat{\xi}_1 \theta_1} e^{\widehat{\xi}_2 \theta_2} g_{sl_2}(0))}^{-1} \xi_1$$

$$\xi_{L_1}^+ = Ad_{(e^{\widehat{\xi}_2 \theta_2} g_{sl_2}(0))}^{-1} \xi_2$$

$$g_{sl_2}(0) = \begin{bmatrix} R_{0L_2} & \vec{p}_{0L_2} \\ 0 & 1 \end{bmatrix}$$

$$R_{0L_2} = \begin{bmatrix} 0.9999 & 0 & -0.0116 \\ 0 & 1 & 0 \\ 0.0116 & 0 & -0.3742 \end{bmatrix}$$

$$\vec{p}_{0L_2} = \begin{bmatrix} x_{0 \rightarrow 1} - c_4 \\ y_{0 \rightarrow 1} \\ z_{0 \rightarrow 1} + L_1 + c_3 \end{bmatrix}$$

$$J_2 = \begin{bmatrix} 0.0116 L_1 \sin(\theta_2) & 0 & 0 & 0 \\ -c_3 - L_1 \cos(\theta_2) & -c_3 & 0 & 0 \\ 0.9999 L_1 \sin(\theta_2) & 0 & 0 & 0 \\ 0.9999 & 0.9999 & 0 & 0 \\ 0 & 0 & 0 & 0 \\ -0.0116 & -0.0116 & 0 & 0 \end{bmatrix}$$

- *Link 3:*

$$\xi_{L_1}^+ = Ad_{(e^{\widehat{\xi}_1 \theta_1} e^{\widehat{\xi}_2 \theta_2} e^{\widehat{\xi}_3 \theta_3} g_{sl_3}(0))}^{-1} \xi_1$$

$$\xi_{L_1}^+ = Ad_{(e^{\widehat{\xi}_2 \theta_2} e^{\widehat{\xi}_3 \theta_3} g_{sl_3}(0))}^{-1} \xi_2$$

$$\xi_{L_1}^+ = Ad_{(e^{\widehat{\xi}_3 \theta_3} g_{sl_3}(0))}^{-1} \xi_3$$

$$g_{sl_3}(0) = \begin{bmatrix} R_{0L_3} & \vec{p}_{0L_3} \\ 0 & 1 \end{bmatrix}$$

$$R_{0L_3} = \begin{bmatrix} -0.3742 & 0 & 0.9273 \\ 0 & 1 & 0 \\ 0.9273 & 0 & -0.3742 \end{bmatrix}$$

$$\vec{p}_{0L_3} = \begin{bmatrix} x_{0 \rightarrow 1} - c_6 \\ y_{0 \rightarrow 1} \\ z_{0 \rightarrow 1} + L_1 + c_5 \end{bmatrix}$$

$$J_3(:,1)$$

$$= \begin{bmatrix} 0.3742(c_5 \sin(\theta_3) + L_1 \cos(\theta_2) \sin(\theta_3)) + 0.9273(-L_1 \sin(\theta_2) + c_6 \sin(\theta_3)) \\ -\cos(\theta_3)(c_5 + L_1 \cos(\theta_2)) \\ 0.3742(c_6 \sin(\theta_3) - L_1 \sin(\theta_2)) + 0.9273(-L_1 \cos(\theta_2) \sin(\theta_3) - c_5 \sin(\theta_3)) \\ -0.3742 \cos(\theta_3) \\ -\sin(\theta_3) \\ 0.9273 \cos(\theta_3) \end{bmatrix}$$

$$J_3(:,2) = \begin{bmatrix} 0.3742 c_5 \sin(\theta_3) + 0.9273 c_6 \\ -c_5 \cos(\theta_3) \\ -0.9273 c_5 \sin(\theta_3) + 0.3742 c_6 \sin(\theta_3) \\ -0.3742 \cos(\theta_3) \\ -\sin(\theta_3) \\ 0.9273 \cos(\theta_3) \end{bmatrix}$$

$$J_3(:,3) = \begin{bmatrix} 0 \\ -c_6 \\ 0 \\ -0.9273 \\ 0 \\ -0.3742 \end{bmatrix}$$

$$J_3(:,4) = \begin{bmatrix} 0 \\ 0 \\ 0 \\ 0 \\ 0 \\ 0 \end{bmatrix}$$

- *Link 4:*

$$\xi_{L_1}^+ = Ad_{(e^{\widehat{\xi}_1 \theta_1} e^{\widehat{\xi}_2 \theta_2} e^{\widehat{\xi}_3 \theta_3} e^{\widehat{\xi}_4 \theta_4} g_{sl_4}(0))}^{-1} \xi_1$$

$$\xi_{L_2}^+ = Ad_{(e^{\widehat{\xi}_2 \theta_2} e^{\widehat{\xi}_3 \theta_3} e^{\widehat{\xi}_4 \theta_4} g_{sl_4}(0))}^{-1} \xi_2$$

$$\xi_{L_3}^+ = Ad_{(e^{\widehat{\xi}_3 \theta_3} e^{\widehat{\xi}_4 \theta_4} g_{sl_4}(0))}^{-1} \xi_3$$

$$\xi_{L_4}^+ = Ad_{(e^{\widehat{\xi}_4 \theta_4} g_{sl_4}(0))}^{-1} \xi_4$$

$$g_{sl_4}(0) = \begin{bmatrix} R_{0L_4} & \vec{p}_{0L_4} \\ 0 & 1 \end{bmatrix}$$

$$R_{0L_4} = \begin{bmatrix} 1 & 0 & 0 \\ 0 & 1 & 0 \\ 0 & 0 & 1 \end{bmatrix}$$

$$\vec{p}_{0L_4} = \begin{bmatrix} x_{0 \rightarrow 1} + c_8 \\ y_{0 \rightarrow 1} \\ z_{0 \rightarrow 1} + L_1 + L_2 + c_7 \end{bmatrix}$$

$$J_4(:,1)$$

$$= \begin{bmatrix} -\sin(\theta_3)(L_2 + L_1 \cos(\theta_2) + c_7 \cos(\theta_4)) \\ L_1 \sin(\theta_2) \sin(\theta_4) - L_2 \cos(\theta_3) \cos(\theta_4) - c_7 \cos(\theta_3) + c_8 \sin(\theta_3) \sin(\theta_4) - L_1 \cos(\theta_2) \cos(\theta_3) \cos(\theta_4) \\ L_1 \cos(\theta_4) \sin(\theta_2) + L_2 \cos(\theta_3) \sin(\theta_4) + c_8 \cos(\theta_4) \sin(\theta_3) + L_1 \cos(\theta_2) \cos(\theta_3) \sin(\theta_4) \\ \cos(\theta_3) \\ -\cos(\theta_4) \sin(\theta_3) \\ \sin(\theta_3) \sin(\theta_4) \end{bmatrix}$$

$$J_4(:,2) = \begin{bmatrix} -\sin(\theta_3)(L_2 + c_7 \cos(\theta_4)) \\ c_8 \sin(\theta_3) \sin(\theta_4) - L_2 \cos(\theta_3) \cos(\theta_4) - c_7 \cos(\theta_3) \\ L_2 \cos(\theta_3) \sin(\theta_4) + c_8 \cos(\theta_4) \sin(\theta_3) \\ \cos(\theta_3) \\ -\cos(\theta_4) \sin(\theta_3) \\ \sin(\theta_3) \sin(\theta_4) \end{bmatrix}$$

$$J_4(:,3) = \begin{bmatrix} c_7 \sin(\theta_4) \\ c_8 \cos(\theta_4) \\ -c_8 \sin(\theta_4) \\ 0 \\ \sin(\theta_4) \\ \cos(\theta_4) \end{bmatrix}$$

$$J_4(:,4) = \begin{bmatrix} 0 \\ -c_7 \\ 0 \\ 1 \\ 0 \\ 0 \end{bmatrix}$$

Link Dynamic Properties:

Dynamic Properties				
Link	1	2	3	4
Mass (kg)	2.58	0.805	0.325	0.225
C.O.M. Location (inches)	$c_1 = 6.814$	$c_3 = 5.895$	$c_5 = 13.04$	$c_7 = 3.475$
	$c_2 = 4.186$	$c_4 = 1.036$	$c_6 = 1.418$	$c_8 = 0$
Inertial Properties	$I_{xx} = 18,445$	$I_{xx} = 15,019$	$I_{xx} = 280$	$I_{xx} = 279$
	$I_{yy} = 24,040$	$I_{yy} = 14,426$	$I_{yy} = 306$	$I_{yy} = 342$
	$I_{zz} = 6,738$	$I_{zz} = 571$	$I_{zz} = 77.5$	$I_{zz} = 79.7$

Table 15: Dynamic Properties.

Representation in SOLIDWORKS™:

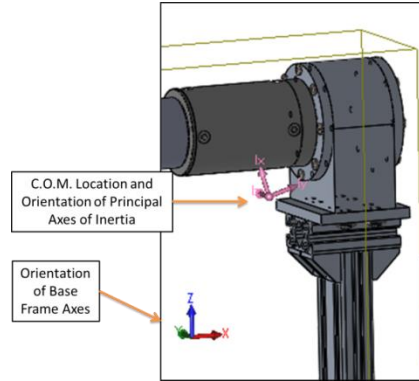


Figure 87: Shoulder Principal Axes of Inertia and C.O.M.

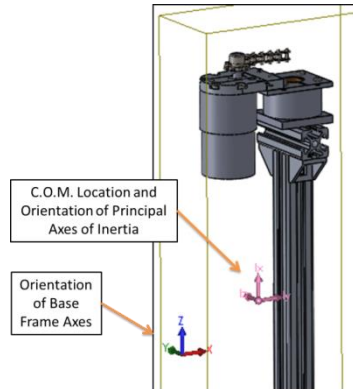


Figure 88: Elbow Principal Axes of Inertia and C.O.M.

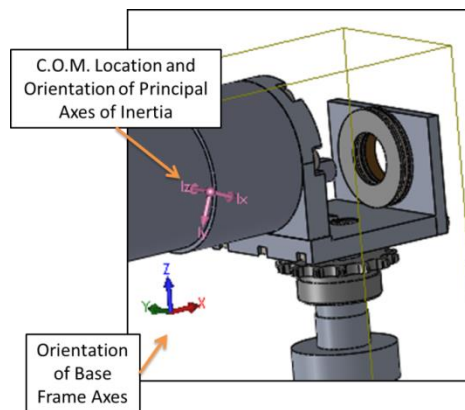


Figure 89: Wrist Principal Axes of Inertia and C.O.M.

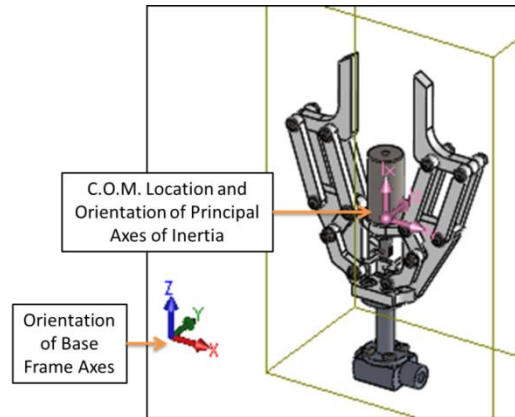


Figure 90: End Effector Principal Axes of Inertia and C.O.M.

Dynamic Loading Plots for Structure and Motor Evaluation:

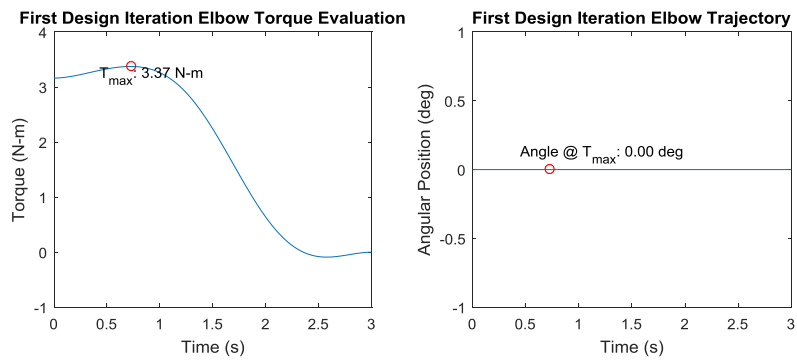


Figure 91: First Iteration Elbow Torque Evaluation.

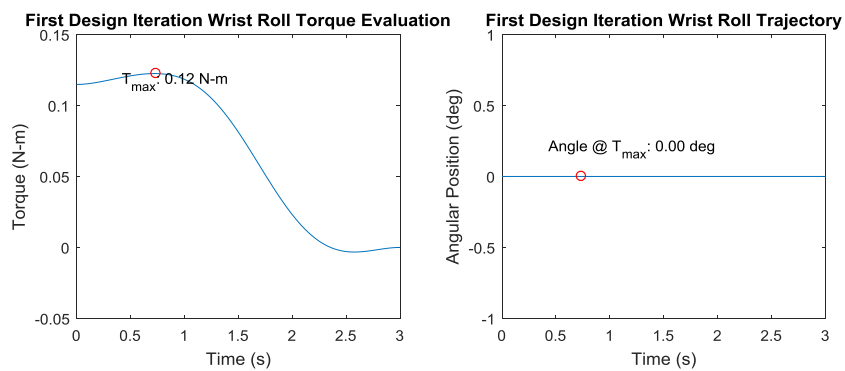


Figure 92: First Iteration Wrist Roll Torque Evaluation.

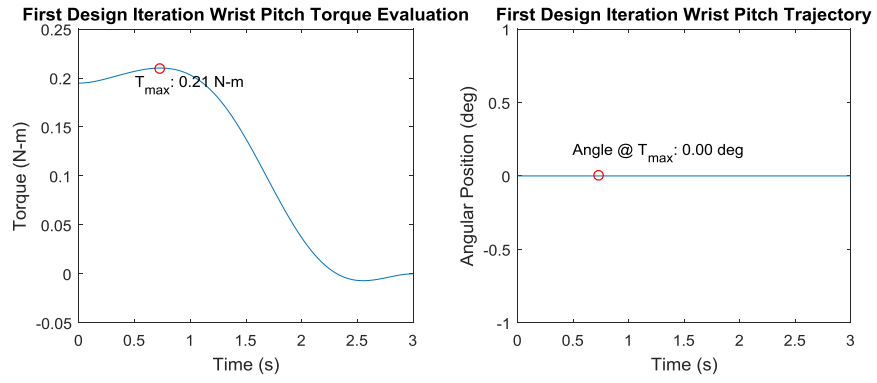


Figure 93: First Iteration Wrist Pitch Torque Evaluation.

Appendix C. Hall Array Calibration

Calibration Stand and Configuration:

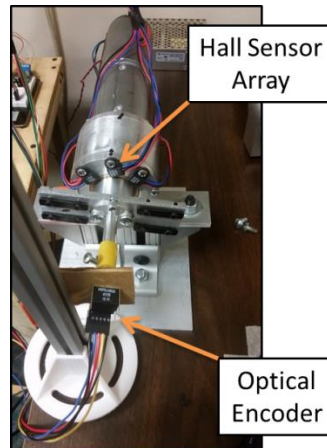


Figure 94: Hall Array Calibration Setup.

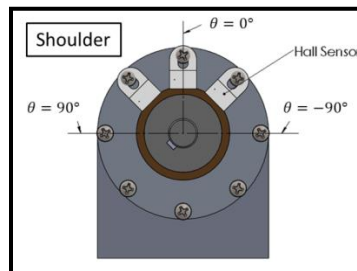


Figure 95: Shoulder Hall Sensor Array Configuration.

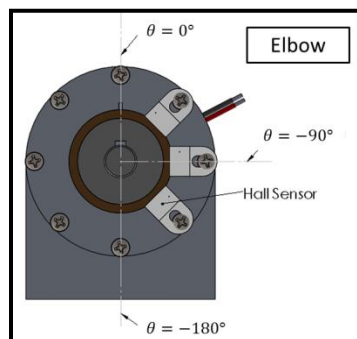


Figure 96: Elbow Hall Sensor Array Configuration.

- Sensors are placed such that they capture the necessary range of motion of the joint.
- For the shoulder, this spans roughly $-90^\circ \leq \theta \leq 90^\circ$.
- For the elbow, the total range of motion is roughly $-170^\circ \leq \theta \leq 170^\circ$.
- A rotation of $+\theta$ is equivalent to a rotation of $-\theta$ coupled with a base rotation of 180° .
- Thus half of the range of motion can be covered with no loss of manipulator reach capability.
- Reduces risk of measurement error due to calibration.

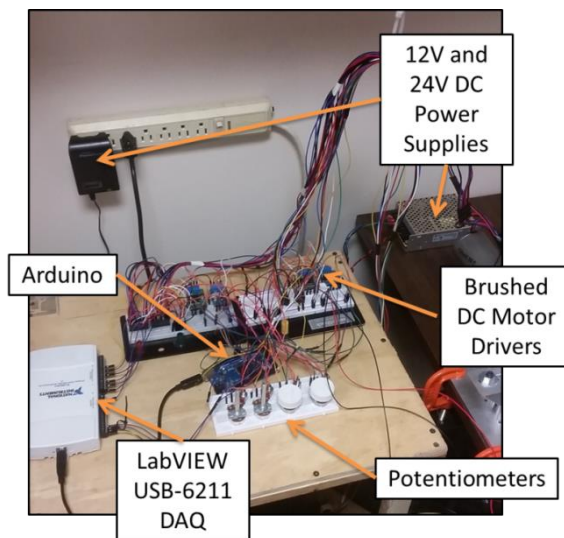


Figure 97: Data Acquisition and Motor Control For Calibration.

- Motors are turned while measurements are recorded from the angular encoder and the hall array.

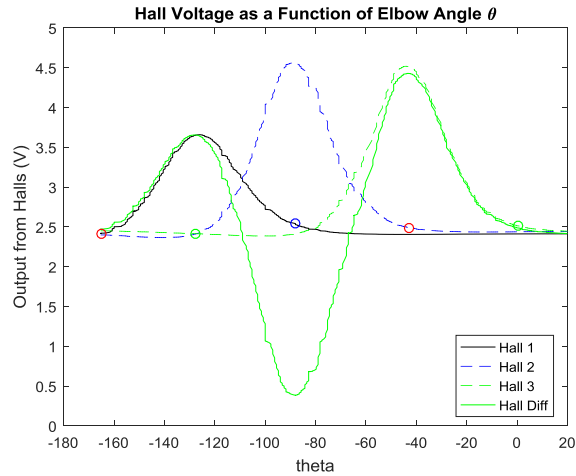


Figure 98: Hall Array Measurements as Function of Angular Position.

- Measurements are plotted together to express hall array measurements as function of angular rotation.
- One measurement is desired as a basis of direct relation between the hall array measurement and angular position, thus the hall difference is used:

$$V_{hall} = V_{hall1} - V_{hall2} + V_{hall3}$$

- The function of angular position vs. hall difference is not one-to-one, therefore one formula cannot be used to express position from hall measurement over the entire range of motion.
- Function is broken into one-to-one segments and a sparse set of the collected data is tabulated so that “lookup tables” for determining position from hall difference can be constructed and used in real-time.
- Linear interpolation is used to estimate angular positions that lie between evaluation points.

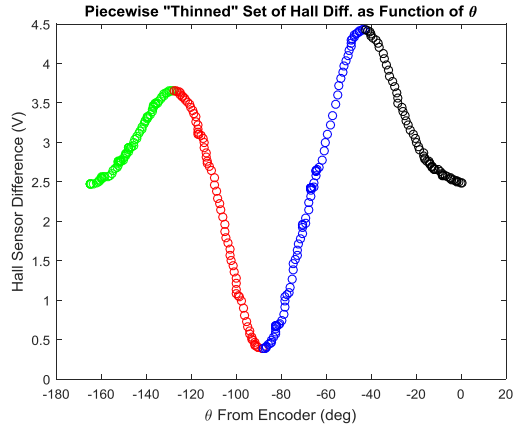


Figure 99: Sparse Set of Hall Array Measurement vs. Angular Position.

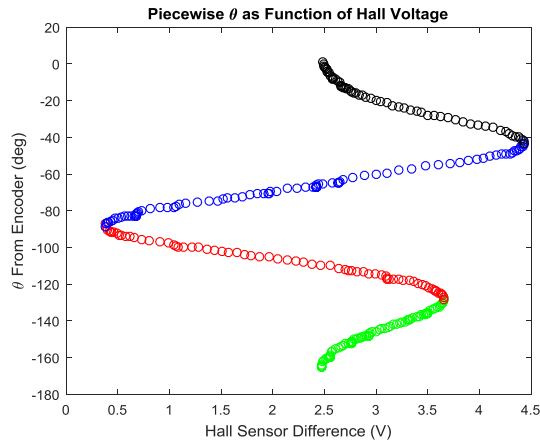


Figure 100: Graphical Angular Position vs. Hall Measurement Lookup Table.

- The index points (points in which the function transitions from one table to the next) are determined from individual hall sensor measurements.
- Comparison of readings from two adjacent sensors determines which region the angular position is in, and interpolation of the hall difference vs. angular position table determines exact position.

- To check the calibration, hall array measurement data is used to “re-construct” angular position. This is compared to angular position measured directly by the optical encoder.

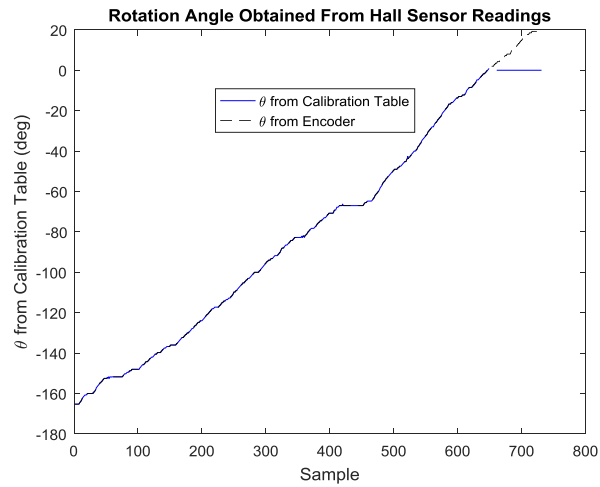


Figure 101: Sample of Angular Position from both Encoder and Hall Array.

Appendix D. Accelerometer Calibration

Accelerometer Calibration:

- Accelerometer voltage output is directly proportional to acceleration.
- Calibration requires establishment of two things:
 - A Reference Zero Reading
 - A Reference Know Acceleration
- From these two items, a sensitivity factor can be determined (in Volts per unit of Acceleration).
- The Reference Zero Reading is established in the following manner:
 - The accelerometer is mounted to a spool as shown and the spool is rotated about its axis.
 -

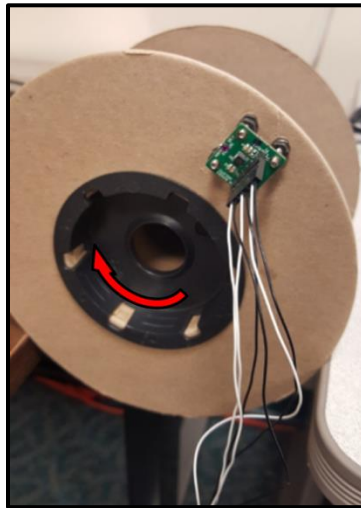


Figure 102: Accelerometer Reference Zero Calibration.

- Static readings from the accelerometer are sampled at an array of positions during rotation.

- If the axis of rotation remains fixed and does not coincide with a coordinate axis of the accelerometer, then the output response from each axis will fluctuate (as a result of gravitational acceleration) between a maximum and minimum value over the course of one rotation.
- Thus the average response over a full rotation represents the Reference Zero Reading

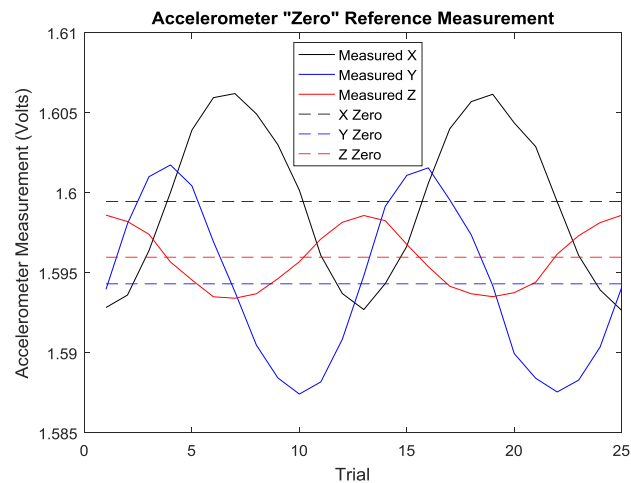


Figure 103: Accelerometer Measurement during Rotation about an Arbitrary Axis.

- The Reference Known Acceleration is established in the following manner:
 - A known acceleration is gravitational acceleration (9.81m/s/s).
 - The sensor is adjusted such that gravitational acceleration is detected by each accelerometer axis individually.
 - Attention is directed toward keeping the responses of the other two axes at zero.
 - Once the gravity vector is along the axis of interest, the Reference Zero Measurement is subtracted to obtain the Sensitivity (V/g)

- The positive and negative sensitivity of each axis is evaluated by orienting the sensor appropriately with respect to direction of gravity.

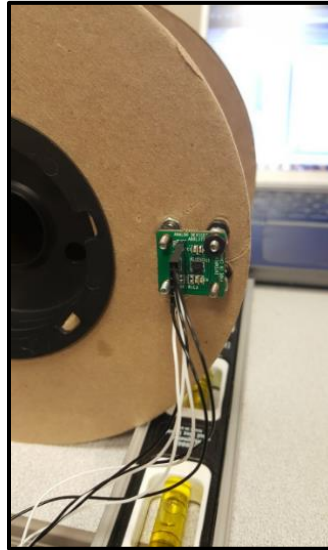


Figure 104a: Accelerometer Measuring 1g along Positive Y-Axis

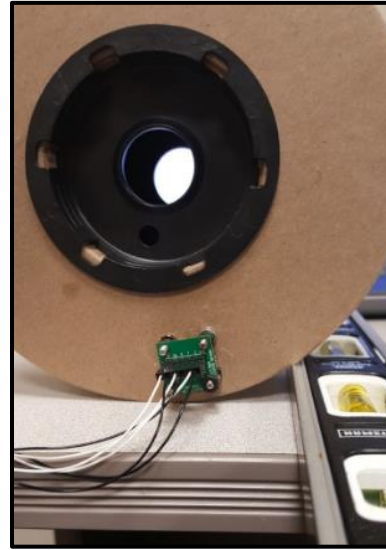


Figure 104b: Accelerometer Measuring 1g along Positive X-Axis



Figure 105: Accelerometer Measuring 1g along Negative Z-Axis.

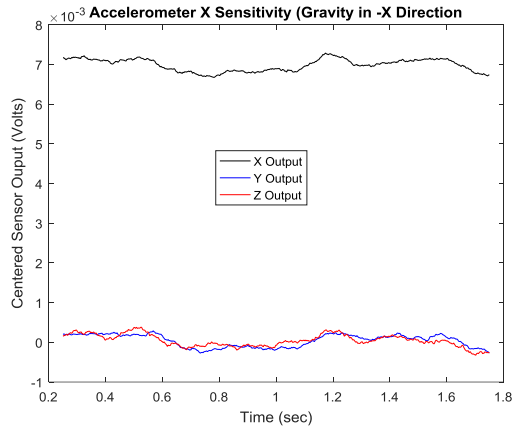


Figure 106: X-axis Reading with Y and Z held at Zero and Gravity in $-X$ Direction.

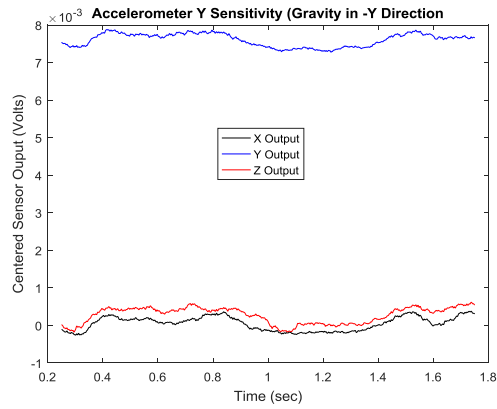


Figure 107: Y-axis Reading with X and Z held at Zero and Gravity in $-Y$ Direction.

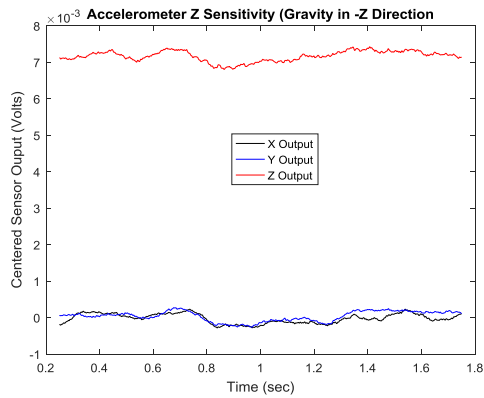


Figure 108: Z-axis Reading with X and Y held at Zero and Gravity in $-Z$ Direction.

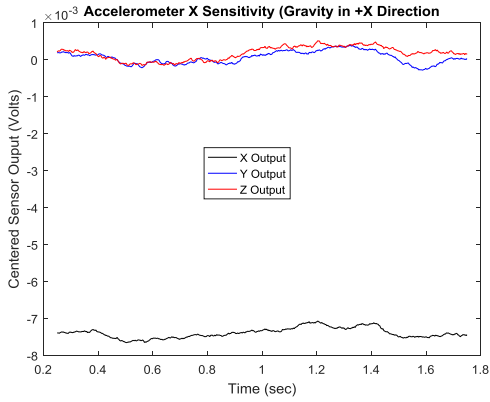


Figure 109: X-axis Reading with Y and Z held at Zero and Gravity in +X Direction.

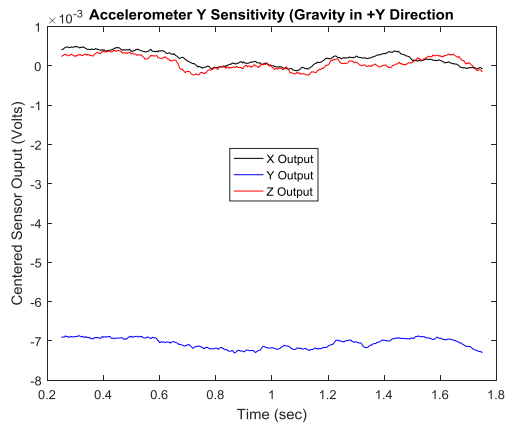


Figure 110: Y-axis Reading with X and Z held at Zero and Gravity in +Y Direction.

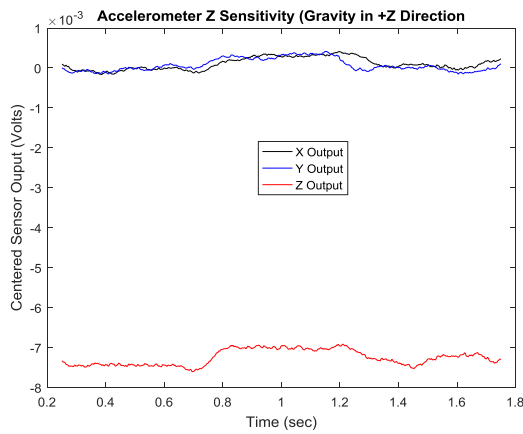


Figure 111: Z-axis Reading with X and Y held at Zero and Gravity in +Z Direction.

- The *negative* sensitivity measurements with gravity along each axis of the sensor arise from nature of the acceleration measurement.
- The accelerometer measures the acceleration of the reference frame in which it is mounted.
- Theory of Relativity states that an object at rest on the surface of the earth is accelerating at 1g upward *with respect to* a freely falling object (upon which no forces are acting).
- For this reason, the accelerometer measures +1g along a certain axis when that axis is pointed upward, or opposite “gravity.”

Appendix E. Model Validation Results

Arm Dynamic Model Validation Collected Data:

- Initial Configuration Test 1: $\vec{\theta}(0) = [-150^\circ; -30^\circ; 0^\circ; 0^\circ]$

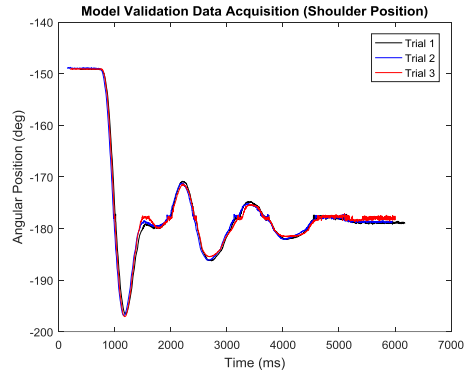


Figure 112: Initial Condition Test 1 Shoulder Trials.

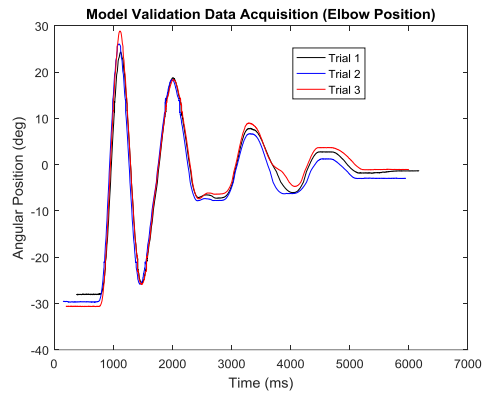


Figure 113: Initial Condition Test 1 Elbow Trials.

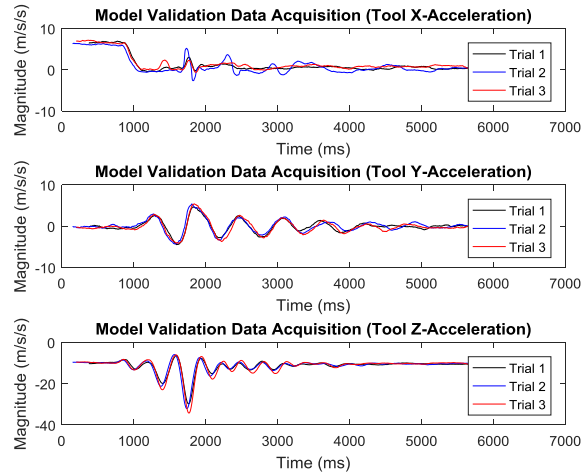


Figure 114: Initial Condition Test 1 Tool Acceleration Trials.

- Initial Configuration Test 2: $\vec{\theta}(0) = [-150^\circ; -30^\circ; 90^\circ; 0^\circ]$

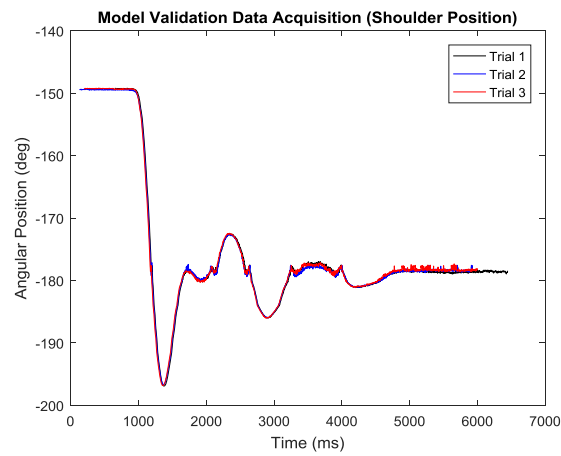


Figure 115: Initial Condition Test 2 Shoulder Trials.

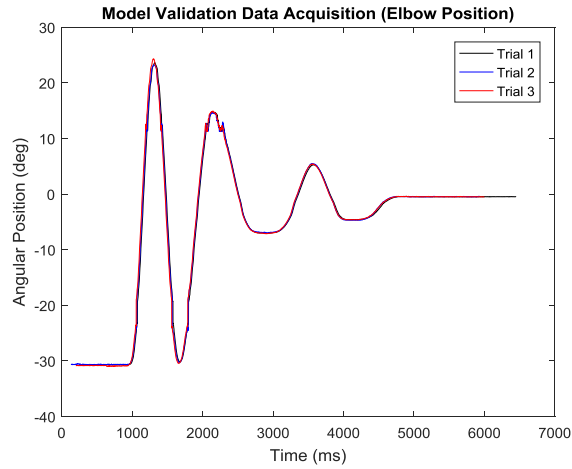


Figure 116: Initial Condition Test 2 Elbow Trials.

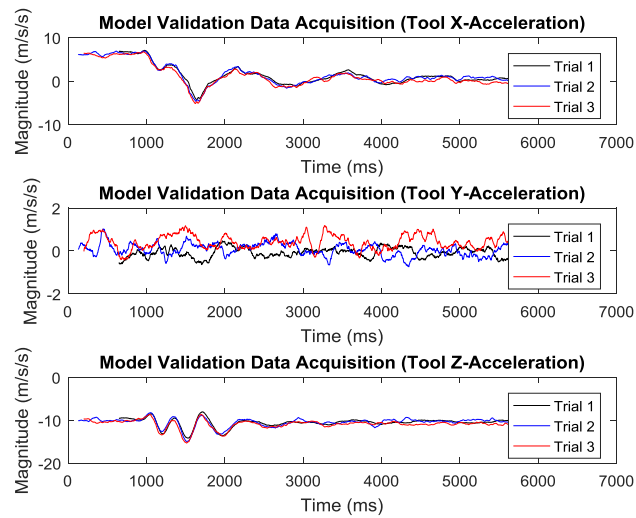


Figure 117: Initial Condition Test 2 Tool Acceleration Trials.

- Initial Configuration Test 3: $\vec{\theta}(0) = [-150^\circ; -30^\circ; -90^\circ; 0^\circ]$

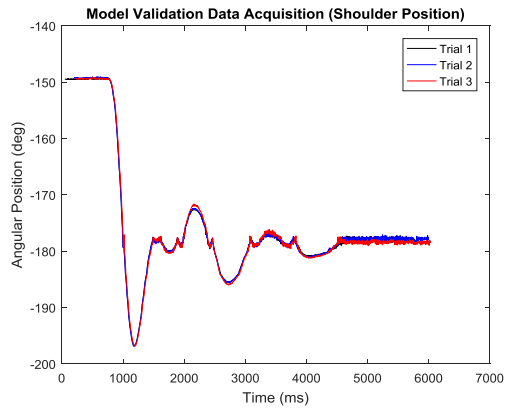


Figure 118: Initial Condition Test 3 Shoulder Trials.

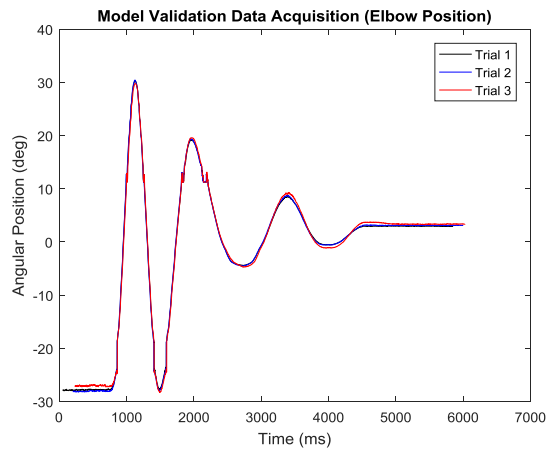


Figure 119: Initial Condition Test 3 Elbow Trials.

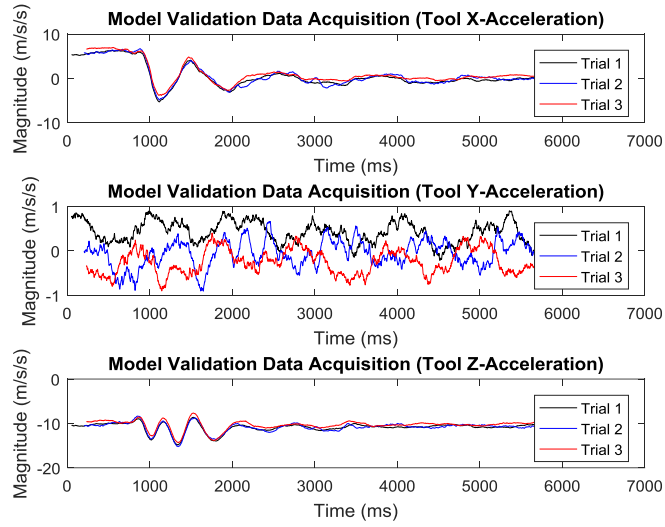


Figure 120: Initial Condition Test 3 Tool Acceleration Trials.

- Initial Configuration Test 4: $\vec{\theta}(0) = [-180^\circ; 0^\circ; -90^\circ; 90^\circ]$

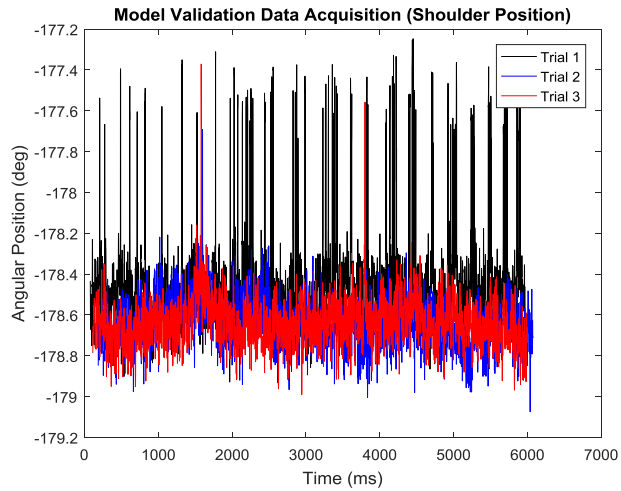


Figure 121: Initial Condition Test 4 Shoulder Trials.

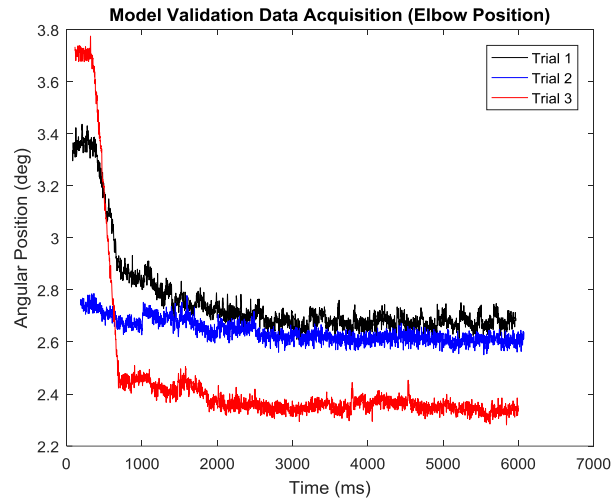


Figure 122: Initial Condition Test 4 Elbow Trials.

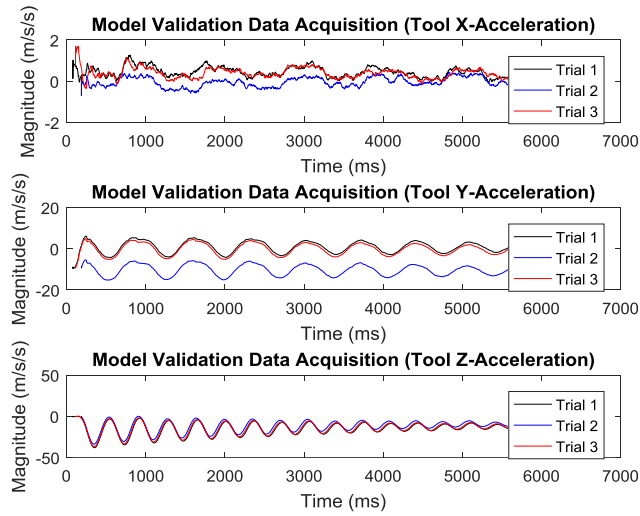


Figure 123: Initial Condition Test 4 Tool Acceleration Trials.

- Initial Configuration Test 5: $\vec{\theta}(0) = [-180^\circ; 0^\circ; 0^\circ; 90^\circ]$

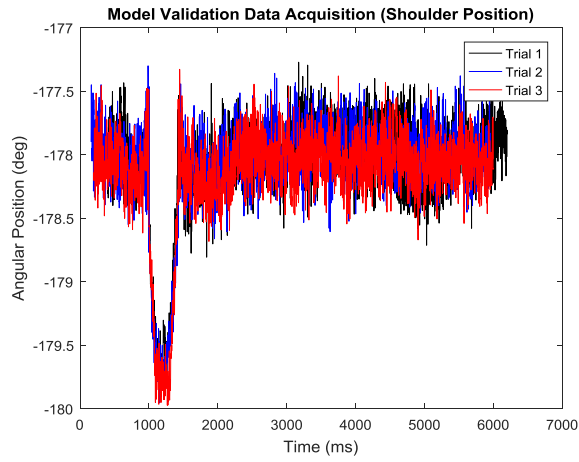


Figure 124: Initial Condition Test 5 Shoulder Trials.

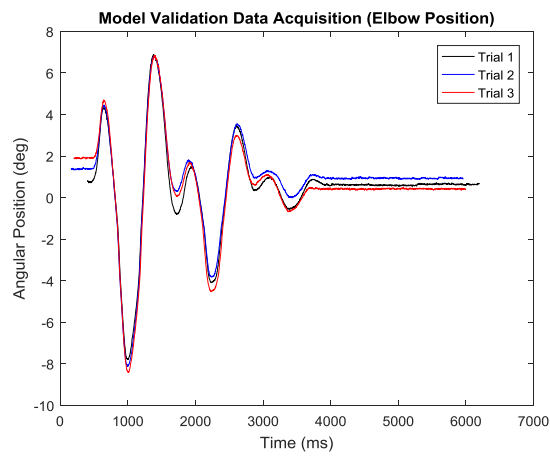


Figure 125: Initial Condition Test 5 Elbow Trials.

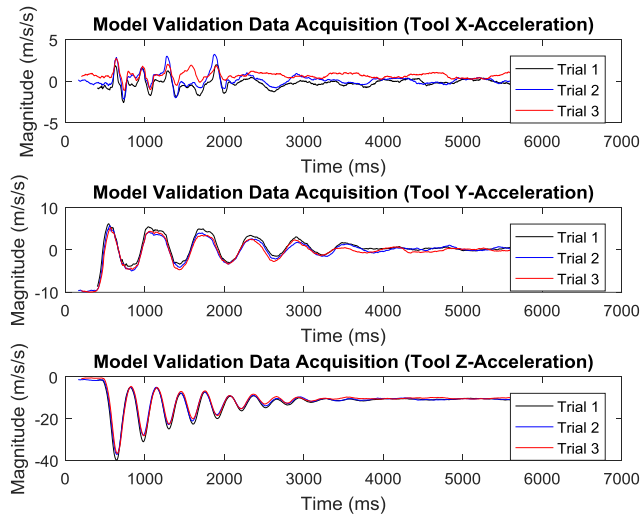


Figure 126: Initial Condition Test 5 Tool Acceleration Trials.

- Initial Configuration Test 6: $\vec{\theta}(0) = [-210^\circ; 30^\circ; 0^\circ; 0^\circ]$

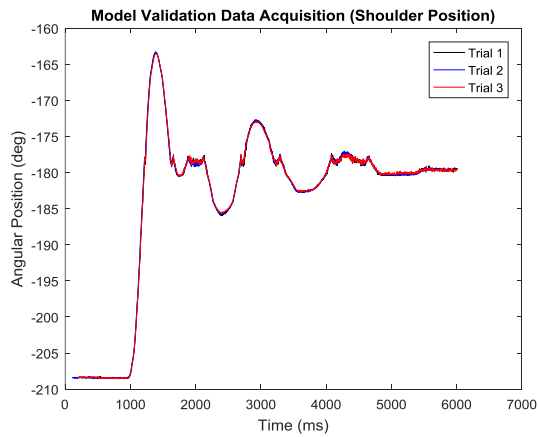


Figure 127: Initial Condition Test 6 Shoulder Trials.

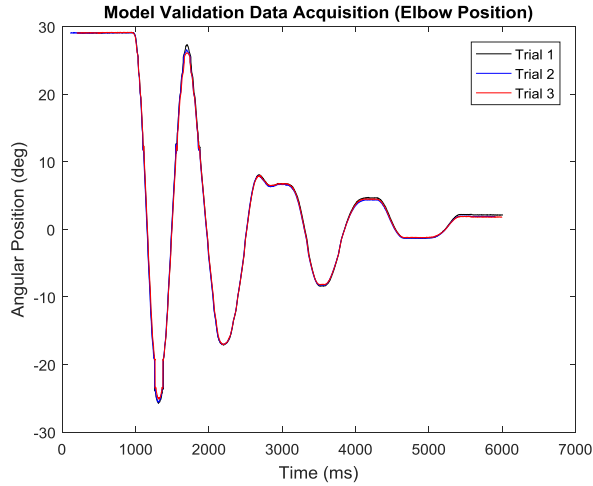


Figure 128: Initial Condition Test 6 Elbow Trials.

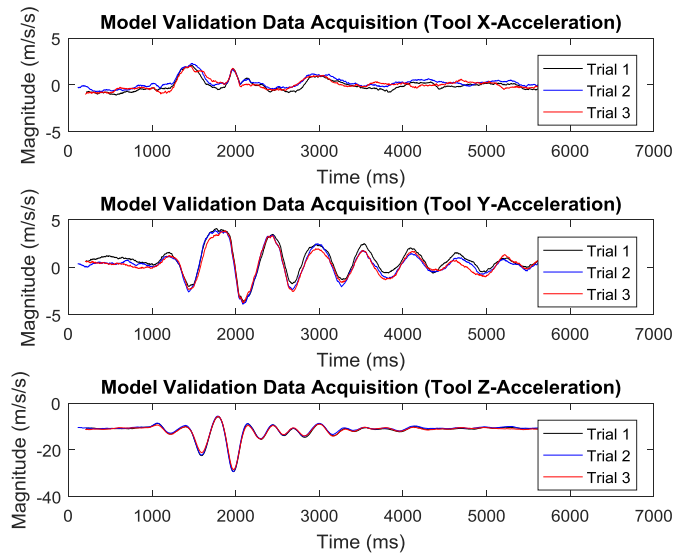


Figure 129: Initial Condition Test 6 Tool Acceleration Trials.

Model Validation Data vs. Simulated Data Response Comparison:

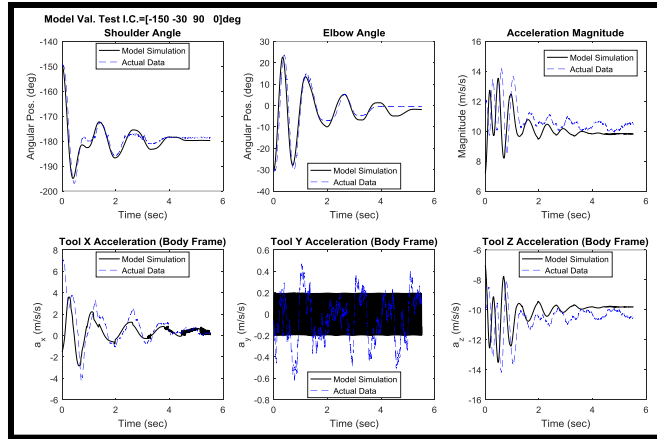


Figure 130: Initial Condition Test 2 Response Comparisons.

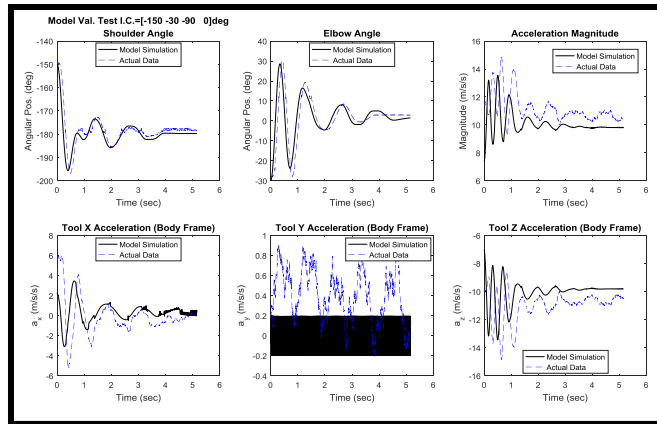


Figure 131: Initial Condition Test 3 Response Comparisons.

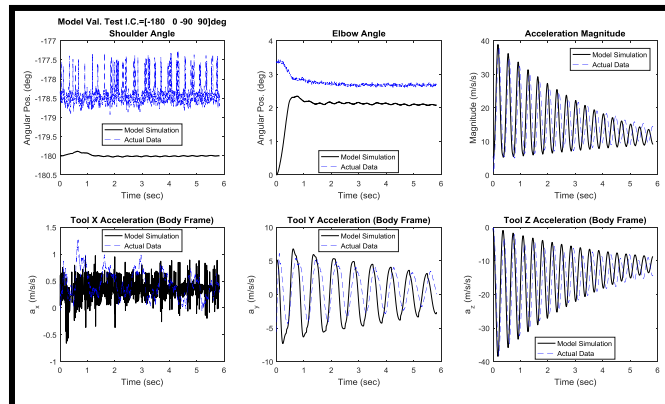


Figure 132: Initial Condition Test 4 Response Comparisons.

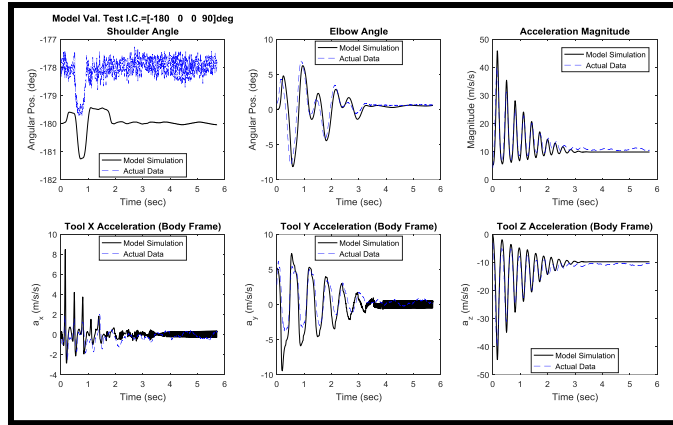


Figure 133: Initial Condition Test 5 Response Comparisons.

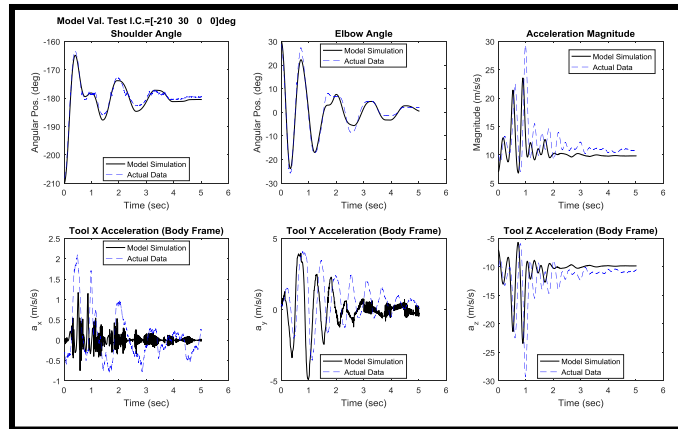


Figure 134: Initial Condition Test 6 Response Comparisons.

- Motor Manufacturer spec sheets

PLG 52 - Ring gear made of steel or no metallic/ Hohlrads Stahl oder Kunststoff																	
Reduction ratio/ Untersetzungsverhältnis		4.5	6.25	8	15	20.25	28.12	36	50	64	91.12	126.5	162	225	288	400	512
Efficiency/ Wirkungsgrad		0.9			0.81						0.73						
Number of stages/ Stufenzahl		1			2						3						
Continuous torque/ Dauerdrehmoment	Nm	1.2			8						24						
Weight of gearbox/ Getriebege wicht	kg	0.56			0.72						0.88						
Axial load/radial load/ Axiallast/Radiallast	N	500/ 350			500/ 350						500/ 350						

Figure 135: Gearbox Manufacturer Specifications.

Data / Technische Daten		GR 42x25		
Rated voltage/ Nennspannung	VDC	12	24	40
Continuous rated speed/ Nenn Drehzahl	rpm*)	3450	3600	3700
Continuous rated torque/ Nenn Drehmoment	Ncm*)	3.9	3.8	3.9
Continuous current/ Nennstrom	A*)	1.9	0.9	0.6
Starting torque/ Anlaufmoment	Ncm**)	19	20	22
Starting current/ Anlaufstrom	A**)	7.8	4	2.76
No load speed/ Leerlauf Drehzahl	rpm**)	4350	4200	4400
No load current/ Leerlaufstrom	A**)	0.34	0.17	0.11
Demagnetization current/ Entmagnetisierstrom	A**)	14	6.5	4.1
Rotor inertia/ Trägheitsmoment	gcm ²	71	71	71
Weight of motor/ Motorgewicht	g	390	390	390

*) $\Delta\theta_w = 100\text{ K}$; **) $\theta_R = 20^\circ\text{C}$

Figure 136: Elbow Motor Manufacturer Specifications.

Data / Technische Daten		GR 53x30			
Rated voltage/ Nennspannung	VDC	12	24	40	60
Continuous rated speed/ Nenn Drehzahl	rpm*)	3790	3600	3680	4000
Continuous rated torque/ Nenn Drehmoment	Ncm*)	9	10	10	10
Continuous current/ Nennstrom	A*)	4.5	2.3	1.3	0.9
Starting torque/ Anlaufmoment	Ncm**)	57	67	66	69
Starting current/ Anlaufstrom	A**)	23.7	13.5	7.7	5.6
No load speed/ Leerlauf Drehzahl	rpm**)	4490	4200	4280	4500
No load current/ Leerlaufstrom	A**)	0.58	0.28	0.17	0.12
Demagnetization current/ Entmagnetisierstrom	A**)	42	20	12	8.5
Rotor inertia/ Trägheitsmoment	gcm ²	230	230	230	230
Weight of motor/ Motorgewicht	g	850	850	850	850

*) $\Delta\theta_w = 100\text{ K}$; **) $\theta_R = 20^\circ\text{C}$

Figure 137: Shoulder Motor Manufacturer Specifications.

Appendix F. Accuracy and Control Performance Plots and Uncertainty Calculation

Computed Torque and Voltage Regulation Control Plots:

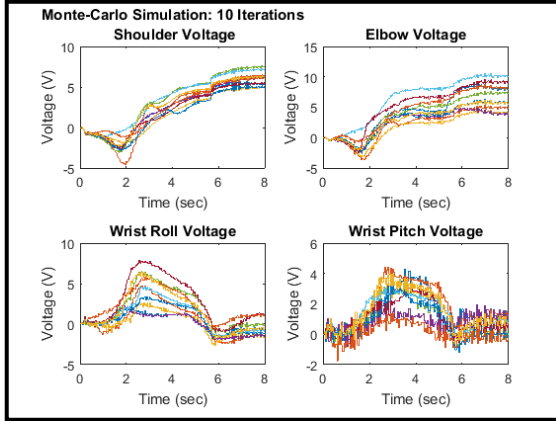


Figure 138a: Motor Voltage for $\vec{\theta}_0 = [0^\circ, 0^\circ, 0^\circ, 0^\circ]$, $\vec{\theta}_f = [-70^\circ, -50^\circ, 70^\circ, 30^\circ]$.

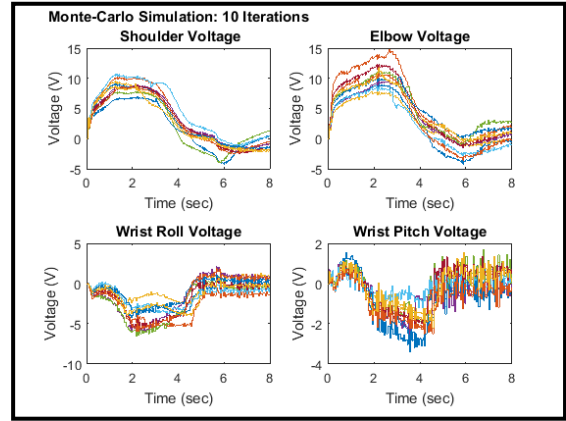


Figure 138b: Motor Voltage for $\vec{\theta}_0 = [-70^\circ, -50^\circ, 70^\circ, 30^\circ]$, $\vec{\theta}_f = [0^\circ, 0^\circ, 0^\circ, 0^\circ]$.

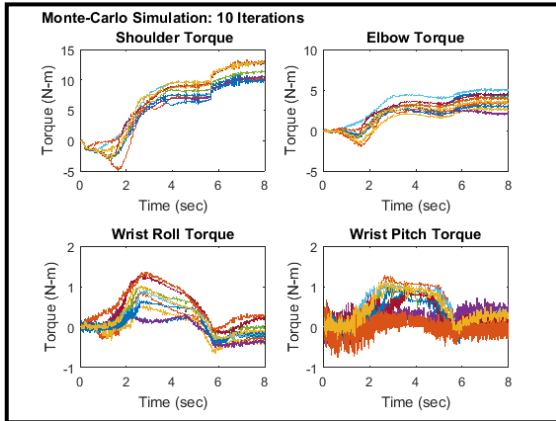


Figure 139a: Motor Torque for $\vec{\theta}_0 = [0^\circ, 0^\circ, 0^\circ, 0^\circ]$, $\vec{\theta}_f = [-70^\circ, -50^\circ, 70^\circ, 30^\circ]$.

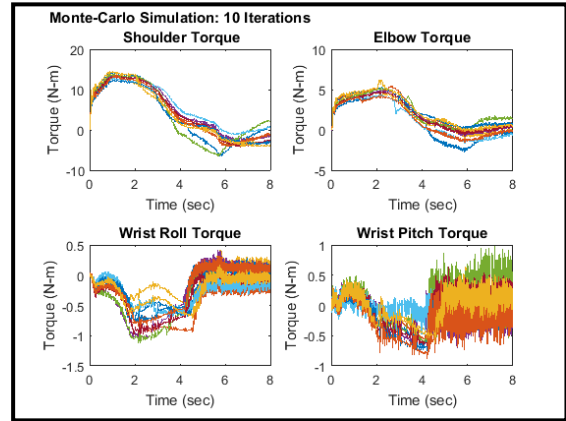


Figure 139b: Motor Torque for $\vec{\theta}_0 = [-70^\circ, -50^\circ, 70^\circ, 30^\circ]$, $\vec{\theta}_f = [0^\circ, 0^\circ, 0^\circ, 0^\circ]$.

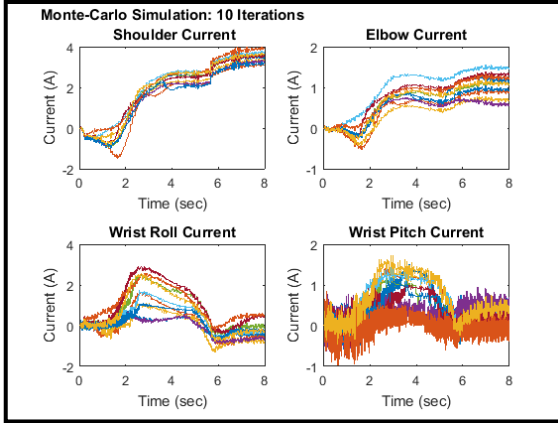


Figure 140a: Motor Current for $\vec{\theta}_0 = [0^\circ, 0^\circ, 0^\circ, 0^\circ]$, $\vec{\theta}_f = [-70^\circ, -50^\circ, 70^\circ, 30^\circ]$.

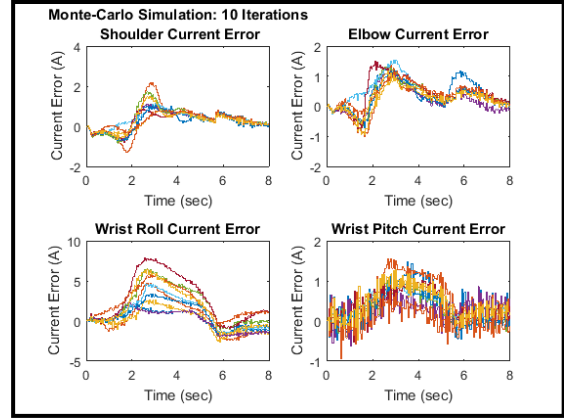


Figure 140b: Current Error for $\vec{\theta}_0 = [0^\circ, 0^\circ, 0^\circ, 0^\circ]$, $\vec{\theta}_f = [-70^\circ, -50^\circ, 70^\circ, 30^\circ]$.

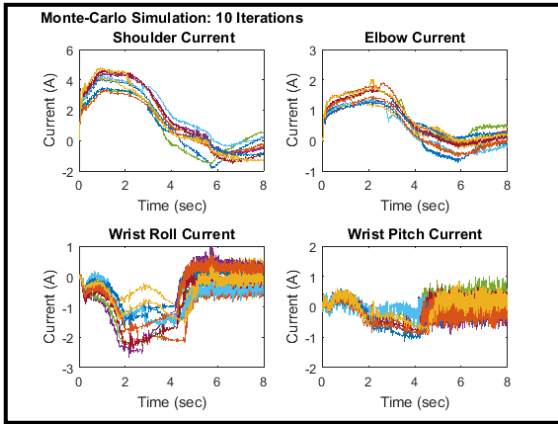


Figure 140c: Motor Current for $\vec{\theta}_0 = [-70^\circ, -50^\circ, 70^\circ, 30^\circ]$, $\vec{\theta}_f = [0^\circ, 0^\circ, 0^\circ, 0^\circ]$.

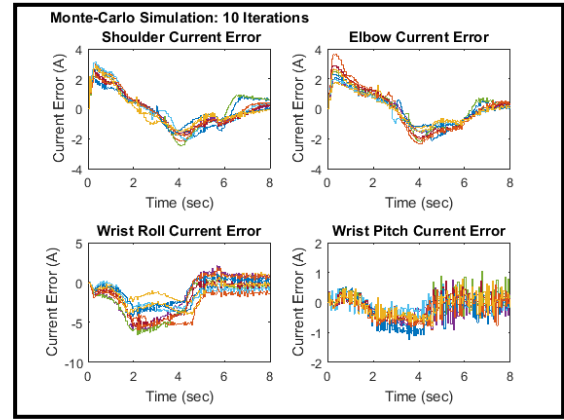


Figure 140d: Current Error for $\vec{\theta}_0 = [-70^\circ, -50^\circ, 70^\circ, 30^\circ]$, $\vec{\theta}_f = [0^\circ, 0^\circ, 0^\circ, 0^\circ]$.

Monte Carlo Analysis Uncertainty Parameterization:

- Kinematic Uncertainty:
 - Represents uncertainty in:
 - Physical size and shape of the manipulator caused by precision limitations on equipment used to machine and manufacture components.
 - Assembly process, namely in areas where the design is adjustable and must be configured by “eye,” such as the connections that fasten bicep to shoulder, forearm to elbow, and shoulder to base.
 - Position measurement caused by errors in sensor calibration and resolution of sensing equipment.
 - Quantified as:
 - ± 0.001 ” on all dimensions of components machined in the Lafferre Hall ETS Machine Shop due to machine precision.
 - $\pm 1/16$ ” on dimensions related to manual location of parts during assembly.
 - Manufacturing tolerance specifications for all prefabricated and purchased parts.
 - $\pm 1^\circ$ On position sensing measurements.
- Dynamic Uncertainty:
 - Represents Uncertainty in:
 - Link lengths, masses, moments of inertia, center of mass location, friction coefficients.

- Motor dynamic parameters including: resistance, inductance, voltage and torque constants, gearbox efficiency, and gearbox reduction ratio.
 - Environmental disturbance torques caused by: collisions or extra loads placed on the arm.
 - Extra loading caused by picking up an object of unknown weight and location with respect to the gripper.
- Quantified as:
 - $\pm 5\%$ of Nominal value for arm dynamic properties.
 - $\pm 20\%$ Nominal value for motor dynamic properties to account for errors in motor model validation and potential effects of radiation exposure on motor functionality.
 - Random disturbances of ± 2 Nm at the shoulder joint, ± 1 Nm at the Elbow Joint, ± 0.25 Nm at the Wrist Roll Joint, and ± 0.25 Nm at the Wrist Pitch Joint.
 - Extra loading caused by grasping and picking up an object is modelled as a random increase in the mass and inertial properties of the end effector link.
 - The current end effector has a gripping length of approximately 2 inches, this means that an object can theoretically be grasped if its center of mass is around ± 1 " from the center of the gripping surface.

- The position of the center of the gripping surface is defined with respect to the wrist pitch joint by the length L_3 .
- The distance between the center of mass of the end effector and the center of the gripper is $d_{cg} = L_3 - c_7$.
- In order to provide a factor of safety against objects slipping out of the end of the gripper if they are too far, or hitting the actuator if they are too close, objects are allowed to be grasped at random distances between $0.8d_{cg}$ and $1.3d_{cg}$. This is equivalent to around 0.56” ‘closer’ to the wrist pitch joint than the center of the gripper, and 0.8415” ‘farther’ from the joint than the center of the gripper.
- The object is allowed to have a random mass between 0 and 0.25kg.
- Mathematically speaking:

$$d_{obj} = rand[0.8d_{cg}, 1.3d_{cg}]$$

$$m_{obj} = rand[0,0.25]kg$$

Adding new mass to the end effector moves the location the center of mass of the new rigid body system by c_x :

$$m_4 c_x = m_{obj}(d_{obj} - c_x) \rightarrow c_x = \frac{m_{obj}d_{obj}}{m_4 + m_{obj}}$$

and also adds a new component to the moments of inertia about the X and Y axes as such:

$$I_{xx,obj} = m_{obj}(d_{obj} - c_x)^2 = I_{yy,obj}$$

- The added moment of inertia about the Z axis is neglected because it is assumed that the center of mass of the object lies very close to this axis.
- The random mass of the object is added to the mass of the end effector, the moments of inertia of the object about the new center of mass are added to their end effector counterparts, and the dimension c_x is added to c_7 to describe the new end effector C.O.M. location.

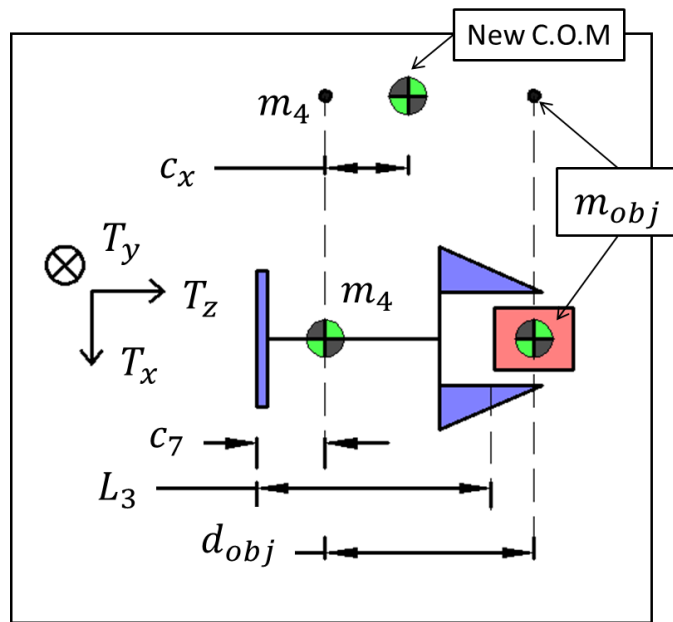


Figure 141: Grasped Object Mass and Location Uncertainty.

Tables parameterizing uncertainty in the kinematic dimensions can be seen on the following pages.

Kinematic Parameter: Y0					
Source of Uncertainty	Area	Type of Uncertainty	Value of Uncertainty (+ -) in inches	Uncertainty Multiplier	Total Uncertainty
Fastening Hole Pattern of 1 1/2" T-Slot Lower Brackets to Base Plate	Base Assembly	Machining	0.001	1	0.001
Lengthwise Fastening of Base Adapter Plate to 1 1/2" T-Slot	Base Assembly	Human	0.0625	1	0.0625
Fastening Hole Pattern of Base Adapter Plate to Shoulder Joint Block	Base Assembly	Machining	0.001	2	0.002
Shoulder Axel Cylinder Horizontal Location and Alignment	Shoulder Assembly	Machining	0.002	1	0.002
Fastening Hole Pattern for Joint Axel onto Shoulder/Bicep Adapter Plate	Bicep Assembly	Machining	0.001	2	0.002
Fastening of Bicep/Shoulder Adapter Plate to Bicep 20mm T-Slot	Bicep Assembly	Human	0.01	1	0.01
Crosswise Fastening of Short Bicep 20mm T-Slot to Long T-Slot and Bicep/Elbow Adapter Plate	Bicep Assembly	Human	0.01	1	0.01
Fastening Hole Pattern for Bicep/Elbow Adapter onto Elbow Joint Block	Elbow Assembly	Machining	0.001	2	0.002
Elbow Axel Cylinder Horizontal Location and Alignment	Elbow Assembly	Machining	0.002	1	0.002
Fastening Hole Pattern for Elbow Axel onto Elbow/Forearm Adapter Plate	Forearm Assembly	Machining	0.001	2	0.002
Fastening of Elbow/Forearm Adapter Plate onto Forearm 20mm T-Slot	Forearm Assembly	Human	0.01	1	0.01
Lengthwise Fastening of Short Forearm 20mm T-Slot to Long T-Slot and Wrist/Forearm Adapter Plate	Forearm Assembly	Human	0.0625	1	0.0625
Fastening Hole Pattern for Wrist/Forearm Adapter Plate onto WR Cyl.	Forearm Assembly	Machining	0.001	2	0.002
Y-Axis Location and Alignment of WR Cylinder and WR Axel	Forearm Assembly	Machining	0.002	1	0.002
Fastening Hole Pattern of WR Axel onto Wrist Pitch Block Base	Forearm Assembly	Machining	0.001	2	0.002
Fastening Hole Pattern of WP Block Axel Mount onto WP Block Base	Wrist Pitch Assembly	Machining	0.001	2	0.002
Horizontal Location of WP Axel Mounting Hole and Alignment of WP Axel	Wrist Pitch Assembly	Machining	0.002	1	0.002
Fastening Hole Pattern for WP Axel onto End-Eff. Mount onto EE Base	Wrist Pitch Assembly	Machining	0.001	3	0.003
Fastening Hole Pattern for EE Mount onto EE Base and Y-Axis Alignment of Solenoid Mounting Hole	End-Effector Assembly	Machining	0.01	1	0.01
Total Uncertainty:					0.191

Table 16: Uncertainty in Kinematic Parameter $y_{0 \rightarrow 1}$.

Kinematic Parameter: Z0					
Source of Uncertainty	Area	Type of Uncertainty	Value of Uncertainty (+ -) in inches	Uncertainty Multiplier	Total Uncertainty
Width of Base Plate	Base Assembly	Machining	0.005	1	0.005
Length of 1 1/2" T-Slot Base	Base Assembly	Machining	0.005	1	0.005
Width of Base/Shoulder Adapter Plate	Base Assembly	Machining	0.005	1	0.005
Vertical Location and Alignment of Shoulder Axel Cylinder Axel	Shoulder Assembly	Machining	0.002	1	0.002
Total Uncertainty					0.017

Table 17: Uncertainty in Kinematic Parameter $z_{0 \rightarrow 1}$.

Kinematic Parameter: L1					
Source of Uncertainty	Area	Type of Uncertainty	Value of Uncertainty (+ -) in inches	Uncertainty Multiplier	Total Uncertainty
Length of Bicep T-Slot	Bicep Assembly	Machining	0.005	1	0.005
Accuracy of Etched Length Scale	Bicep Assembly	Machining	0.005	1	0.005
Accuracy of Manual Length Adjustment	Bicep Assembly	Human	0.03125	1	0.03125
Short Width of Bicep Double 20mm T-Slot	Bicep Assembly	Manufacturing	0.01	1	0.01
Width of Bicep/Elbow Adapter Plate	Bicep Assembly	Machining	0.005	1	0.005
Vertical Location and Alignment of Elbow Axel Cylinder and Axel	Elbow Assembly	Machining	0.002	1	0.002
Total Uncertainty:					0.05825

Table 18: Uncertainty in Kinematic Parameter L_1 .

Kinematic Parameter: L2					
Source of Uncertainty	Area	Type of Uncertainty	Value of Uncertainty (+ -) in inches	Uncertainty Multiplier	Total Uncertainty
Length of Forearm T-Slot	Forearm Assembly	Machining	0.005	1	0.005
Accuracy of Etched Length Scale	Forearm Assembly	Machining	0.005	1	0.005
Accuracy of Manual Length Adjustment	Forearm Assembly	Human	0.03125	1	0.03125
Width of Forearm 20mm T-Slot	Forearm Assembly	Manufacturing	0.01	1	0.01
Width of Forearm/Wrist Adapter Plate and Wrist Roll Cylinder Bearing Seat	Forearm Assembly	Machining	0.005	1	0.005
Width of Wrist Roll Thrust Bearings	Forearm Assembly	Manufacturing	0.0021	1	0.0021
Length of WR Axle Bearing Surface	Forearm Assembly	Machining	0.005	1	0.005
Length of Wrist Roll Axle	Forearm Assembly	Machining	0.005	1	0.005
Vertical Location of Fastening Holes for Wrist Pitch Axle Mount to Wrist Pitch Block Base	Wrist Pitch Assembly	Machining	0.001	2	0.002
Vertical Location and Alignment of Wrist Pitch Axle and Cylinder	Wrist Pitch Assembly	Machining	0.002	1	0.002
Total Uncertainty:					0.07235

Table 19: Uncertainty in Kinematic Parameter L₂.

Kinematic Parameter: L3					
Source of Uncertainty	Area	Type of Uncertainty	Value of Uncertainty (+ -) in inches	Uncertainty Multiplier	Total Uncertainty
Flat Width of Wrist Pitch Axle	Wrist Pitch Assembly	Machining	0.005	1	0.005
Length of End-Effector Mounting Shaft	Wrist Pitch Assembly	Machining	0.005	1	0.005
Length of End-Effector	End Effector Assembly	Manufacturing	0.0625	1	0.0625
Total Uncertainty:					0.0725

Table 20: Uncertainty in Kinematic Parameter L₃.

Monte Carlo Accuracy and Robustness Simulation Motor Analysis Plots:

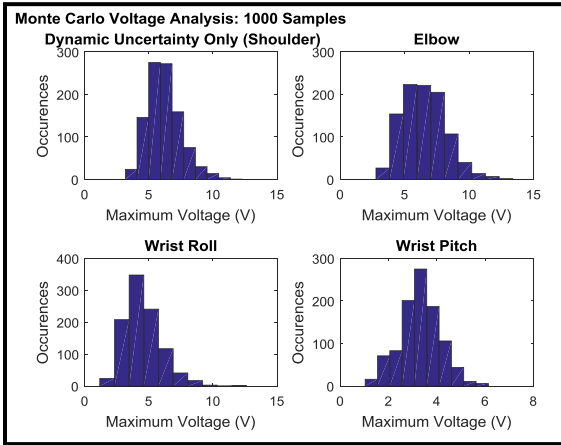


Figure 142a: Max Motor Voltage for
 $\vec{\theta}_0 = [0^\circ, 0^\circ, 0^\circ, 0^\circ]$,
 $\vec{\theta}_f = [-70^\circ, -50^\circ, 70^\circ, 30^\circ]$, 1000
 Iterations, Dynamic Uncertainty Only.

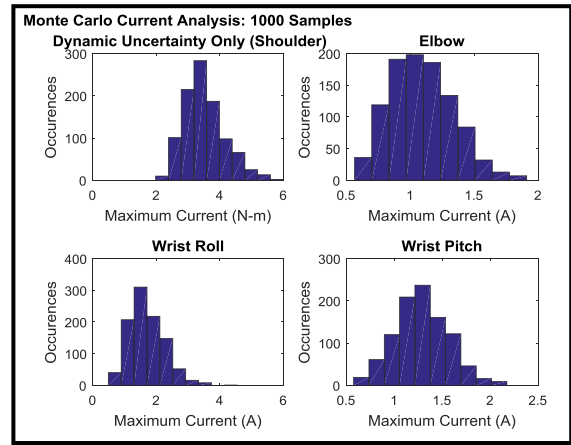


Figure 142b: Max Motor Current for
 $\vec{\theta}_0 = [0^\circ, 0^\circ, 0^\circ, 0^\circ]$,
 $\vec{\theta}_f = [-70^\circ, -50^\circ, 70^\circ, 30^\circ]$, 1000
 Iterations, Dynamic Uncertainty Only.

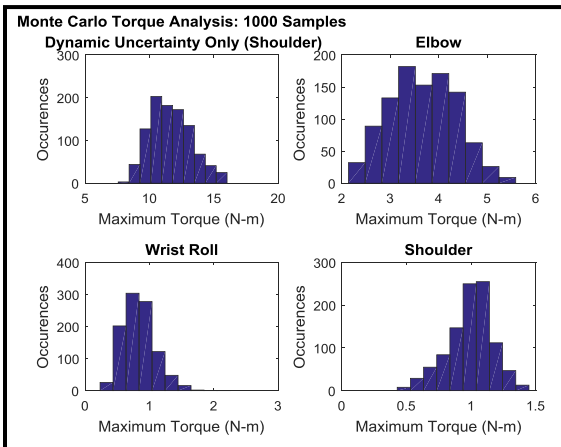


Figure 142c: Max Motor Torque for
 $\vec{\theta}_0 = [0^\circ, 0^\circ, 0^\circ, 0^\circ]$,
 $\vec{\theta}_f = [-70^\circ, -50^\circ, 70^\circ, 30^\circ]$, 1000
 Iterations, Dynamic Uncertainty Only.

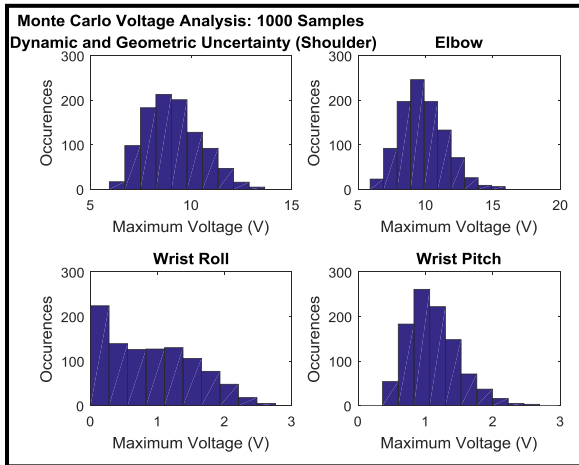


Figure 143a: Max Motor Voltage for $\vec{\theta}_0 = [-70^\circ, -50^\circ, 70^\circ, 30^\circ]$, $\vec{\theta}_f = [0^\circ, 0^\circ, 0^\circ, 0^\circ]$, 1000 Iterations, Dynamic and Kinematic Uncertainty.

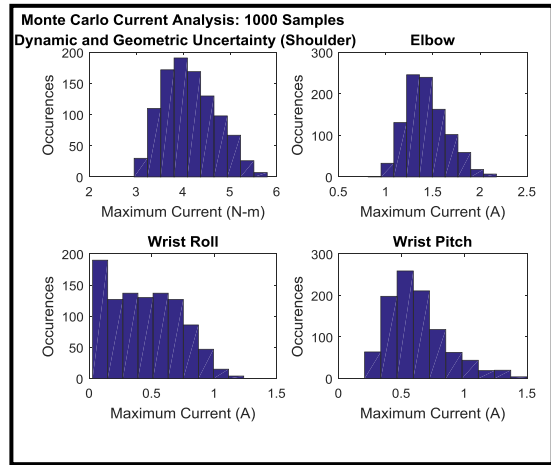


Figure 143b: Max Motor Current for $\vec{\theta}_0 = [-70^\circ, -50^\circ, 70^\circ, 30^\circ]$, $\vec{\theta}_f = [0^\circ, 0^\circ, 0^\circ, 0^\circ]$, 1000 Iterations, Dynamic and Kinematic Uncertainty.

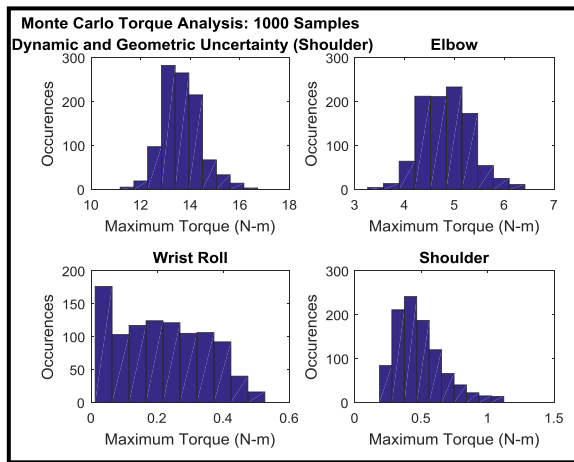


Figure 143c: Max Motor Torque for $\vec{\theta}_0 = [-70^\circ, -50^\circ, 70^\circ, 30^\circ]$, $\vec{\theta}_f = [0^\circ, 0^\circ, 0^\circ, 0^\circ]$, 1000 Iterations, Dynamic and Kinematic Uncertainty.

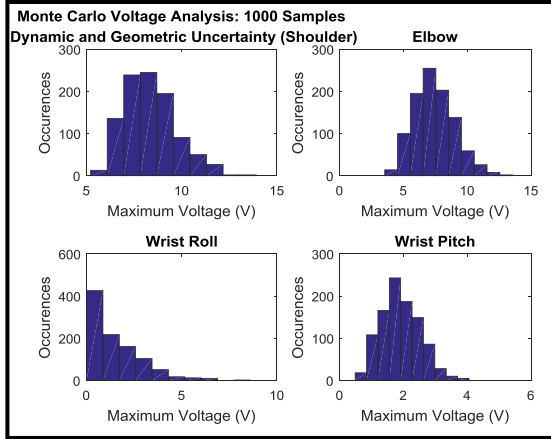


Figure 144a: Max Motor Voltage for
 $\vec{\theta}_0 = [-70^\circ, -50^\circ, 70^\circ, 30^\circ]$,
 $\vec{\theta}_f = [30^\circ, -135^\circ, 0^\circ, 15^\circ]$, 1000
 Iterations, Dynamic and Kinematic
 Uncertainty.

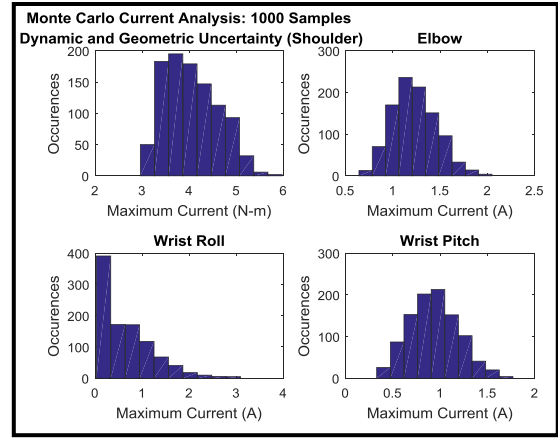


Figure 144b: Max Motor Voltage for
 $\vec{\theta}_0 = [-70^\circ, -50^\circ, 70^\circ, 30^\circ]$,
 $\vec{\theta}_f = [30^\circ, -135^\circ, 0^\circ, 15^\circ]$, 1000
 Iterations, Dynamic and Kinematic
 Uncertainty.

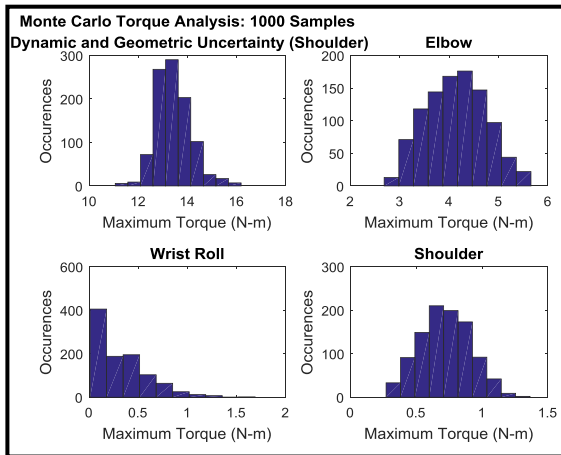


Figure 144c: Max Motor Voltage for
 $\vec{\theta}_0 = [-70^\circ, -50^\circ, 70^\circ, 30^\circ]$,
 $\vec{\theta}_f = [30^\circ, -135^\circ, 0^\circ, 15^\circ]$, 1000
 Iterations, Dynamic and Kinematic
 Uncertainty.